Friction Modelling

– and Parameter Estimation for Hydraulic Asymmetrical Cylinders

Master's Thesis

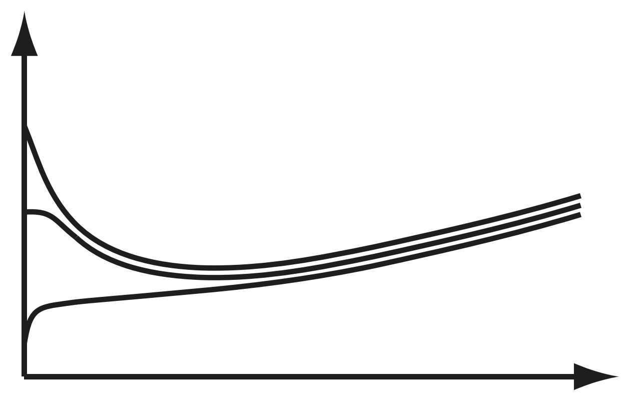

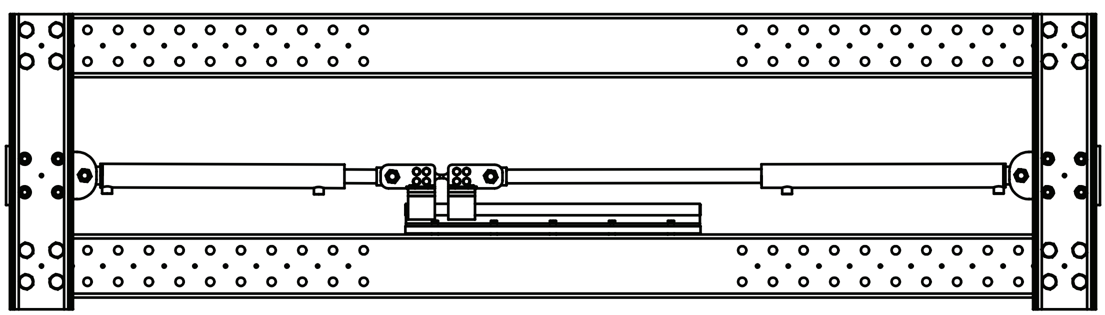

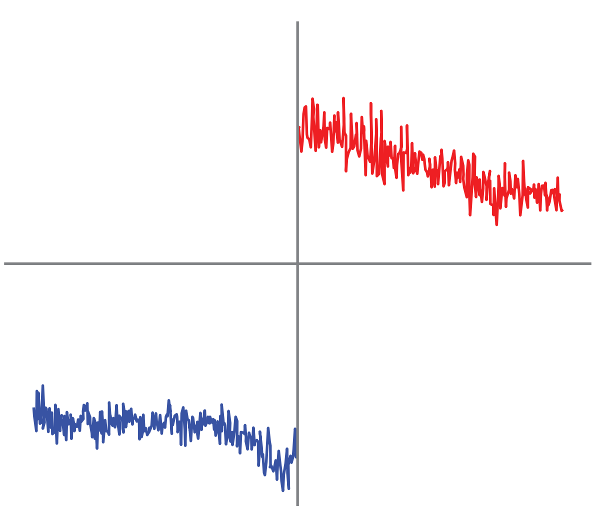

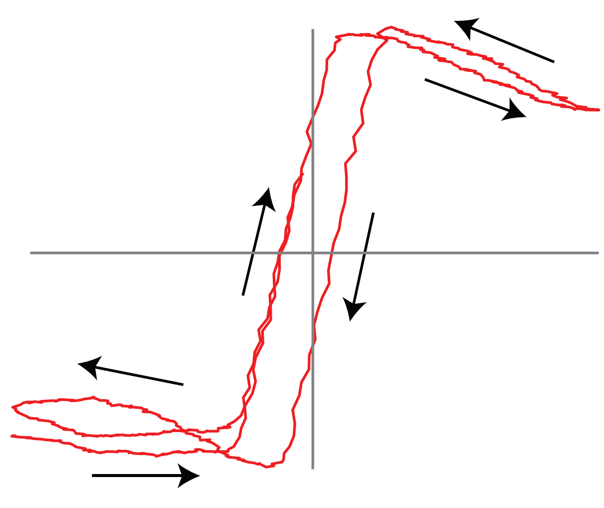

Aalborg University

Electro-Mechanical Systems Design

Fibigerstræde 16

DK-9220 Aalborg Øst

Tel: +45 99 40 93 09

Fax: +45 98 15 16 75

E-mail: swe@ime.aau.dk

http://www.industri.aau.dk

FRICTION MODELLING AND PARAMETER ESTIMATION FOR HYDRAULIC ASYMMETRICAL CYLINDERS

Theme: Master's Thesis

Type:	Semester Report
Semester:	10^{th} EMSD
ECTS:	30
Project period:	1/2/2011-15/5/2011
Project group:	54G
Supervisors:	Torben O. Andersen
	Lasse Schmidt
Prints in circulation:	6
Pages excl. Appendix:	74
Pages incl. Appendix:	100
Enclosed:	1 *DVD*

Mads Hvoldal

Casper Olesen

Synopsis:

This report is developed as a part of master's thesis in Electro-Mechanical System Design (EMSD) at Aalborg University, Denmark.
A full system model was developed based on a test bench including three servo valves and two asymmetrical cylinders. This model was incorporated in the simulation program, Simulink. The cylinder denoted *test cylinder* was to maintain a velocity reference whereas a force control was developed for the second cylinder. The expressions where linearised in order to develop controllers suitable for the chosen control strategies. Satisfactory controllers where developed and the performance of these where documented. Investigations, in the field of friction, where made, and commented on in the report. Through experimental data the phenomena where illustrated, and the demands for a friction model stated. Friction parameters and efficiencies where found derived for different operational situations of the cylinder. A program was written to semi-automatic determine the friction parameters and the efficiency of a given cylinder.

By signing this document, each member of the project group certifies that all have contributed equally in the writing of this project and are jointly being liable for the contents of this report.

Preface

This is a report by Mads Hvoldal and Casper Olesen, project group 54G. The project period concludes the 10 th semester *EMSD* from february 1th 2011 to June 11st 2011. The project theme is *Friction Modelling And Compensation On A Hydraulic Asymmetrical Cylinder*.
According to the study guide [Studienævnet for Industri og Global Forretningsudvikling, 2010] the aim of the project is to acquire competence in the following areas:

- Account for the solved problem and set up criteria for the solution.
- Be able to evaluate terms, theories and methods used to solve the problem.
- Be able to document that central concepts, theories and methods used are used correctly in the problem solution.
- Account for the choices made and that they are made on a professional level.
- Be able to evaluate limitations in applied theories, methods and approach to solving the problem.
- Be able to evaluate the solution against the set up criteria.

Guide

This report uses the Harvard system of referencing. In context this appears as the authors surname and year of publishing in square brackets, e.g. [Phillips, 2000]. If the year of publishing is uncertain or unknown this will be followed by an asterisk, e.g. [Phillips, 2000*]. The references cited are found in detail in the *Bibliography* sorted alphabetically by authors surname.

Appendices are generally referred to as e.g. *appendix A.2*. A *PDF* version of the report and enclosures are found on the enclosed DVD.

Appendix A Parameter Values, beginning on page 77, contains tabulated parameter values applied or obtained throughout the report. This list also serves as a general nomenclature.

Contents

Abstract

This report is a master's thesis in Electro-Mechanical System Design (EMSD) at Aalborg University, Denmark.

Daniel Henriksen designed, in the year 2010, a test bench for hydraulic cylinders. This test bench constitutes the base for this project, with a minor modification to his design, as two servo valves, instead of one, controlling the load produced by at cylinder. The test bench had at the beginning of the project, not yet been operational and different electrical circuit boards where needed to be designed, documented and manufactured.

A full system model was developed based on fluid-mechanical expressions. This model was incorporated in the simulation program, Simulink. The expressions where linearised in order to develop controllers suitable for the chosen control strategies. Satisfactory controllers where developed and the performance of these where documented. To enable implementation of the chosen control strategies in the physical setup, a control program was developed in Code Composer Studio v4. Semi-automatic execution of experiments where achieved and a procedure on how to use the system, for friction determination, was formulated.

Investigations, in the field of friction, have been made by studying the documented work made by recognized scientists dating back to the sixties. The most well documented friction phenomena are presented throughout this report, including the Stribeck effect, friction lag and hysteresis loops. Steady state and dynamic friction models are introduced and the assumptions and simplifications made within these are stated. The friction models presented are the Márton and Lantos model (in which the Tustin model is used), the pressure-based model, the LuGre model and a modified Leuven model.

Experiments where conducted, on the test bench, in order to test the properties of the friction models, which are incorporated in a developed simulation model of the full system. In order to compare the friction models, values for respective friction parameters where derived from the data. Regrettably, no successful implementation was achieved, but the characteristic friction phenomena was documented and the efficiency of the test cylinder was derived.

1 Introduction

This chapter introduces the foundation for the report by presenting an initial problem, which is desired to be solved through use of the experimental setup available and studies in the areas of friction. To be able to solve the initial problem, a series of subproblems are specified in a problem specification.

In modern industry, optimization is an important topic. If an optimization of machinery is to be performed, it is important not only to understand the phenomena occurring in it, but also to be able to model each aspects contributioning to the full system behavior. Or at least know which aspects to ignore. In dynamical modelling an important phenomenon is friction.

Friction has been investigated thoroughly throughout the years and several friction models have been proposed and tried verified through tests. The earliest recorded attempt to describe friction was done by Leornado da Vinci in 1519 and later by Charles Augustin de Coulomb in 1785 [Armstrong-Hélouvry et al., 1994]. More resent studies where made by Brian Armstrong-Hélouvry and P. R. Dahl to name a few of the most recognized scientists in this field. The friction models developed by the last mentioned scientists are considerable more comprehensive as they include the transition from the static to the dynamic regime.

The nature of friction is to oppose movement. Friction has both positive and negative aspects. It is used as a positive feature when braking, clamping and often also when considering control systems. The natural damping is used to stabilize a system and friction is often a part of this induced phenomenon. A negative aspect is of course the energy loss associated with overcoming the friction when actuation is wanted. The force diminished by friction, when using hydraulic actuators, is typically between 10 and 15%, but up to 30 % [Bonchis et al., 1999]. Minimizing this loss is essentially the motivation for many of todays engineering companies to carry out research in friction.When knowing the friction characteristics, an implementation of friction compensation in the control strategy should be able to achieve a greater performance.

In 2010 Daniel Henriksen designed a test stand for hydraulic cylinders as a part of his master's thesis in EMSD [Henriksen, 2010]. This test bench is used in the present experimental study of friction.

1.1 Initial Problem

With the friction test bench at hand, it is desired at the end of this project to be able to estimate the friction characteristics of a given cylinder. This yields the following initial problem:

How to describe the friction found in a cylinder by using advanced friction models?

1.2 System description

In figure 1.1 the test bench is depicted, which consists of several components of interest. There are two differential cylinders mounted to the test bench frame and a sledge securing a horizontal travel. The cylinders are mounted horizontally to cancel out the gravitationally contribution. The cylinder to the left functions as the test cylinder for in which the friction will be investigated. The cylinder to the right is used as a controllable load. On the sledge, between the two cylinders, a load cell is placed attached with a strain gage.

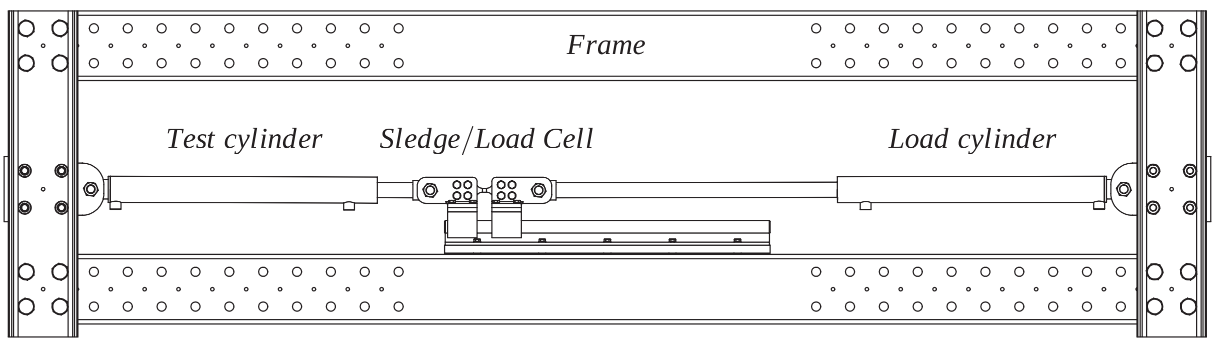

Figure 1.1: Test bench overview with some of the included parts.

As seen in the hydraulic diagram figure 1.2, there are placed three servo valves controlling the flow to the cylinders. The velocity of the cylinder is to be calculated from the position measurements obtained from the position sensor integrated in the test cylinder. To measure the pressures in the system, five pressure transducers are implemented in the setup, measuring the pressure in the cylinder chambers and the supply pressure. To control the system and collect data from the test system a DSP is connected to the pressure transducers, strain gage, position sensor and the valves. In table 1.1 the components are listed with manufacturers details.

Component	Manufacturer	Model
Accelerometer	Freescale Semiconductor	$MMA1250$
Strain gage	Tokyo Sokki Kenkyujo	$FCS-2-12$
Strain gage amplifier	RS Components	$435-692$
Position sensor	Hydra Tech	$PS6308$
DSP	Texas Instruments	$TMS320F28335PGFA$
DAC	Analog Devices	$AD5724R$
Pressure transducer	Parker	$MBS32-3615-1AB08$
Servo valve	MOOG	$D633-313A$
Cylinders	Hydra Tech	*Hydra Tech* 8054202 *CDA* 210 *Cyl* $40/25x400$
Pump	–	–

Table 1.1: Components present in the test setup

The hydraulic diagram on figure 1.2 depicts the system setup with mechanical and hydraulic components. The test cylinder is connected to a single valve, and the load cylinder is driven by a separate meter-in/separate meter-out setup including two servo valves identically to the one on the test cylinder.

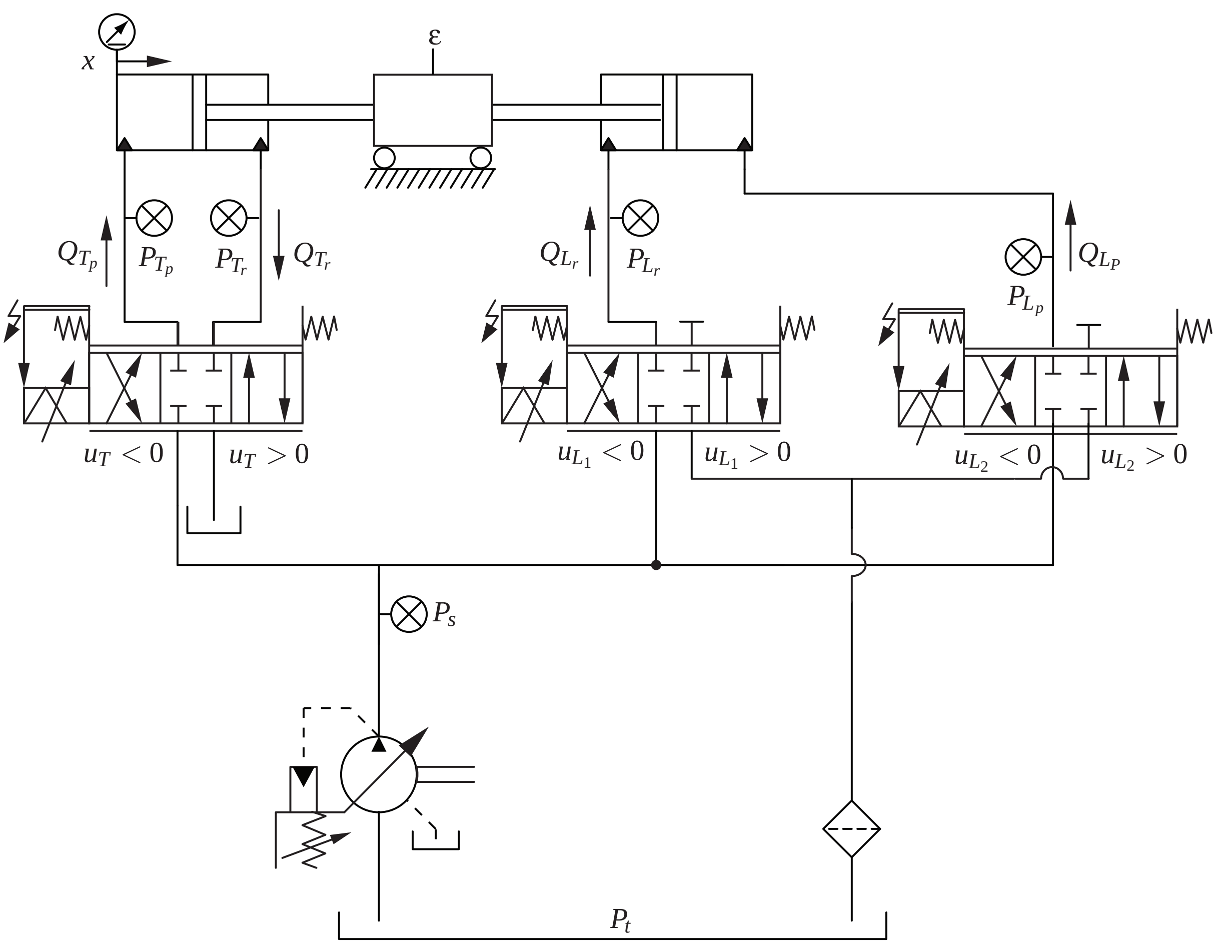

Figure 1.2: Hydraulic diagram of the test bench showing the implemented components.

Q_{Tp} :	Flow into the test cylinder on the piston side	$[m^3/s]$
Q_{Tr} :	Flow out of the test cylinder on the rod side	$[m^3/s]$
Q_{Lp} :	Flow into the load cylinder on the piston side	$[m^3/s]$
Q_{Lr} :	Flow into the load cylinder on the rod side	$[m^3/s]$
P_{Tp} :	Pressure in the test cylinders piston side chamber	$[Pa]$
P_{Tr} :	Pressure in the test cylinders rod side chamber	$[Pa]$
P_{Lp} :	Pressure in the load cylinders piston side chamber	$[Pa]$
P_{Lr} :	Pressure in the load cylinders rod side chamber	$[Pa]$
P_s :	Supply pressure	$[Pa]$
P_t :	Reservoir pressure	$[Pa]$
u_T :	Test cylinder valve voltage	$[V]$
u_{L_2} :	Load cylinder piston side valve voltage	$[V]$
u_{L_1} :	Load cylinder rod side valve voltage	$[V]$
x :	Position of the test cylinder piston	$[m]$
ε :	Strain of the load cell obtained by a strain gage	$[-]$

In figure 1.3 some of the electrical boards used in the setup is seen. Figure 1.3 includes a strain gage amplifier(1), DSP(4), pressure transducer/position amplifier(2), digital to analog converter(5) and a switch board(3) to enable another group to connect to the setup.

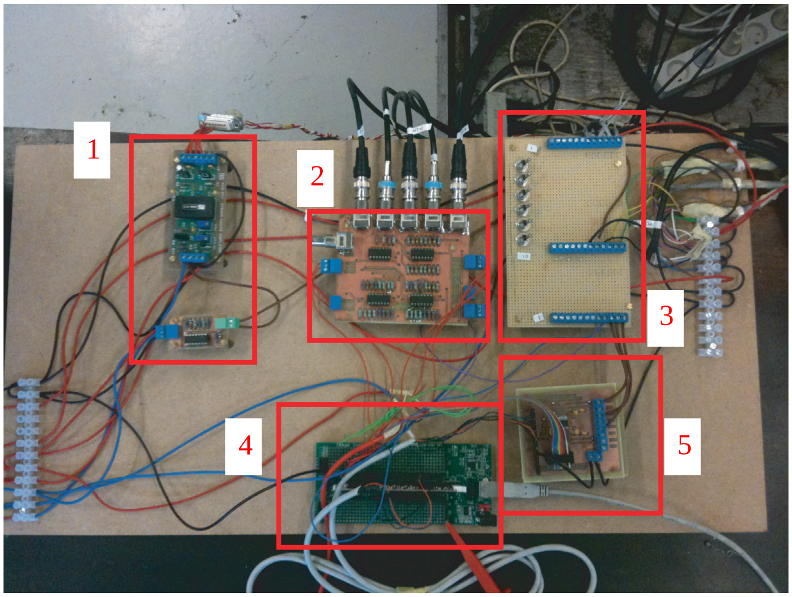

Figure 1.3: Picture of the electric components scaling the signals, and the DSP used for control/sampling.

The pressure transducer/position amplifier board, the secondary strain gage amplifier and the digital to analog converter board was developed in Altium Designer 6 and produced during the project period. The documentation of the amplifiers is located in *appendix B Electrical Circuit Boards*. The schematics and the printed circuit boards developed in Altium Designer is also located on the enclosed DVD under the *Altium Designer* folder.

1.3 Problem Specification

By taking the initial problem and the system description into account the problem specification, which are to be followed and dealt with throughout the report, can be specified:

- How should the test bench be modeled to be able to investigate the friction in detail?
- Which phenomena are present in the area of friction studies?
- What control strategy is suitable for implementation on the test bench so an adequate control is attained?
- Which friction models exist and which of them are most suited for the given setup?
- How would a standard approach for estimating the friction be specified?
- What is the efficiency of the given cylinder?

2 System Model

In this chapter the equations describing different relations in the system are presented. This is done by considering the system to consist of subsystems. Continuity equations are used to describe the control volumens *Test*- and *Load subsystems* which are presented in section 2.1 *Test-subsystem* and section 2.2 *Load-subsystem*. The *Shared subsystem* consist of the moving bodies which includes the cylinder pistons and the sledge. Their movement is described by Newtons second law of motion in section 2.3 *Shared-subsystem*. The equations for oil flow from the servo valves are presented in section 2.4 *Servo Valves*. In section 2.5 *Simulink Model* the nonlinear model, used to simulate the test bench and develop different controllers and suitable friction models, is introduced.

2.1 Test-subsystem

In this section the continuity equations for the test cylinder are presented. Moreover, associated assumptions are stated and variables used are explained. Subsequently, the continuity equations are solved for the pressure gradients. Figure 2.1 is a schematically overview of the test cylinder with the piston areas denoted A_{Tp} and A_{Tr}.

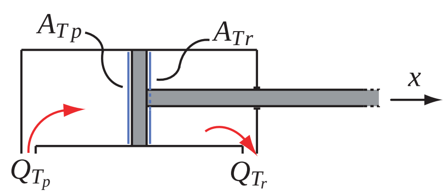

Figure 2.1: Schematic overview of the test cylinder.

2.1.1 Continuity Equation

The flow continuity equations are presented for the control volumes of the piston- and rod side of the test cylinder in equation 2.1 and equation 2.2, respectively.

$$Q_{Tp} - Q_{Tl} = \frac{dV_{Tp}}{dt} + \frac{V_{Tp}}{\beta}\frac{dP_{Tp}}{dt} \;;\; V_{Tp} = V_{Tp0} + A_{Tp}x \tag{2.1}$$

$$Q_{Tl} - Q_{Tr} = \frac{dV_{Tr}}{dt} + \frac{V_{Tr}}{\beta}\frac{dP_{Tr}}{dt} \;;\; V_{Tr} = V_{Tr0} + A_{Tr}\left(x_{Tstroke} - x\right) \tag{2.2}$$

Where,

Q_{Tl} :	Leakage flow over the test cylinder piston	$[m^3/s]$
V_{Tp} :	Volume on the test cylinders piston side	$[m^3]$
V_{Tr} :	Volume on the test cylinders rod side	$[m^3]$
V_{Tp0} :	Initial volume on the test cylinders piston side	$[m^3]$
V_{Tr0} :	Initial volume on the test cylinders rod side	$[m^3]$
A_{Tp} :	Piston area on the test cylinders piston side	$[m^2]$
A_{Tr} :	Piston area on the test cylinders rod side	$[m^2]$
$\dot{x}$:	Velocity of the cylinder piston	$[m/s]$
$x_{Tstroke}$:	Stroke length of the test cylinder	$[m]$
β :	Bulk modulus of the fluid	$[bar]$

As a simplification β is modeled as a constant. Assuming no leakage flow, $Q_{Tl} = 0$, the pressure gradients of the piston- and rod side are solved as seen in equation 2.3 and equation 2.4.

$$\dot{P}_{Tp} = \frac{\beta}{V_{Tp0} + A_{Tp}x}\left(Q_{Tp} - A_{Tp}\dot{x}\right) \quad (2.3)$$

$$\dot{P}_{Tr} = \frac{\beta}{V_{Tr0} + A_{Tr}\left(x_{Tstroke} - x\right)}\left(A_{Tr}\dot{x} - Q_{Tr}\right) \quad (2.4)$$

2.2 Load-subsystem

In this section the continuity equations and the derived pressures are presented, similarly as in section 2.1.1 *Continuity Equation*. Figure 2.1 is a schematically overview of the load cylinder with the piston areas denoted A_{Lp} and A_{Lr}.

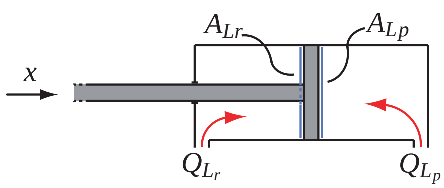

Figure 2.2: Schematic Overview of the load cylinder.

2.2.1 Continuity Equation

The continuity equations are presented for the control volumes of the piston- and rod side of the load cylinder in equation 2.5 and equation 2.6 respectively.

$$Q_{Lr} - Q_{Ll} = \frac{dV_{Lr}}{dt} + \frac{V_{Lr}}{\beta}\frac{dP_{Lr}}{dt} \; ; \; V_{Lr} = V_{Lr0} + A_{Lr}\left(x + x_0\right) \quad (2.5)$$

$$Q_{Lp} + Q_{Ll} = \frac{dV_{Lp}}{dt} + \frac{V_{Lp}}{\beta}\frac{dP_{Lp}}{dt} \; ; \; V_{Lp} = V_{Lp0} + A_{Lp}\left(x_{Lstroke} - x - x_0\right) \quad (2.6)$$

Where,

Q_{Ll} :	Leakage flow over the load cylinder piston	$[m^3/s]$
V_{Lp} :	Volume on the load cylinders piston side	$[m^3]$
V_{Lr} :	Volume on the load cylinders rod side	$[m^3]$
V_{Lp0} :	Initial volume on the load cylinders piston side	$[m^3]$
V_{Lr0} :	Initial volume on the load cylinders rod side	$[m^3]$
A_{Lp} :	Piston area on the load cylinders piston side	$[m^2]$
A_{Lr} :	Piston area on the load cylinders rod side	$[m^2]$
$x_{Lstroke}$	Stroke length of the load cylinder	$[m]$
x_0	Offset of the load cylinder position	$[m]$

Assuming no leakage flow, $Q_{Ll} = 0$, the pressure gradients of the piston- and rod side is solved as seen in equation 2.7 and equation 2.8.

$$\dot{P}_{Lr} = \frac{\beta}{V_{Lr0} + A_{Lr}(x + x_0)}(Q_{Lr} - A_{Lr}\dot{x}) \tag{2.7}$$

$$\dot{P}_{Lp} = \frac{\beta}{V_{Lp0} + A_{Lp}(x_{Lstroke} - x - x_0)}(Q_{Lp} + A_{Lp}\dot{x}) \tag{2.8}$$

2.3 Shared-subsystem

In this section Newtons second law of motion for the shared-subsystem is presented as seen in equation 2.9. A free body diagram for movement in positive direction is given in figure 2.3.

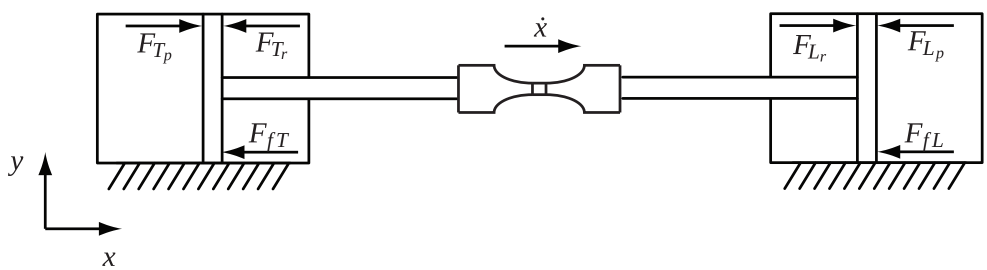

Figure 2.3: Free body diagram for positive velocity.

$$m_{eq}\ddot{x} = P_{Tp}A_{Tp} + P_{Lr}A_{Lr} - P_{Tr}A_{Tr} - P_{Lp}A_{Lp} - F_{f_{Total}} \tag{2.9}$$

$$m_{eq}\ddot{x} = F_T - F_L - F_{fT} - F_{fL} \tag{2.10}$$

Where,

F_{fTotal} :	Total friction force in the system	$[N]$
F_{fT} :	Friction contribution in the test cylinder	$[N]$
F_{fL} :	Friction contribution in the load cylinder	$[N]$
F_T :	Resulting pressure force of the test cylinder	$[N]$
F_L :	Resulting pressure force of the load cylinder	$[N]$
$\ddot{x}$:	Acceleration of the cylinder pistons	$[m/s^2]$
m_{eq} :	Total mass of moving bodies	$[kg]$

A force $F_{Applied}$ is introduced and derived by strain gage measurements.

$$F_{Applied} = F_L + F_{fL} \tag{2.11}$$

$$F_{fT} = F_T - F_{Applied} - m_{eq}\ddot{x} \tag{2.12}$$

2.4 Servo Valves

The test bench has three proportional servo valves implemented. The valve denoted *test valve* controls the flow to and from the test cylinder's piston- and rod side. The valves denoted *load valve 1* and *load valve 2* control the flow to the rod- and piston side of the load cylinder, respectively.

2.4.1 Test Valve

For an input voltage u_T, the static flow through the test valve is given as:

$$Q_{T_p} = \begin{cases} K_T \cdot u_T \cdot \sqrt{\frac{2}{\rho}\left(P_s - P_{T_p}\right)} & , \quad u_T \geq 0 \\ K_T \cdot u_T \cdot \sqrt{\frac{2}{\rho}\left(P_{T_p} - P_t\right)} & , \quad u_T < 0 \end{cases} \tag{2.13}$$

$$Q_{T_r} = \begin{cases} K_T \cdot u_T \cdot \sqrt{\frac{2}{\rho}\left(P_{T_r} - P_t\right)} & , \quad u_T \geq 0 \\ K_T \cdot u_T \cdot \sqrt{\frac{2}{\rho}\left(P_s - P_{T_r}\right)} & , \quad u_T < 0 \end{cases} \tag{2.14}$$

Where,

K_T :	Valve gain	$-$
ρ :	Density of the system fluid	$[kg/m^3]$

The valve gain, K_T is calculated with rated values found in the data sheet for the MOOG D633 servo valve. The data sheet is found in the enclosed DVD in the *Data Sheets* folder.

$$K_T = \frac{Q_N}{u_{\%}\sqrt{\frac{2\Delta p_N}{\rho}}} \tag{2.15}$$

Note: The index T is in this case not an indication of which subsystem it belongs to, but merely the same notation as used in the data sheet for the valves. The valve gain, K_T is the same value for all three valves.

At 100% valve opening the rated pressure drop is $\Delta p_N = 35\ [bar]$ and the rated flow is $Q_N = 40\ [l/min]$. As the valve is a proportional servo spool valve, a 100% oppening is given at maximum voltage $u_{100\%} = 10[V]$. This results in the following valve gain $K_T = 7.43 \cdot 10^{-7}$.

As the plunger in the valves has a dynamic response, this has to be modeled as well. The transfer function is developed and is presented in equation 2.16.

$$G_{valve}(s) = \frac{1}{\frac{1}{\omega_{valve}^2}s^2 + \frac{2\zeta_{valve}}{\omega_{valve}}s + 1} \tag{2.16}$$

Where,

ω_{valve} :	The eigenfrequency of the valves	$[rad/s]$
ζ_{valve} :	The damping of the valves response	$[-]$

These constants are determined to $\omega_{valve} = 90\ [Hz]$ and $\zeta_{valve} = 1$.

To illustrate the valve operation, a cross section of the valve is shown in figure 2.4 with a positive voltage applied, that is $u_T > 0$. This causes the valve-plunger to displace making a passageway between the supply and piston side. The reservoir will then be connected to the rod side of the test cylinder.

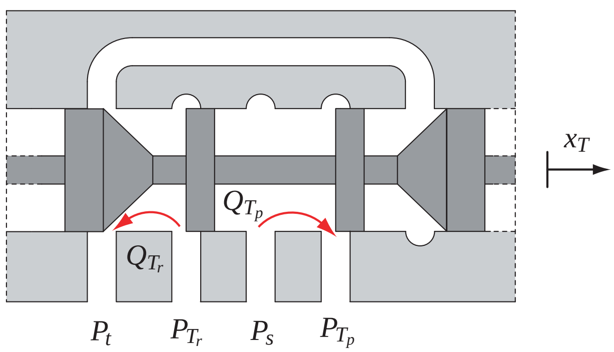

Figure 2.4: Servo valve for the test cylinder with a positive applied voltage.

2.4.2 Load Valve 1

For input voltages u_{L_1}, the static flow through load valve 1 is expressed as seen in equation 2.17.

$$Q_{L_r} = \begin{cases} K_T \cdot u_{L_1} \cdot \sqrt{\frac{2}{\rho}(P_s - P_{L_r})} & , \quad u_{L_1} \geq 0 \\ K_T \cdot u_{L_1} \cdot \sqrt{\frac{2}{\rho}(P_{L_r} - P_t)} & , \quad u_{L_1} < 0 \end{cases} \tag{2.17}$$

The dynamic response for load valve 1 is modeled in the same manner, as for the test valve with the transfer function found in equation 2.16.

2.4.3 Load Valve 2

For input voltages u_{L_2}, the static flow through load valve 2 is expressed as seen in equation 2.18.

$$Q_{L_p} = \begin{cases} K_T \cdot u_{L_2} \cdot \sqrt{\frac{2}{\rho}\left(P_s - P_{L_p}\right)} & , \quad u_{L_2} \geq 0 \\ K_T \cdot u_{L_2} \cdot \sqrt{\frac{2}{\rho}\left(P_{L_p} - P_t\right)} & , \quad u_{L_2} < 0 \end{cases} \tag{2.18}$$

The dynamic response for load valve 2 is also modeled in the same manner, as for the test valve with the transfer function found in equation 2.16.

2.5 Simulink Model

To simulate how the system reacts to given inputs, the test bench is modeled in Simulink. This model is then later used to analyze the effect of different controllers on the system, before they are implemented in the test rig. By implementing different friction models in the Simulink model and comparing simulated results with actual results from the test rig, the friction model which yields the most realistic results can be found. The complete Simulink model and the MATLAB files can be found on the enclosed DVD.

Figure 2.5 illustrates the Simulink model and the signal routing is read from left to right.

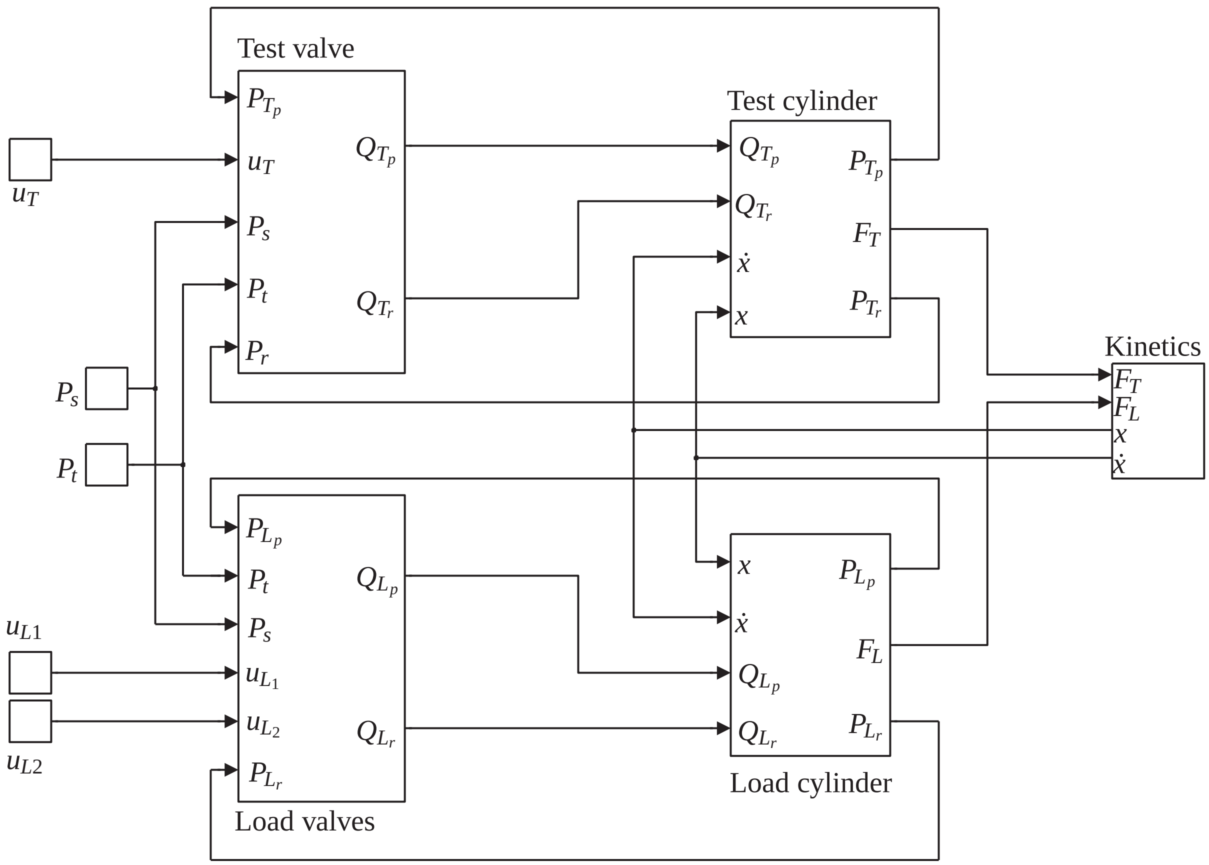

Figure 2.5: Simulink system diagram.

The model receives the signal voltages u_T, u_{L_1} and u_{L_2} which can be controlled in an interval between ± 10 $[V]$ as described in section 2.4. The oil flow from the valve blocks are fed to the cylinder blocks, where the pressure build up is calculated through use of the continuity equations described in the sections 2.1.1 and 2.2.1. The resulting force for each cylinder, calculated from the chamber pressures, derived by integrating the pressure gradients, are fed from the cylinder blocks into the kinetic block. The kinetic block equates the motion of the system, based on Newtons second law of motion for the moving bodies presented in section 2.3 *Shared-subsystem*. Moreover, the friction models investigated, are included in the *Kinetics*-block.

3 Friction Modelling

When investigating the friction produced by the cylinder seals and the relative motion of the cylinder piston, a detailed understanding of the physical phenomenon is essential. In this chapter a general description of the friction phenomena is given. In the first part of the chapter the nature of friction is investigated by considering the phenomena documented in earlier studies of friction. The second part is reviewing some of the friction models and assumptions made in these.

3.1 Friction Phenomena

Friction is a force phenomenon which opposes relative movement between to surfaces in contact.

General characteristics of the friction contributions are presented in figure 3.1, where the friction force is shown as a function of the velocity.

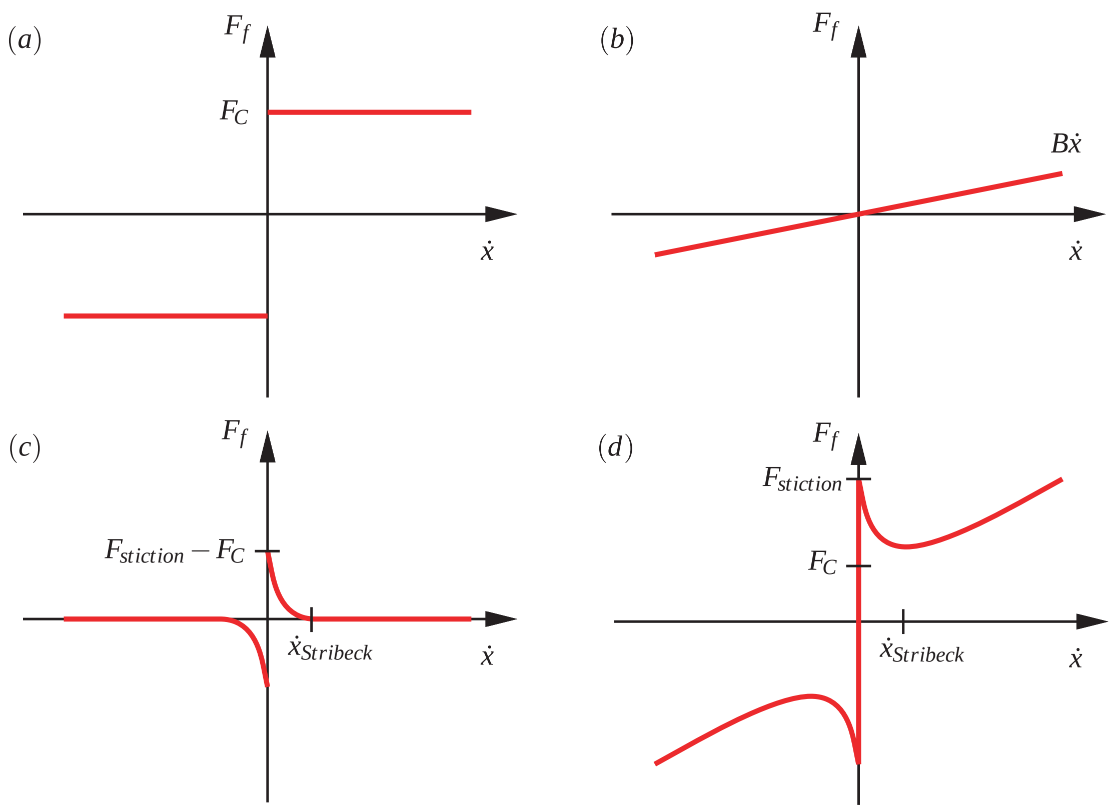

Figure 3.1: Figure illustrating some of the friction contributions and the combined friction.

Graph *a* in figure 3.1 is illustrating the Coulomb friction. The Coulomb friction is a constant friction contribution and thereby not dependent on the velocity.

The viscous friction is assumed to be proportional to the velocity, why the viscous friction contribution is expressed as a function of a viscous friction coefficient B multiplied with the velocity as seen in graph *b*, figure 3.1.

A friction phenomenon influencing the operation at low velocities is the Stribeck effect as seen on graph *c*. The Stribeck effect is a friction contribution at low velocities, which is decreasing exponentially from the difference between the stiction (*maximum static friction level*) and the Coulomb force to zero [Armstrong-Hélouvry et al., 1994].

Graph *d* in figure 3.1 illustrates the total friction force consisting of the three friction contributions shown on graph *a*, *b* and *c*.

It is common, in the study of friction, to refer to a curve of the combined friction as a function of velocity by *Stribeck friction curve* or simply *Stribeck curve* [Armstrong-Hélouvry et al., 1994].

3.1.1 Stribeck Friction Regimes

A Stribeck curve is illustrating the friction dependence upon velocity. Stribeck curves are often generated by steady state velocity data so initial friction behavior can be eliminated. The friction seen on the Stribeck friction can be divided into four regimes as seen on figure 3.2.

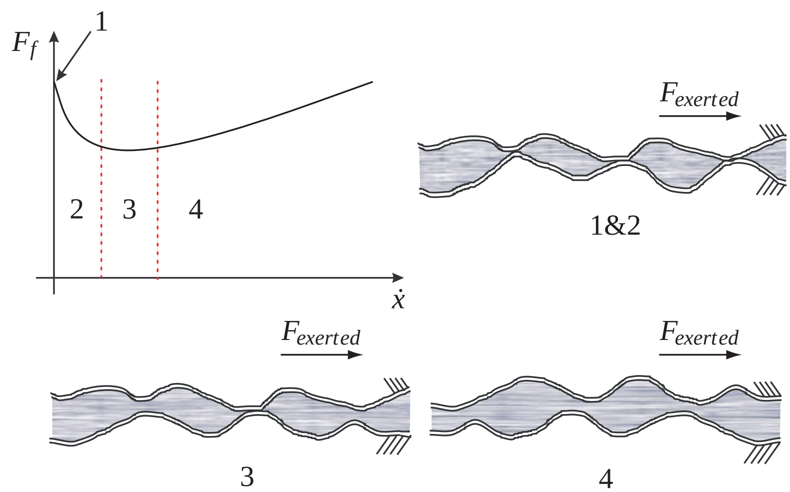

Figure 3.2: Stribeck friction curve divided into four regimes. Modified from [Márton and Lantos, 2006]

The first regime is the *stiction*, where the surface asperities deform elastically and there is no displacement until the exerted load force $F_{exerted}$ reaches the stiction level, entering the second regime, as seen in the graph in figure 3.2.

The second regime is the *boundary lubrication*. Both the stiction and boundary lubrication regimes are solid to solid friction, and the velocity (very low) has not yet reached a level where a consistence film layer has been developed. The oil is primarily functioning as a lubricant. Boundary lubrication is a process of the shear in the solids, and thus the shear strength normally is greater for solids than fluids the friction is greater than for the third regime, [Armstrong-Hélouvry et al., 1994]. The appearance of the Stribeck curve can differ under different lubrication situations as seen in figure 3.3.

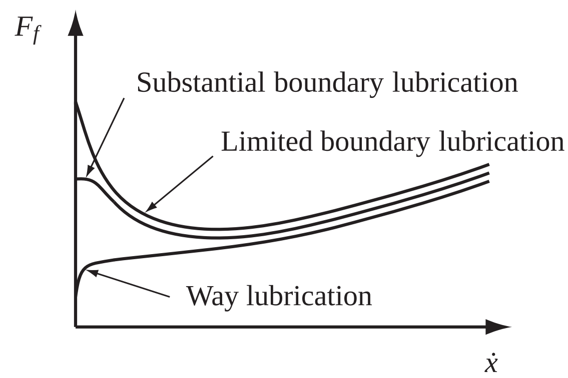

Figure 3.3: Stribeck curves dependent on the boundary lubrication.

From this, can be derived that the lubricant, the hydraulic oil, used has an important impact on the friction in the regime dominated by boundary lubrication.[Armstrong-Hélouvry et al., 1994]

Another factor influencing the friction in the boundary lubrication regime is the geometry of the cylinder piston as stated in [Meikandan et al., 1994]. This means that the characteristics of the cylinder friction can vary depending on the type of the oil, seals and piston geometry in the boundary lubrication regime. The upcoming theory will be based on the *Limited Boundary Lubrication* as many of the friction models are derived from this characteristic. From [Kato et al., 1998] it is noted that the normal load affects the regimes in which solid to solid contact is present. It is assumed that the seals are expanding under high pressure resulting in a higher normal load and friction. To investigate the load dependence a series of Stribeck curves are to be generated with different load situations.

When considering the asperities they are often modeled as springs. Until the stiction level is reached all the springs are acting as linear elastic springs. When the relative motion occurs, some of these springs are canceled as there is no solid to solid contact between two given asperity junctions, figure 3.4.

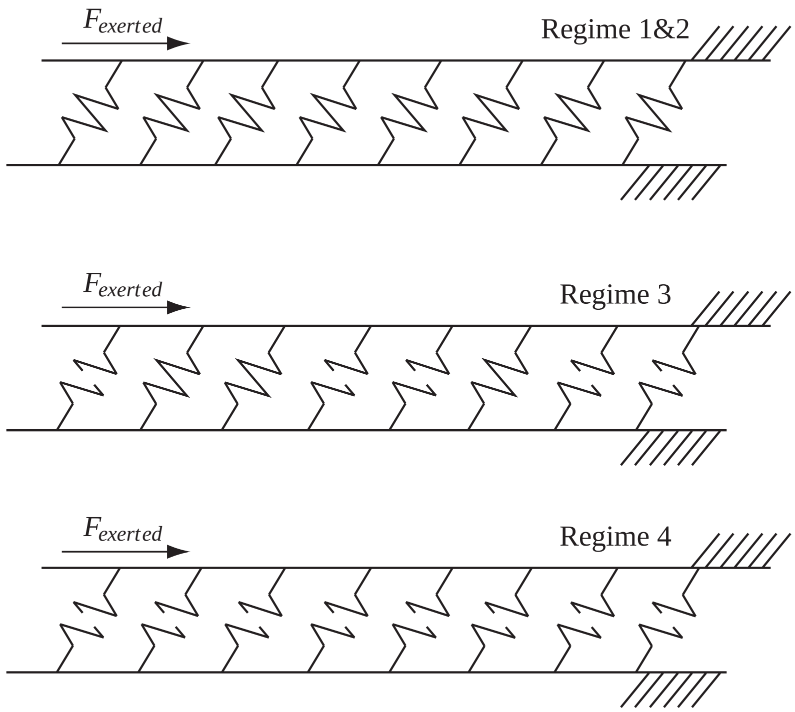

Figure 3.4: Model hypothesis of the surface asperities behavior.

Partial fluid lubrication is the third regime and in this regime lubrication is forced between the solids by their relatively motion. Solid on solid friction can still occur.

When the fluid film has grown beyond the height of the aspirates and the load is supported only by the fluid a new regime is entered. This is the *full fluid lubrication* regime and is the fourth regime where the viscous friction is dominant.

In the full fluid lubrication friction regime the dynamic viscosity of the fluid, the velocity and contact area of the moving object determine the friction force to be overcome. This phenomenon is also known as drag force.

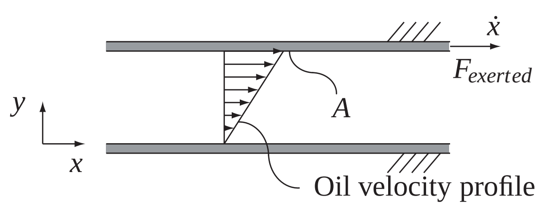

Figure 3.5: Velocity profile of an oil film separating a stationary plate from a moving one.

In figure 3.5 a velocity profile is shown for an oil film separating a stationary plate from a moving one. The oil is a Newtonian fluid and the shear stress is therefore proportional to the rate of deformation, resulting in the velocity profile from figure 3.5. To maintain a constant velocity a constant force must be exerted because of the internal resistance of the oil, equation 3.1. [Çengel and Turner, 2005].

$$F_{exerted} = A\tau = A\mu \frac{d\dot{x}}{dy} \tag{3.1}$$

Where τ is the shear stress of the fluid, μ is the dynamic viscosity and A is the contact area of the moving object in contact with the fluid. The force needed to maintain a constant velocity is the same magnitude as the viscous friction force but in opposite directions.

3.1.2 Friction Lag

Early studies proved that a time lag can be observed in friction when a change in velocity or load force is applied. The delay can vary from milliseconds to seconds. When observing figure 3.6, showing the Stribeck curve, a presumption could be made that the friction would be an instantaneously reaction of the velocity as in figure 3.7. However, the friction is actually lagging the velocity as in figure 3.8.[Armstrong-Hélouvry et al., 1994]

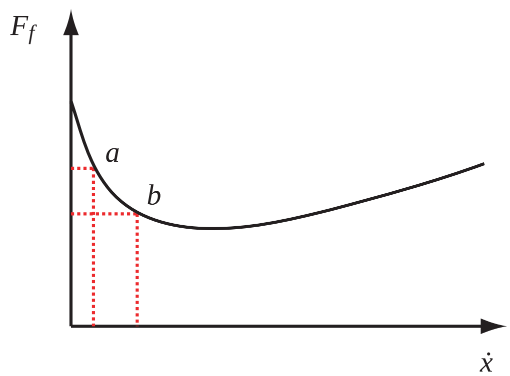

Figure 3.6: Stribeck curve. Point *a* and *b* are used in figure 3.7 and 3.8 to describe the friction lag.

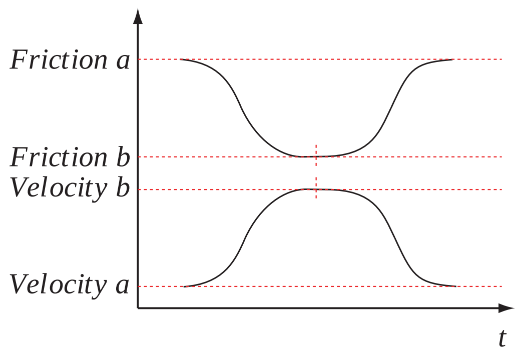

Figure 3.7: Friction as a function of velocity without lag.

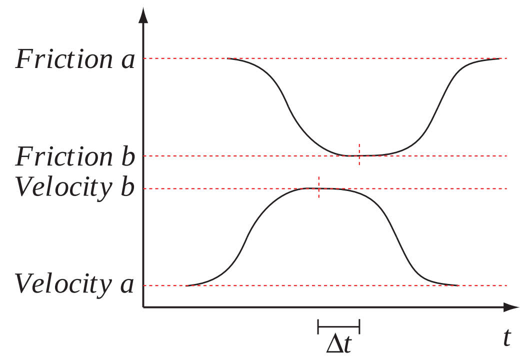

Figure 3.8: Friction as a function of velocity with lag.

As can be observed in figure 3.8 a lag in the friction force is present when a change in the velocity occurs. This is assumed to be because of the time needed for the new height of the film thickness to be established, this phenomenon is also known as the *squeeze effect*. The film thickness develops slowly and decreases rapidly while accelerating and decelerating respectively, hence the frictional force will have a different time lag depending on whether an acceleration or deceleration has occurred. [Al-Bender, 2005]

3.1.3 Friction Hysteresis

Hysteresis refers to a system that may exhibit path- or/and rate dependent memory. Friction hysteresis is caused by friction lag and the fact that boundary film layer develops and decreases at different rates depending on the velocity and applied force, amongst other factors.

Friction hysteresis is apparent, when the friction force is plotted as a function of the position or velocity of the system, in form of *hysteresis loops*. A such loop can be seen in figure 3.9.

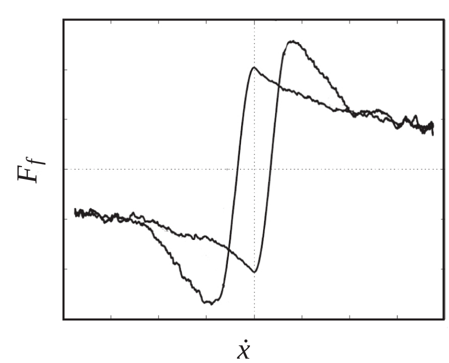

Figure 3.9: A typical rate dependent hysteresis loop. Modified from [Al-Bender, 2005]

It should be noted that the development of a such loop, is not only dependent on given inputs, but also on previous inputs and states. The shape of hysteresis loops can thus differ depending on the properties of the system.

The distinction between *local* and *nonlocal* memory is made when considering the modelling of the loops, and is the difference whether or not it is able to model hysteresis loops within a larger loop, respectively [Dennis S. Bernstein, 2011*].

A position dependent hysteresis loop with the nonlocal memory aspect is presented in figure 3.10.

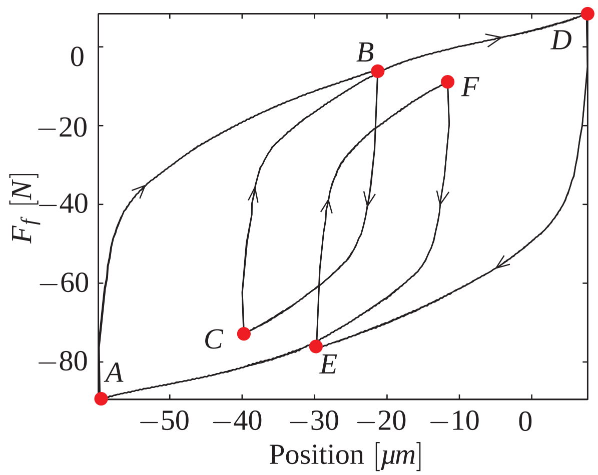

Figure 3.10: The relation between the position and hysteresis force depicting the hysteresis memory aspect. Modified from [Lambert et al., 2002]

Figure 3.10 illustrates measurements of the hysteresis force plotted as as a function of the measured position performed by [Lambert et al., 2002]. At every *new* point from A to F the sign on the velocity reference is changed. As seen, this creates hysteresis loops within the bigger loop. These loops illustrate the hysteresis nonlocal memory aspect: When an internal loop is closed the system behaves as if the closed loop never occurred.

3.1.4 Stick-Slip Motion

Stick-slip motion occurs at close to zero velocity and is apparent in the form of sudden jerking motion. Considering an object at rest on which an external load is applied and increased until the stiction level is reached. As the object starts to move relatively to a surface in contact, the friction transcends from static to dynamic friction level which is, for limited boundary lubrications, a lower value. The external force applied is then decreased until the force is insufficient to sustain the motion and the object is brought to a hold at which point the cycle is repeated. This is also illustrated in figure 3.11.

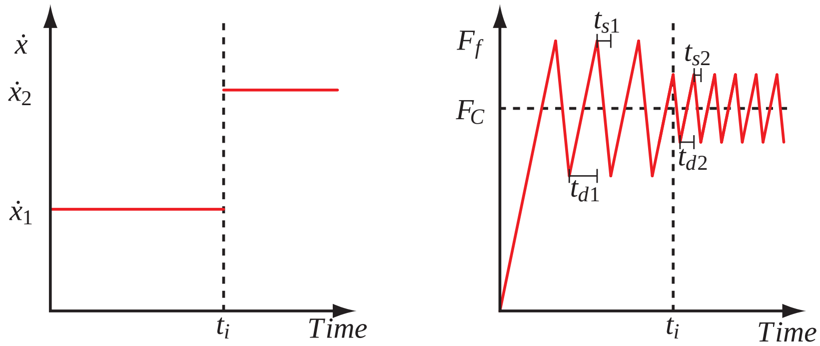

Figure 3.11: Stick slip.

As illustrated, a low average velocity, depicted by $\dot{x}_1$, results in a high difference in friction force and this leads to a more apparent stick slip motion. The time the object is at rest is referred to as the dwell time an is denoted by t_d, likewise is the time when slipping occurs called the slip time denoted by t_s.

3.2 Friction Models

When considering which friction model to employ in the present study, an overview of some of the existing models is essential.

3.2.1 The Márton and Lantos Model

In the identification and model-based compensation of Stribeck friction done by Lõrinc Márton and Béla Lantos a linearized friction model is applied. A linearized friction model eases the implementation in a simulation model. The model by Márton and Lantos originates from the Tustin friction model seen in equation 3.2.

$$F_f = \operatorname{sign}(\dot{x}) \left(F_C + (F_{stiction} - F_C)\, e^{-\frac{|\dot{x}|}{\dot{x}_{stribeck}}} \right) + B\dot{x} \tag{3.2}$$

The parameters used in the Tustin model can be found both for the positive and negative friction regime, but will only be covered for the positive in the following. The discussed model makes use of the linear tendency of the Tustin exponential model as the velocity evolves towards infinity. In figure 3.12 a linear function F_{d2} is given covering the high velocity regime of the friction, and thereby the fourth Stribeck curve regime.

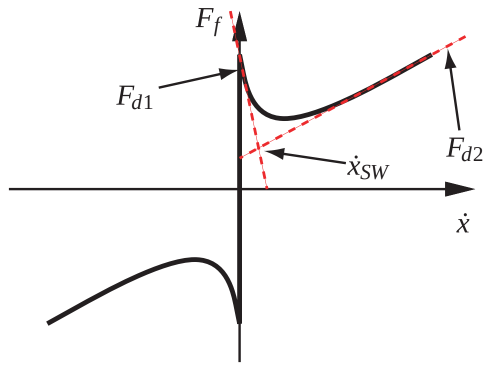

Figure 3.12: Two linear functions approximating the friction force.

It is obvious that the linear approximation F_{d2} diverges significantly at low velocities. To model the friction at low velocities a second linear function F_{d1} is derived, decreasing from the stiction level. F_{d1} and F_{d2} can approximately describe the friction force progress from the low velocity regime influenced by stiction to the high velocity regime approximating the simple viscous friction. Introducing the switching velocity $\dot{x}_{SW}$, where the two linear functions intersect, constitutes the friction model presented in equation 3.3.[Márton and Lantos, 2006]

$$F_f = \begin{cases} F_{d1} & if \quad 0 \leq \dot{x} \leq \dot{x}_{SW} \\ F_{d2} & if \quad \dot{x}_{SW} < \dot{x} \end{cases} \tag{3.3}$$

By linearization of the Tustin model, the parameters for the two linear functions can be obtained.

$$F_{d_1} = F_{stiction} + \left.\frac{\partial F_{Tustin}(\dot{x})}{\partial \dot{x}}\right|_{\dot{x}=0} \dot{x} = \overbrace{F_{stiction}}^{a_{d_1}} + \overbrace{\left(\frac{F_C - F_{stiction}}{\dot{x}_{Stribeck}} + B\right)}^{b_{d_1}} \dot{x} \tag{3.4}$$

$$\begin{aligned} F_{d_2} &= F_f(\dot{x}_{max}) + \left.\frac{\partial F_{Tustin}(\dot{x})}{\partial \dot{x}}\right|_{\dot{x}=\dot{x}_{max}} (\dot{x} - \dot{x}_{max}) \\ &= \overbrace{F_f(\dot{x}_{max})}^{a_{d_2}} + \overbrace{\left(B + \frac{(F_C - F_{stiction})}{\dot{x}_{Stribeck}} e^{\frac{-|\dot{x}_{max}|}{\dot{x}_{Stribeck}}}\right)}^{b_{d_2}} (\dot{x} - \dot{x}_{max}) \end{aligned} \tag{3.5}$$

$\dot{x}_{max}$ is the maximum velocity present in the data generating the Stribeck curve. The switch velocity deciding which linear function to use is given in equation 3.6.

$$\dot{x}_{SW} = \frac{a_{d_1} - a_{d_2}}{b_{d_2} - b_{d_1}} \tag{3.6}$$

Having two options when calculating the friction leads to a switching in the control strategy. In the same manner as for the positive regime two linear functions can also be derived for the negative velocity.

3.2.2 The Pressure-Based Model

In the tribology literature many of the friction models are only velocity dependent, but in hydraulic cylinders the pressure is assumed to have a significant influence on the friction. By implementing the chamber pressures, the effect of the elastomeric seals can be accounted for. In [Bonchis et al., 1999] a friction model using the chamber pressures and the piston velocity was formulated. This model is presented in equation 3.7.

$$F_f = k_1 e^{k_2 \dot{x}} + k_3 (P_p - P_r) + k_4 P_r + k_5 \dot{x} \tag{3.7}$$

The constants k_{1-5} are to be determined from test data. When applying equation 3.7 it is clear that the friction during contraction will differ from expansion, as thought to be valid for differential cylinders. The pressure-based model is affected by external load variation in contrast to the velocity dependent models.

In figure 3.13 it can be seen how the seals are expected to influence the friction.

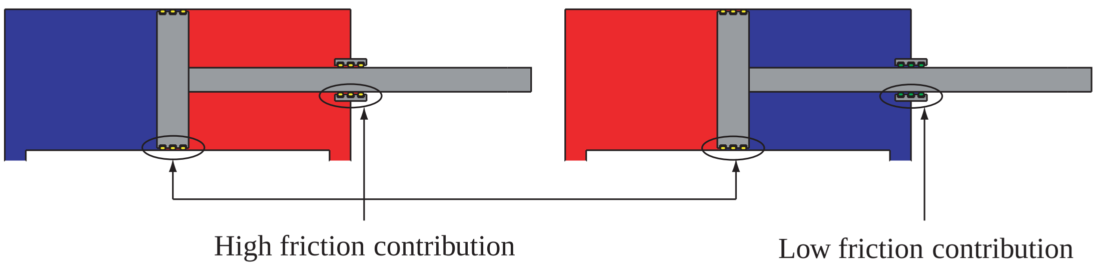

Figure 3.13: Pressure influence on the seals. High pressure is illustrated by the colour red, and low pressure is blue.

Compared with for example the LuGre and Leuven model the pressure-based model is simpler but has also no considerable improvement from the classical viscous-Coulomb friction model as shown in [Bonchis et al., 1999].

3.2.3 The LuGre Model

The LuGre model was developed by [de Wit et al., 1995]. Besides being able to model the Stribeck effect, it also accounts for the friction force generated when deformation of asperity junctions occur. Another aspect of this model is the ability to simulate presliding *spring-like* displacement and hysteresis loops.

The asperity junctions are in the LuGre model considered as bristles which is illustrated in figure 3.14. For simplicity, the bristles in one of the two, relative to each other, moving surfaces are modeled as rigid and the bristles on other surface are modeled as elastic.

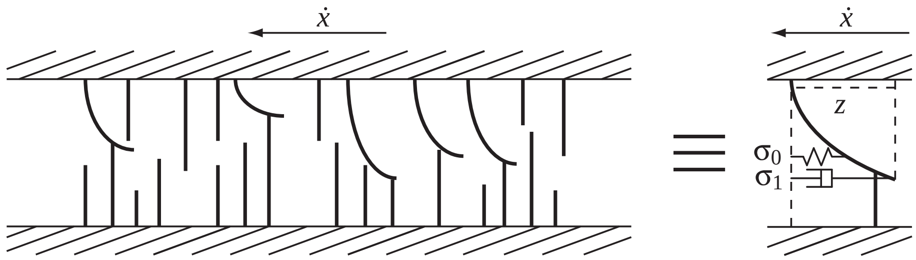

Figure 3.14: Bristle modelling.

The parameter σ_1 is the micro-viscous coefficient which is equivalent to a damping coefficient. The parameter σ_0 is the average stiffness of the bristles.

The average deflection of the deformable elastic bristles is denoted by z and the rate of deflection $\dot{z}$ is modeled by equation 3.8.

$$\dot{z} = \dot{x} - \frac{|\dot{x}|}{g(\dot{x})} z \tag{3.8}$$

Where,

$$g(\dot{x}) = \frac{1}{\sigma_0}\left(F_C + (F_{stiction} - F_C)\, e^{-\left(\frac{|\dot{x}|}{\dot{x}_{Stribeck}}\right)^{\delta}}\right) \tag{3.9}$$

Where δ is an arbitrary constant which is geometry dependent and often set to unity. The steady state deflection z_{ss} is described by equation 3.10.

$$z_{ss} = sign(\dot{x})\, g(\dot{x}) \tag{3.10}$$

The friction force generated when bending the bristles is described by equation 3.11.

$$F_{f,bristles} = \sigma_0 z + \sigma_1 \dot{z} \tag{3.11}$$

The final LuGre model emerges when adding the viscous friction term $B\dot{x}$ to equation 3.11 and is presented in equation 3.12.

$$F_f = \sigma_0 z + \sigma_1 \dot{z} + B\dot{x} \tag{3.12}$$

Note the steady state friction force $F_{f,ss}$ arises when the velocity $\dot{x}$ is held constant and can be expressed by equation 3.13.

$$\begin{aligned} F_{f,ss} &= \sigma_0 z_{ss} + B\dot{x} \\ &= \sigma_0 sign(\dot{x})\, g(\dot{x}) + B\dot{x} \\ &= sign(\dot{x})\, F_C + (F_{stiction} - F_C)\, e^{-\left(\frac{|\dot{x}|}{\dot{x}_{Stribeck}}\right)^{\delta}} + B\dot{x} \end{aligned} \tag{3.13}$$

3.2.4 The Modified Leuven Model

The original Leuven model is a white box model, originated from the LuGre model and attempts to incorporate nonlocal memory.

The modified Leuven model is a grey box model as the hysteresis force is to be calculated on-line while operating.

The modified Leuven model *(a.k.a. the Maxwell-Slip Friction Model)* can be considered as one of the *state of the art* friction models. This model is very comprehensive and includes accurate modelling in the presliding and sliding regimes. Moreover, the model incorporates a hysteresis function with nonlocal memory, which is defined as an input-output relationship for which the output at any time instant not only depends on the previous inputs and outputs, but also on past extremum values as well [Swevers et al., 2000].

The modified Leuven model equation consists of three terms as seen in equation 3.14.

$$F_f = F_h(k) + \sigma_1 \dot{z} + B\dot{x} \tag{3.14}$$

$F_h(k)$ is the hysteresis force. The middle term[1] is *the micro viscous term* with the micro viscous damping coefficient σ_1 multiplied with the derived average deflection of the asperity junctions $\dot{z}$, first mentioned in section 3.2.3 *The LuGre Model*. The derived deflection is modeled as seen in equation 3.15.

$$\dot{z} = \dot{x}\left(1 - sign\left(\frac{F_h(k)}{S(\dot{x})}\right)\left|\frac{F_h(k)}{S(\dot{x})}\right|^n\right) \tag{3.15}$$

The n is an arbitrary parameter which can be used to shape the transition curves. As seen in equation 3.15 another function $S(\dot{x})$is presented. This function is used to model the constant velocity behavior. This function is expressed as seen in equation 3.16 and is much similar to the *Tustin Model* presented in section 3.2.1 *The Márton and Lantos Model.*

$$S(\dot{x}) = sign(\dot{x})\left(F_C + (F_{stiction} - F_C)\, e^{-\left(\frac{|\dot{x}|}{\dot{x}_{stribeck}}\right)^{\delta}}\right) \tag{3.16}$$

By implementing the Maxwell Slip model, the asperity junctions can be considered as a N number of elastoslide elements in parallel with no mass.

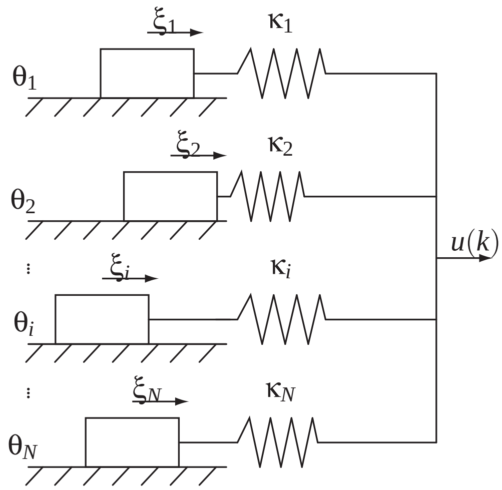

Figure 3.15: Maxwell Slip model for N elements.

As illustrated each element is considered attached to a spring which has a spring constant, κ_i. The position of each element is denoted $\xi_i(k)$. The small piston displacement is measured and denoted with $u(k)$ and the Coulomb force for each element is denoted θ_i. The index k is simply the newest measured value and $k-1$ is the previous measured value.

The deformation $\delta_i(k)$ of each spring can be expressed as the difference between the small piston displacement $u(k)$ and the position of each element $\xi_i(k)$ as seen in equation 3.17

$$\delta_i(k) = u(k) - \xi_i(k) \tag{3.17}$$

The ratio $y_i(k)$ between the spring deformation $\delta_i(k)$ and the maximum spring deformation Δ_i (*when the spring force equals the Coulomb force* θ_i) can be expressed as seen in equation 3.18 or equation 3.19 depending on the conditions.

$$\left.\begin{aligned} y_i(k) &= \tfrac{\delta_i(k)}{\Delta_i} \\ \xi_i(k+1) &= \xi_i(k) \end{aligned}\right\} \quad if\,|\delta_i(k)| < \Delta_i \tag{3.18}$$

$$\left.\begin{aligned} y_i(k) &= \mathrm{sign}(\delta_i(k)) \\ \xi_i(k+1) &= u(k) - \mathrm{sign}(\delta_i(k))\Delta_i \end{aligned}\right\} \quad else \tag{3.19}$$

From equation 3.17 to equation 3.19 can be noted that $y_i \in [-1,1]$ and assuming the initial position of each element to be zero, yielding: $\xi_i(k) = 0$ until $|\delta_i(k)| > \Delta_i$.

The maximum spring deformations Δ_i are considered to be equally distributed over the number of elements N. That is $\Delta_i = {}^{i}\!/_{N}$.

Considering the ratios y_i, and the Coulomb forces θ_i to be vectors denoted by Φ and Θ, respectively, that is $\Phi = [y_1 \,..\, y_i \,..\, y_N]^T$ and $\Theta = [\theta_1 \,..\, \theta_i \,..\, \theta_N]^T$, the hysteresis force can be expressed as seen in equation 3.20.

$$F_h(k) = \sum_i^N \theta_i y_i(k) = \Theta(k)^T \Phi(k) \tag{3.20}$$

To obtain better estimates of the Coulomb vector Θ the recursive least square method *(RLS)* is incorporated as seen in equation 3.21 to equation 3.23.

$$\Theta(k) = \Theta(k-1) + L(k)\left[F_h(k) - \Theta(k)^T(k-1)\Phi(k)\right] \quad (3.21)$$

$$L(k) = \frac{P(k-1)\Phi(k)}{\lambda(k)\Phi^T(k)P(k-1)\Phi(k)} \quad (3.22)$$

$$P(k) = \frac{1}{\lambda(k)}\left[P(k-1) - L(k)\Phi^T(k)P(k-1)\right] \quad (3.23)$$

The matrix $P(k)$ is the covariance matrix of the Coulomb parameters and $L(k)$ is a gain vector. The forgetting factor $\lambda(k)$ is influencing the values of $P(k)$ and $L(k)$. If $\lambda(k)$ obtains a small value the gain vector $L(k)$ will be large, and therefore the change in the parameters has more impact on Θ. The hysteresis force $F_h(k)$ is measured and used to obtain new approximations for Θ as seen in equation 3.21. This measurement can also be used to express the recursive model error $E(\Theta)$, as seen in equation 3.24.

$$E(\Theta) = \frac{1}{M}\sum_{k=1}^{M}\left(F_h(k) - \Theta^T(k)\Phi(k)\right)^2 \quad (3.24)$$

Where, M is the number of samplings up to and including sampling k.

4 System Control

To conduct experiments on the test bench, control strategies are to be derived. From section 3.1.1 *Stribeck Friction Regimes* it can be concluded that test runs are to be carried out where data of the friction force and velocity are logged, why it is evident that a control of the piston velocity is developed. Furthermore, the load applied on the test cylinder, from the load cylinder, is considered to have an impact on the friction, why the resulting force of the load cylinder must be controlled.

4.1 Linear Model

Before controllers for the MOOG valves, used on the friction test bench, can be developed, a linear model of the system must be derived. This linear model has to be transformed into the Laplace domain to construct a block diagram of the linear system and derive the transfer functions.

4.1.1 Equation Of Motion

The equation of motion, first presented in equation 2.9 on page 11 is to be transformed into the Laplace domain. To obtain what is expected to be satisfactory controller performance, the simple Coulomb-viscous friction model is estimated to be sufficient. The Coulomb friction can be neglected when evaluating the dynamics of the system because of the constant contribution. The equation of motion, equation 4.1, is transformed into the Laplace domain in equation 4.2, and the velocity of the piston is isolated in equation 4.3.

$$m_{eq}\ddot{x} = \overbrace{P_{T_p}A_{T_p} - P_{T_r}A_{T_r}}^{F_T} \overbrace{-P_{L_p}A_{L_p} + P_{L_r}A_{L_r}}^{F_L} - \overbrace{(B_T + B_L)}^{B}\dot{x} - \overbrace{\left(\cancel{F_{C_T} + F_{C_L}}^{\,0}\right)}^{F_C} \tag{4.1}$$

$$m_{eq}X(s)s^2 = F_T + F_L - BX(s)s \tag{4.2}$$

$$X(s)s = \frac{F_T + F_L}{m_{eq}s + B} \tag{4.3}$$

4.1.2 Test Cylinder Pressures

The pressure gradient equations are nonlinear, why the derived linearized equations are only valid in a limited range from a given evaluation point. The linearized pressure gradient equations are Laplace-transformed and the pressures isolated in equation 4.6 and 4.7. The over-lined parameters are specific values denoting the operating point used in the control chapter.

$$\dot{P_{T_p}} = \frac{\left(Q_{T_p} - A_{T_p}\dot{x}\right)\beta}{V_{T_P0} + A_{T_p}x} \tag{4.4}$$

$$\dot{P_{T_r}} = \frac{\left(A_{T_r}\dot{x} - Q_{Tr}\right)\beta}{V_{T_r0} + A_{T_r}\left(x_{Tstroke} - x\right)} \tag{4.5}$$

$$P_{T_p}(s) = \frac{\left(Q_{T_p} - A_{T_p}X(s)s\right)\beta}{\overline{V}_{T_P}s} \tag{4.6}$$

$$P_{T_r}(s) = \frac{\left(A_{T_r}X(s)s - Q_{T_r}\right)\beta}{\overline{V}_{T_r}s} \tag{4.7}$$

4.1.3 Load Cylinder Pressures

The pressure gradient equations for the load cylinder are treated in the same manner as the equations in section 4.1.2 *Test Cylinder Pressures*, thereby resulting in equation 4.10 and 4.11.

$$\dot{P}_{L_p} = \frac{\left(Q_{L_p} + A_{L_p}\dot{x}\right)\beta}{V_{L_p0} + A_{L_p}\left(x_{Lstroke} - x - x_0\right)} \tag{4.8}$$

$$\dot{P}_{L_r} = \frac{\left(Q_{L_r} - A_{L_r}\dot{x}\right)\beta}{V_{L_r0} + A_{L_r}\left(x + x_0\right)} \tag{4.9}$$

$$P_{L_p}(s) = \frac{\left(Q_{L_p} + A_{L_p}X(s)s\right)\beta}{\overline{V}_{L_p}s} \tag{4.10}$$

$$P_{L_r}(s) = \frac{\left(Q_{L_r} - A_{L_r}X(s)s\right)\beta}{\overline{V}_{L_r}s} \tag{4.11}$$

4.1.4 Test Valve Flow

The flows into the test cylinders rod and piston side are to be formulated by linear equations of the form seen in equation 4.12 and 4.13. The constants used in the linear equations are found through Taylor series linearization.

$$Q_{T_p}(s) = K_{u_{T_p}}u_T(s) + K_{P_{T_p}}P_{T_p}(s) \tag{4.12}$$

$$Q_{T_r}(s) = K_{u_{T_r}}u_T(s) + K_{P_{T_r}}P_{T_r}(s) \tag{4.13}$$

The constants used in the two flow equations are given in equation 4.14 to equation 4.17.

$$K_{u_{T_p}} = \left.\frac{\partial Q_{T_p}}{\partial u_T}\right|_{u_T=\overline{u}_T, P_{T_p}=\overline{P}_{T_p}} = \begin{cases} K_T\sqrt{\frac{2}{\rho}\left(P_s - \overline{P}_{T_p}\right)} & , \quad u \geq 0 \\ K_T\sqrt{\frac{2}{\rho}\left(\overline{P}_{T_p} - P_t\right)} & , \quad u < 0 \end{cases} \tag{4.14}$$

$$K_{u_{T_r}} = \left.\frac{\partial Q_{T_r}}{\partial u_T}\right|_{u_T=\overline{u}_T, P_{T_r}=\overline{P}_{T_r}} = \begin{cases} K_T\sqrt{\frac{2}{\rho}\left(\overline{P}_{T_r} - P_t\right)} & , \quad u \geq 0 \\ K_T\sqrt{\frac{2}{\rho}\left(P_s - \overline{P}_{T_r}\right)} & , \quad u < 0 \end{cases} \tag{4.15}$$

$$K_{P_{T_p}} = \left.\frac{\partial Q_{T_p}}{\partial P_{T_p}}\right|_{u_T=\overline{u}_T, P_{T_p}=\overline{P}_{T_p}} = \begin{cases} -\frac{K_T \overline{u}_T}{\rho\sqrt{\frac{2}{\rho}\left(P_s - \overline{P}_{T_p}\right)}} & , \quad u \geq 0 \\ \frac{K_T \overline{u}_T}{\rho\sqrt{\frac{2}{\rho}\left(\overline{P}_{T_p} - P_t\right)}} & , \quad u < 0 \end{cases} \tag{4.16}$$

$$K_{P_{T_r}} = \left.\frac{\partial Q_{T_r}}{\partial P_{T_r}}\right|_{u_T=\overline{u}_T, P_{T_r}=\overline{P}_{T_r}} = \begin{cases} \frac{K_T \overline{u}_T}{\rho\sqrt{\frac{2}{\rho}\left(\overline{P}_{T_r} - P_t\right)}} & , \quad u \geq 0 \\ -\frac{K_T \overline{u}_T}{\rho\sqrt{\frac{2}{\rho}\left(P_s - \overline{P}_{T_r}\right)}} & , \quad u < 0 \end{cases} \tag{4.17}$$

4.1.5 Load Valve 1 Flow

Unlike the flow entering the test cylinder, the load cylinder piston and rod side have separate controlled valves. A flow equation only including linear parts for the flow entering the rod side of the load cylinder is formulated in equation 4.18.

$$Q_{L_r}(s) = K_{u_{L_r}} u_{L_1}(s) + K_{P_{L_r}} P_{L_r}(s) \tag{4.18}$$

The constants are given in equation 4.19 and 4.20.

$$K_{u_{L_r}} = \left.\frac{\partial Q_{L_r}}{\partial u_{L_1}}\right|_{u_{L_1}=\overline{u}_{L_1}, P_{L_r}=\overline{P}_{L_r}} = \begin{cases} K_T\sqrt{\frac{2}{\rho}\left(P_s - \overline{P}_{L_r}\right)} & , \quad u \geq 0 \\ K_T\sqrt{\frac{2}{\rho}\left(\overline{P}_{L_r} - P_t\right)} & , \quad u < 0 \end{cases} \tag{4.19}$$

$$K_{P_{L_r}} = \left.\frac{\partial Q_{L_r}}{\partial P_{L_r}}\right|_{u_{L_2}=\overline{u}_{L_1}, P_{L_r}=\overline{P}_{L_r}} = \begin{cases} -\frac{K_T \overline{u}_{L_1}}{\rho\sqrt{\frac{2}{\rho}\left(P_s - \overline{P}_{L_r}\right)}} & , \quad u \geq 0 \\ \frac{K_T \overline{u}_{L_1}}{\rho\sqrt{\frac{2}{\rho}\left(\overline{P}_{L_r} - P_t\right)}} & , \quad u < 0 \end{cases} \tag{4.20}$$

4.1.6 Load Valve 2 Flow

As with load valve 1, a linear equation is derived in equation 4.21.

$$Q_{L_p}(s) = K_{u_{L_p}} u_{L_2}(s) + K_{P_{L_p}} P_{L_p}(s) \tag{4.21}$$

The constants are given as in equation 4.22 and equation 4.23.

$$K_{u_{L_p}} = \left.\frac{\partial Q_{L_p}}{\partial u_{L_2}}\right|_{u_{L_2}=\overline{u}_{L_2}, P_{L_p}=\overline{P}_{L_p}} = \begin{cases} K_T\sqrt{\frac{2}{\rho}\left(P_s - \overline{P}_{L_p}\right)} & , \quad u \geq 0 \\ K_T\sqrt{\frac{2}{\rho}\left(\overline{P}_{L_p} - P_t\right)} & , \quad u < 0 \end{cases} \tag{4.22}$$

$$K_{P_{L_p}} = \left.\frac{\partial Q_{L_p}}{\partial P_{L_p}}\right|_{u_{L_2}=\overline{u}_{L_2}, P_{L_p}=\overline{P}_{L_p}} = \begin{cases} -\frac{K_T \overline{u}_{L_2}}{\rho\sqrt{\frac{2}{\rho}\left(P_s - \overline{P}_{L_p}\right)}} & , \quad u \geq 0 \\ \frac{K_T \overline{u}_{L_2}}{\rho\sqrt{\frac{2}{\rho}\left(\overline{P}_{L_p} - P_t\right)}} & , \quad u < 0 \end{cases} \tag{4.23}$$

4.2 Block Diagram

From section 4.1 *Linear Model* block diagrams can be developed and used to derive the transfer functions used in section 4.4 *Controller Designs*. To make the system block diagram more manageable, it is chosen to divide it up in three parts.

As seen in figure 4.1 the load cylinder has two inputs due to the two separate controlled valves. The output of the diagram is the resultant force produced by the pressures.

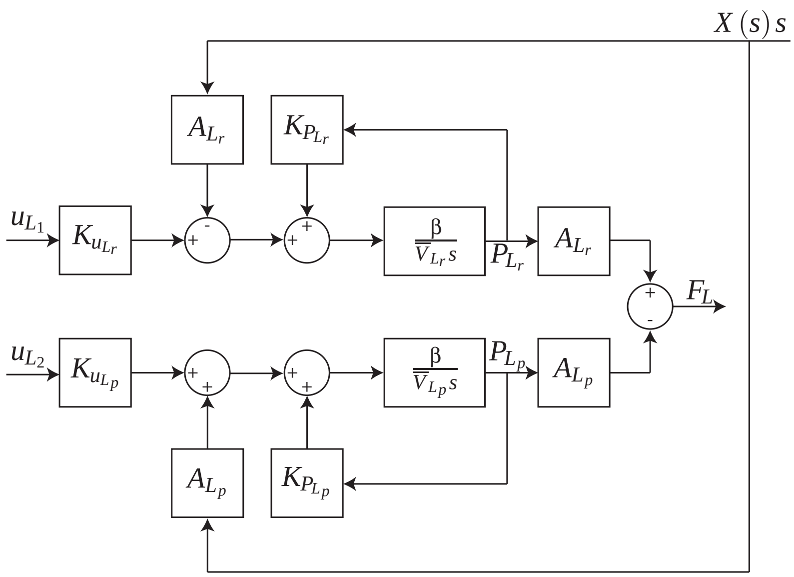

Figure 4.1: Block diagram of the load cylinder.

The block diagram of the test cylinder, figure 4.2, has u_T as an input and F_T as a output. The cylinder velocity is fed back from the linearized equation of motion, derived in equation 4.3 on page 31, not shown in this diagram.

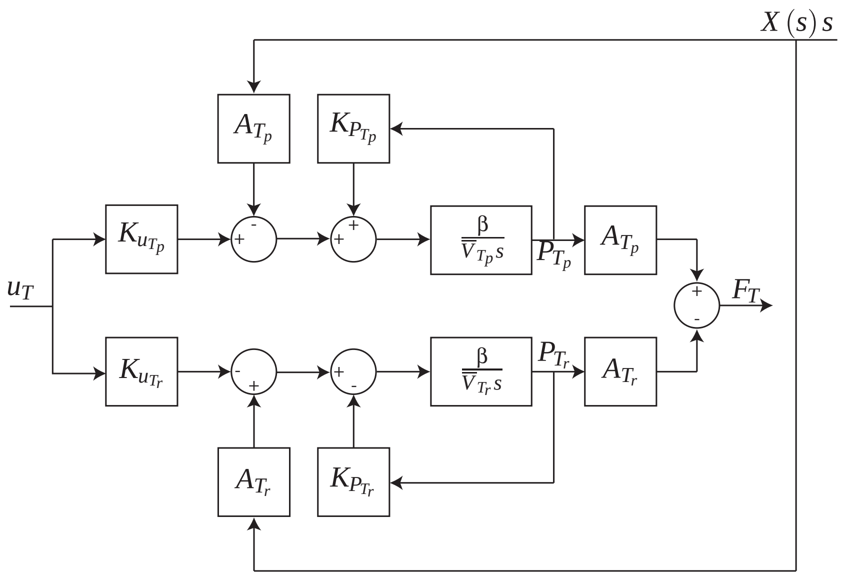

Figure 4.2: Block diagram of the test cylinder.

The block diagram of the linearized equation of motion is presented in figure 4.3. As seen, this block outputs the system velocity, based on the two inputs; the resulting forces from each cylinder. The output of this diagram is fed back to the continuity equations implemented in the cylinder block diagrams.

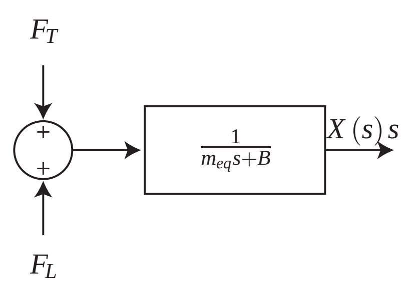

Figure 4.3: Block diagram combining the forces from the two cylinders.

The transfer function presented in the block diagram in figure 4.3 will be referred to as G_{EM}.

The three block diagrams are reduced and their transfer functions used in the controller development for the given controller strategy.

4.3 Control Strategies

In section 4.3.1 *Force Control of the Load System* the block diagrams from section 4.2 *Block Diagram* are reduced to derive transfer functions for the load cylinder force control and the velocity control of the test cylinder in section 4.3.2 *Velocity Control of the Test System.* The transfer functions are used in section 4.4 *Controller Designs.*

4.3.1 Force Control of the Load System

The control strategy used for the load system should be able to maintain a constant load under operation. Having two valves enables a more specific load control. A single valve would also be able to control the resultant force of the load cylinder, but by using two valves the produced load force can be specified as well as the pressure regimes of the chambers. The load force F_{Lref} is the resulting force produced by the chamber pressures in the load cylinder. The pressure reference in the piston side of the load cylinder P_{L_pref} is to be determined from the pressure reference in the rod side of the load cylinder P_{L_rref} as seen in equation 4.24.

$$P_{L_pref} = \frac{A_{L_r}}{A_{L_p}} P_{L_rref} - \frac{1}{A_{L_p}} F_{Lref} \tag{4.24}$$

In figure 4.4 the force control is implemented in the block diagram for the load system through pressure feedback for each cylinder chamber. The flows, resulting from the velocity of the system, into the load cylinder chambers are treated as disturbances and are canceled through feedforward compensation using the feedforward gains C_{ffL_r}, C_{ffL_p} and the measured velocity $\dot{x}_{measured}$. The red boxes indicate the final pressure control systems.

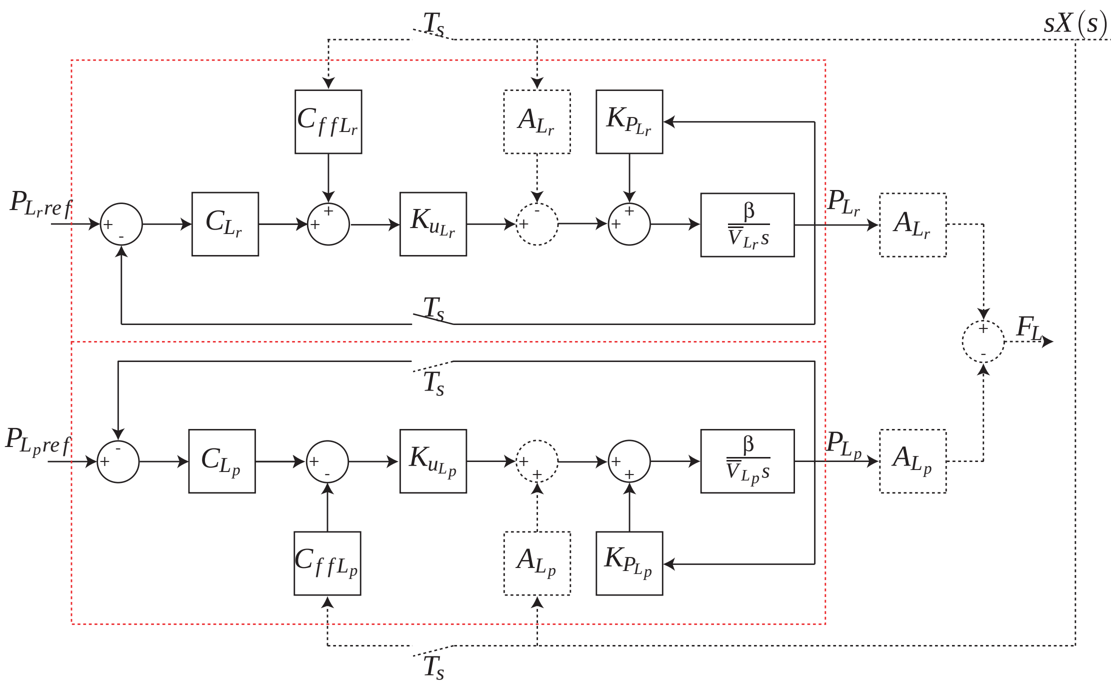

Figure 4.4: Blockdiagram of the force control used on the load cylinder.

By disregarding the disturbances, feedforward gains and the controllers, the open loop transfer functions for the two pressure systems are expressed as seen in equation 4.25 and 4.26, respectively.

$$G_{L_r ol} = \frac{\frac{K_{u_{L_r}}\beta}{\overline{V}_{L_r}}}{s - \frac{\beta K_{P_{L_r}}}{\overline{V}_{L_r}}} \tag{4.25}$$

$$G_{L_p ol} = \frac{\frac{K_{u_{L_p}}\beta}{\overline{V}_{L_p}}}{s - \frac{\beta K_{P_{L_p}}}{\overline{V}_{L_p}}} \tag{4.26}$$

The purpose of the two feedforward flow gains C_{ffL_r} and C_{ffL_p} are to cancel the flow disturbances from the test system and are seen in equation 4.27 and 4.28.

$$C_{ffL_r} = \frac{A_{L_r}}{K_{u_{L_r}}} \tag{4.27}$$

$$C_{ffL_p} = \frac{A_{L_p}}{K_{u_{L_p}}} \tag{4.28}$$

Note that due to the friction in the load cylinder, the applied force deviates from F_{Lref} and therefore the applied force is difficult to predict without an adequate friction model for the load cylinder.

4.3.2 Velocity Control of the Test System

To determine a suitable control strategy for the test cylinder it is essential that it fulfills the demands for the needed test runs. The constants used to express the Stribeck curve can be estimated through constant velocity data. Combining the data samples from different constant velocity datasets will derive a Stribeck curve, and due to the constant velocity the initial forces are then equal to zero. The control strategy will therefore have the aim to hold a constant velocity[Lambert et al., 2002].

Combining and reducing the block diagrams, seen in figure 4.2 and figure 4.3 on page 35, and disregarding the force disturbance from the load cylinder, the transfer function describing the velocity to a voltage input can be expressed as seen in equation 4.29.

$$G_{Tol} = \frac{n_{TC}\left(sn_{T1} + n_{T0}\right)}{s^3 + s^2 d_{T2} + sd_{T1} + d_{T0}} \tag{4.29}$$

where

$$n_{TC} = \frac{\beta}{m_{eq}\overline{V}_{T_p}\overline{V}_{T_r}} \tag{4.30}$$

$$n_{T0} = \beta K_{uTp}K_{PTr}A_{Tp} - \beta K_{uTr}K_{PTp}A_{Tr} \tag{4.31}$$

$$n_{T1} = K_{uTr}A_{Tr}\overline{V}_{T_p} + K_{uTp}A_{Tp}\overline{V}_{T_r} \tag{4.32}$$

$$d_{T0} = \beta^2 \frac{A_{Tp}^2 K_{PTr} - K_{PTr}K_{PTp}B - A_{Tr}^2 K_{PTp}}{m_{eq}\overline{V}_{T_p}\overline{V}_{T_r}} \tag{4.33}$$

$$d_{T1} = \beta \frac{A_{Tp}^2\overline{V}_{T_r} - K_{PTp}B\overline{V}_{T_r} - \beta K_{PTp}m_{eq}K_{PTr} + A_{Tr}^2\overline{V}_{T_p} + \overline{V}_{T_p}BK_{PTr}}{m_{eq}\overline{V}_{T_p}\overline{V}_{T_r}} \tag{4.34}$$

$$d_{T2} = \frac{\overline{V}_{T_p}m_{eq}\beta K_{PTr} - \beta K_{PTp}\overline{V}_{T_r}m_{eq} + B\overline{V}_{T_p}\overline{V}_{T_r}}{m_{eq}\overline{V}_{T_p}\overline{V}_{T_r}} \tag{4.35}$$

By inserting parameters for the system, the controllers can be designed for the pressure and velocity control strategies.

4.4 Controller Designs

The demands for the controllers are to reduce the disturbance effect and to improve the response, but also to remove steady state error at step inputs. The parameters in the controllers presented in this section are designed from values of the specific systems. These values include direct measurable values eg. the supply pressure and simulation-based values eg. evaluation points. The controllers presented in this section are derived from the system with a constant supply pressure at $P_s = 150\ [bar]$.

Different plots are used to quickly reveal different aspects of the designed control system. The root locus plot is used to give an idea of the system time constants and damping while the determination of the relative stability is easily derived from bode plots. The systems are controlled through a digital signal processor the analogue controllers are digitalized through backward Euler using a sampling time $T_s = 1/10{,}000$ and documented in *appendix D Filters and Difference Equations*. The relatively low sampling time, in theory, would ensure a stable analogue system to remain stable when converted to the z-domain through use of backward Euler. Moreover, the poles and zeroes for the digital controlled systems are checked to lie within the unit circle which indicates stability. The last plot considered is the unit step response of the closed loop control systems. The unit step response is used to analyze different system time aspects, stability, and steady state error. In the following only the root locus and the unit step response plot for the different systems are presented. All four types of plots are found in *appendix E Control System Plots.* No free integrators are present in the three open loops of the systems why they are all categorized as type zero systems. The controllers used for all three control systems are simple PI-controllers as the integrator in this type of controller will remove the steady state error when applying a step input. The general form of this type of controller can be expressed as seen in equation 4.36

$$C_{PI} \quad = \quad K_P + \frac{K_I}{s} = \frac{K_P s + K_I}{s} = K_c \frac{\tau_c s + 1}{s} \tag{4.36}$$

The controlled *open loop* transfer functions for the three control systems are denoted G_{CTol}, G_{CL_rol} and G_{CL_pol}. Likewise are the controlled *closed loop* transfer functions denoted by eg. G_{CTcl} and a z-transformed transfer function is denoted by e.g. $G_T(z)$.

To further cancel out the disturbance from the interactions between the systems, the controllers must be designed to result in adequately dissimilar bandwidths. When considering the faster system the disturbance will appear as constant.

The final values for the parameters in the three PI-controllers are seen in table 4.1.

	τ_c	K_c
C_T	0.06	$8.00 \cdot 10^2$
C_{L_r}	0.33	$1.25 \cdot 10^{-4}$
C_{L_p}	0.25	$6.50 \cdot 10^{-5}$

Table 4.1: Values of the controller parameters.

The control system bandwidths are found to be the values seen in table 4.2.

	Bandwidth	
G_{CTcl}	378	$[rad/sec]$
G_{CL_rcl}	151	$[rad/sec]$
G_{CL_pcl}	87	$[rad/sec]$

Table 4.2: Bandwidths of the controlled closed loop system.

These values are considered adequately dissimilar as the lowest ratio between them is 1.77.

The constant values in the two feedforward controllers in the load system are presented in table 4.3.

	Gain
C_{ffL_r}	5.7205
C_{ffL_p}	34.0682

Table 4.3: Feedforward gains.

Figure 4.5 displays the root locus plot of the open and closed control loop transfer function for the rod-side in the load system by blue and the closed loop by red. Poles are noted by o or o and roots by x or x. The root located at $\omega = 0$ is from the free integrator introduced by the controller. The root located at $\omega = -1.76$ is the constant negative product of $\beta K_{P_{L_r}} / \overline{V}_{L_r}$ from the original uncontrolled system. As seen in figure 4.5 a pole is located at $\omega = -3.03$ which is the inverted negative value of the time constant τ_c in the adhering controller. Due to the small gain in the controller, the roots in the closed loop are located close to the closed loop poles. A root not displayed is located at $\omega = -110.76$ which is a product of the chosen controller gain K_{cLr} and closed loop parameters. The constants in the controllers are chosen to result in *critical* or *over-damped* systems. An overshoot of approximately 1% is seen in the unit step response for G_{CL_rcl} in figure 4.6.

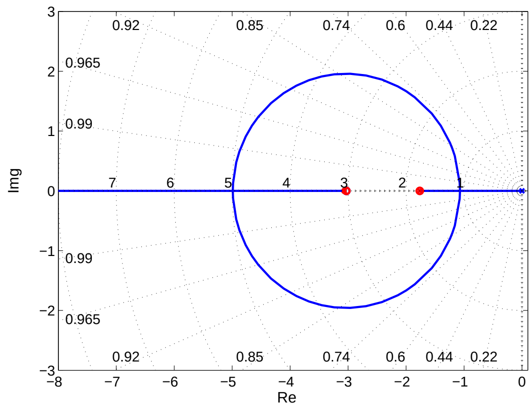

Figure 4.5: Root locus of G_{CL_rol} (blue) and G_{CL_rcl} (red).

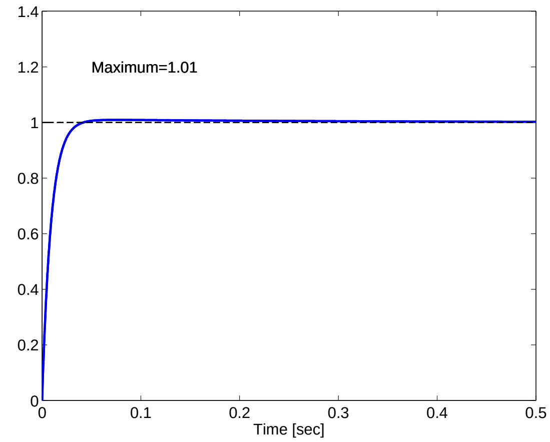

Figure 4.6: Unity step response of G_{CL_rcl}.

Figure 4.7 displays the root locus plot of the open and closed control loop transfer function for the piston-side in the load system. The root located at $\omega = -7.32$ is the constant negative product of $\beta K_{P_{L_p}}/\overline{V}_{L_p}$ from the original uncontrolled system. As can be seen in figure 4.8 the control system has no overshoot.

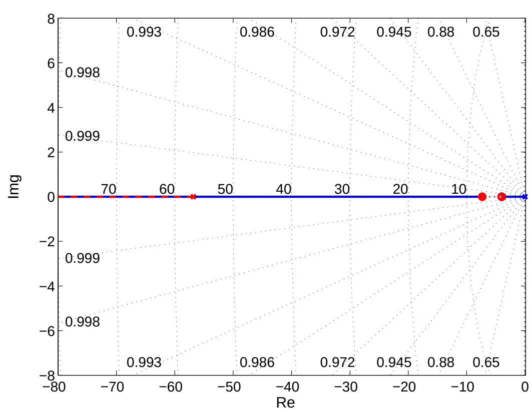

Figure 4.7: Root locus of G_{CL_pol}.

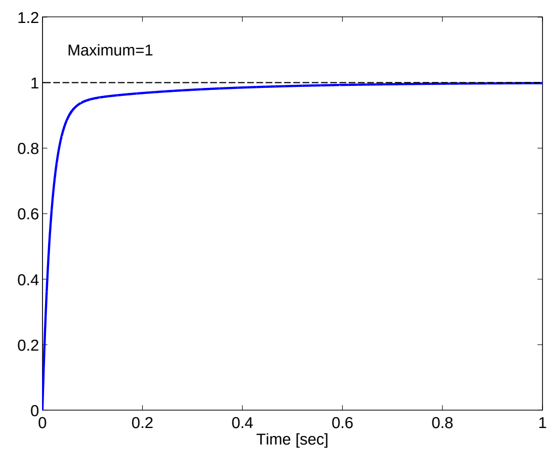

Figure 4.8: Unity step response of G_{CL_pcl}.

Due to the high order of G_{CT} several poles and zeros are placed in the root locus plot for G_{CTol} as seen in figure 4.9, but all of them are located in the left half-plane side which is an indication of stability. It is seen in figure 4.10, which illustrates the unit step response of G_{CTcl}, that the system has no overshoot. Furthermore, the settling time is read to $\tau_{2\%} < 0.4$ $[sec]$.

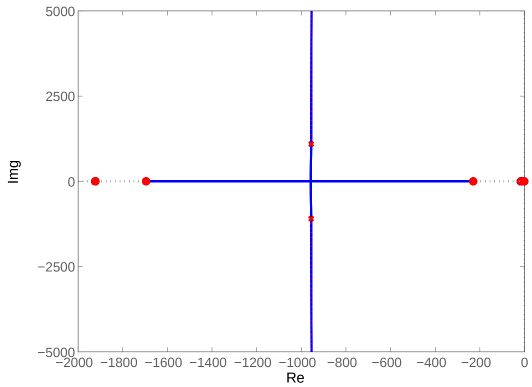

Figure 4.9: Root locus of G_{CTol}.

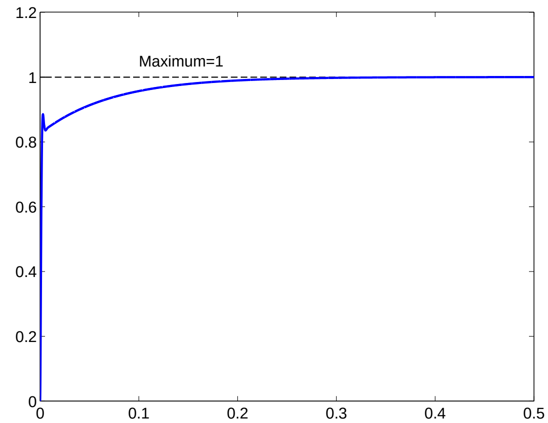

Figure 4.10: Unity step response of G_{CTcl}.

4.5 Evaluation of the Implemented Controllers

In this section the implementation of the z-transformed controllers in the nonlinear model are presented. Furthermore, some of the simulated responses to inputs are compared to measured data from the actual test bench.

Figure 4.11 schematically illustrates the control of the nonlinear model. The *Test Bench* block is the representation of the nonlinear Simulink model presented in figure 2.5 on page 15. The velocity feed-forward ff can be switched on or off to be able to evaluate the impact it has on the system dynamics. To simulate the delay from the digital sampling time T_s the zero-order-hold blocks are implemented and depicted with ZOH.

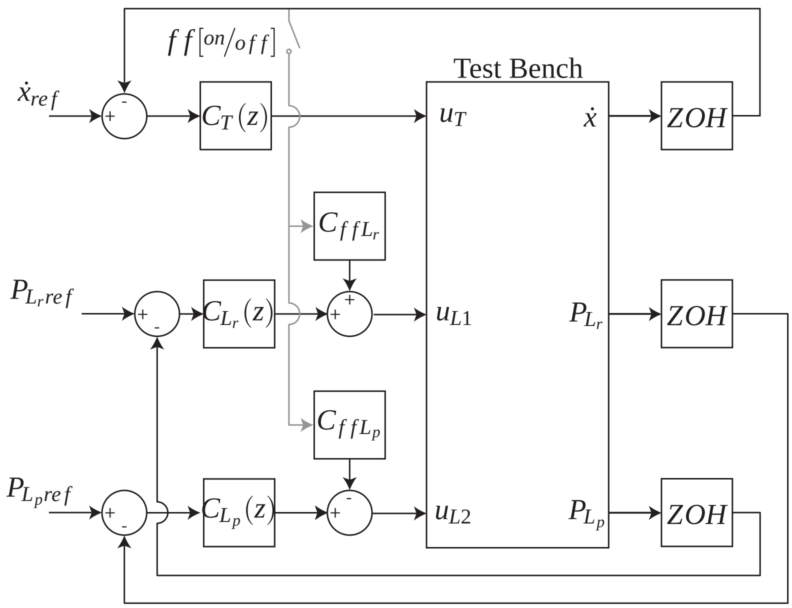

Figure 4.11: Schematic diagram of the control of the nonlinear model.

The digital controllers are implemented in the Simulink model. Before they can be used in in the DSP program presented in section 4.6 *DSP Program* they are to be converted into difference equations, as documented in *appendix D Filters and Difference Equations*.

4.5.1 Evaluation of Constant Reference Control

Figure 4.12, 4.13 and 4.14 depicts simulated and measured data at different constant velocity references, but at the same constant pressure references. The resultant force from the pressures in the load cylinder is set to 10 $[kN]$, which results in $P_{L_p ref} = 88.7$ $[bar]$ at $P_{L_r ref} = 15.0$ $[bar]$. The constant references are attained until the piston is stopped by the end-stop, which can be observed in figure 4.12 to 4.14.

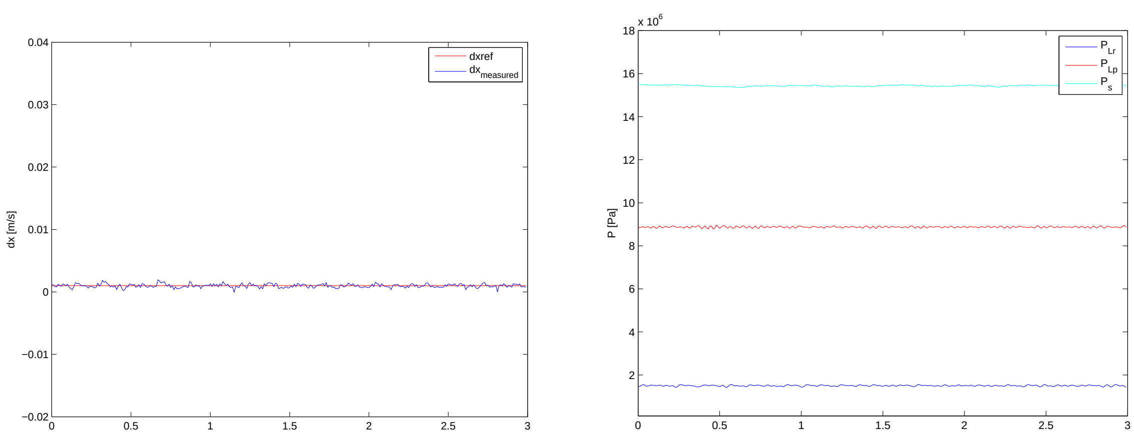

Figure 4.12: Velocity and pressure data at $\dot{x}_{ref} = 1.0$ $[mm/s]$, $P_{L_r ref} = 15$ $[bar]$ and $P_{L_p ref} = 88.7$ $[bar]$.

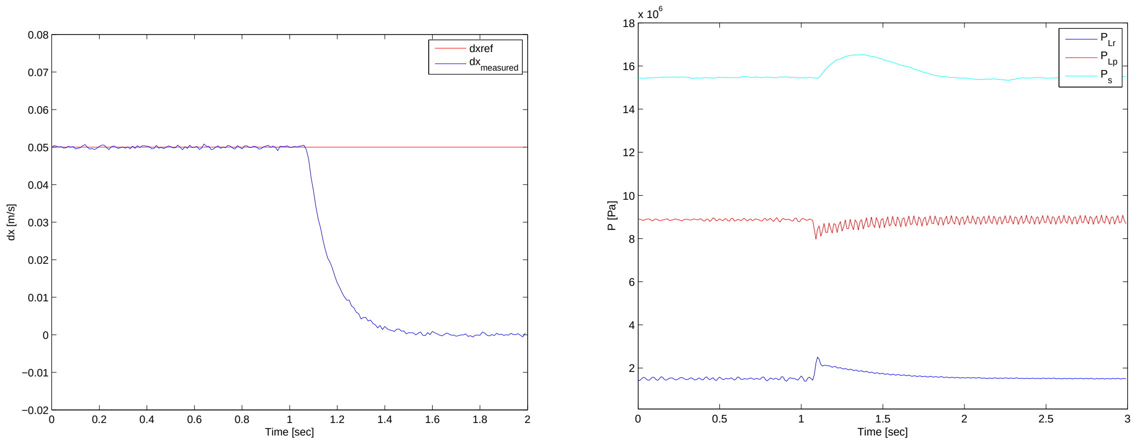

Figure 4.13: Velocity and pressure data at $\dot{x}_{ref} = 50.0\ [mm/s], P_{L_r ref} = 15\ [bar]$ and $P_{L_p ref} = 88.7\ [bar]$.

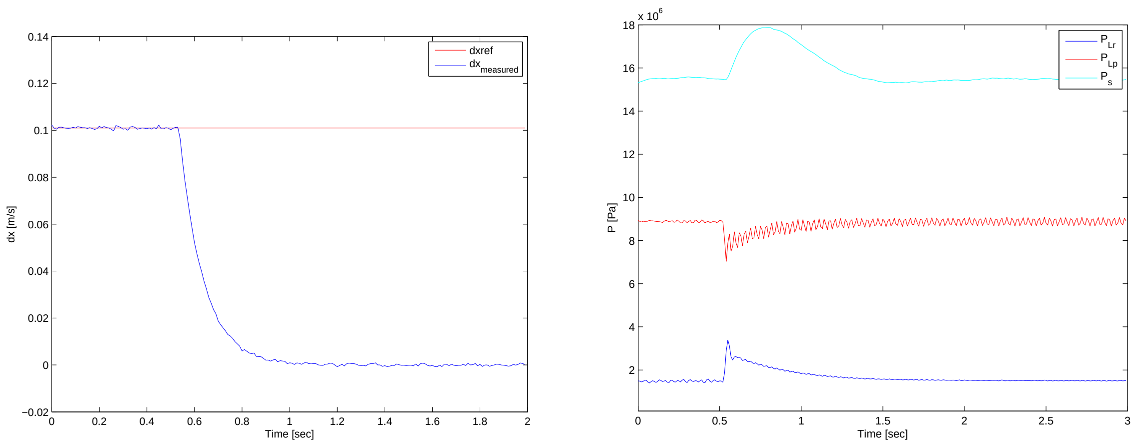

Figure 4.14: Velocity and pressure data at $\dot{x}_{ref} = 101.0\ [mm/s], P_{L_r ref} = 15\ [bar]$ and $P_{L_p ref} = 88.7\ [bar]$.

An important observation can be derived from data collected from the supply pressure transducer. As seen in figure 4.15 the supply pressure, P_s, is not constant during operation as was initially assumed in the linear and nonlinear model.

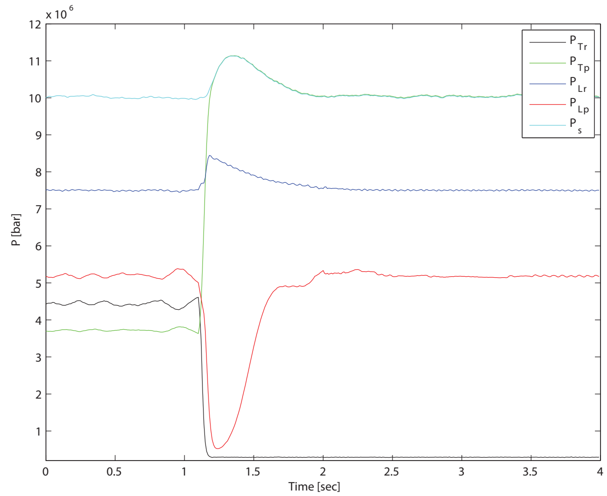

Figure 4.15: Measured data for pressures at $\dot{x}_{ref} = 52.2$ $[mm/s]$, $P_{L_r ref} = 75$ $[bar]$, $P_{L_p ref} = 53.7$ $[bar]$ and $F_{Lref} = 1$ $[kN]$.

The reason for the supply pressure fails to remain constant is assumed to be due to the limited power of the pump as it is failing to mechanically compensate fast enough to counter the valves with faster response time. This assumption is supported when observing the pressures for the test cylinder chambers. As the sledge reaches the end-stop and is abruptly brought to a hold, causing the control for the velocity control system to attempt to maintain $\dot{x}_{ref}$ by displacing the plunger of the test valve, finally results in a full opening between the piston-side and the supply line. The rod-side will then be fully opened to reservoir line. In figure 4.16 it is depicted that the system is struggling to attain the relative high referenced velocity due to oscillations in the supply pressure. Therefore all measured data at high velocities ($\dot{x}_{ref} > 150$ $[mm/s]$) must be checked to be close to the referenced velocity with an deviation of maximum ± 2 $[mm/s]$, or otherwise disregarded in further data analysis.

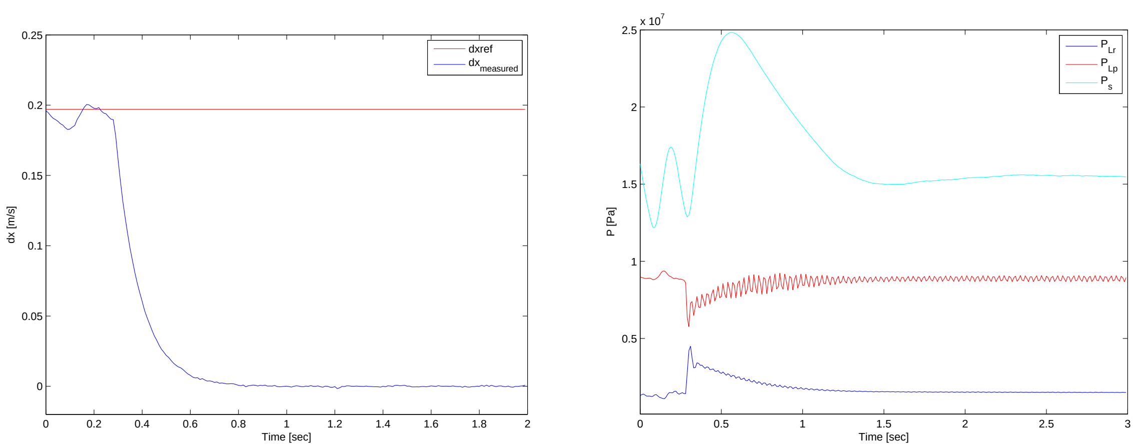

Figure 4.16: Velocity and pressure data at $\dot{x}_{ref} = 197.0$ $[mm/s]$, $P_{L_r ref} = 15$ $[bar]$ and $P_{L_p ref} = 88.7$ $[bar]$.

4.5.2 Evaluation of Feedforward Compensation

Figure 4.17 depicts the velocity data to step inputs and figure 4.19 depicts data from the two constant controlled pressures obtained under the velocity step control. Considering figure 4.19 it can be observed that the velocity feedforward to the pressure control systems has a positive effect on the model as it decreases the errors induced when applying the velocity steps. Another aspect, which can be derived from these data, is the steady state errors are all zero to the step inputs as expected.

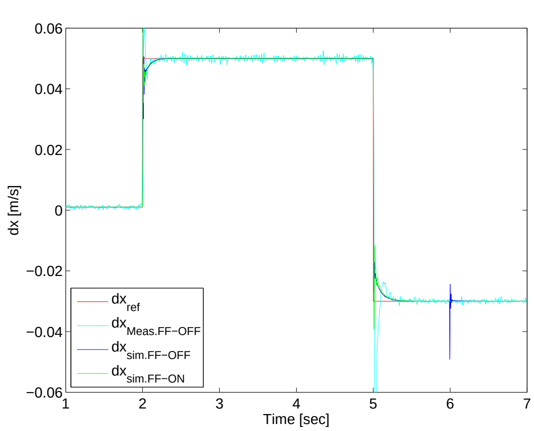

Figure 4.17: Control velocity at step in $\dot{x}_{ref}$ and constant pressure references.

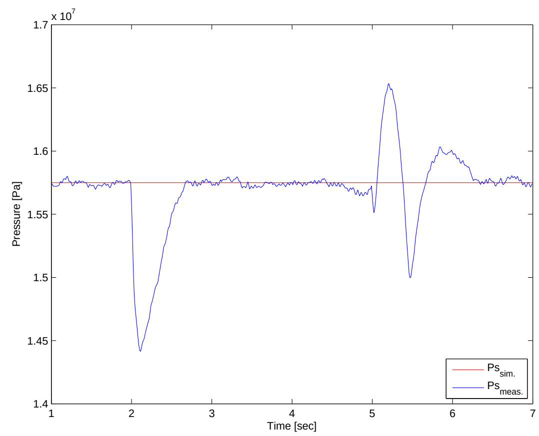

Figure 4.18: Supply pressure at step in $\dot{x}_{ref}$ and constant pressure references.

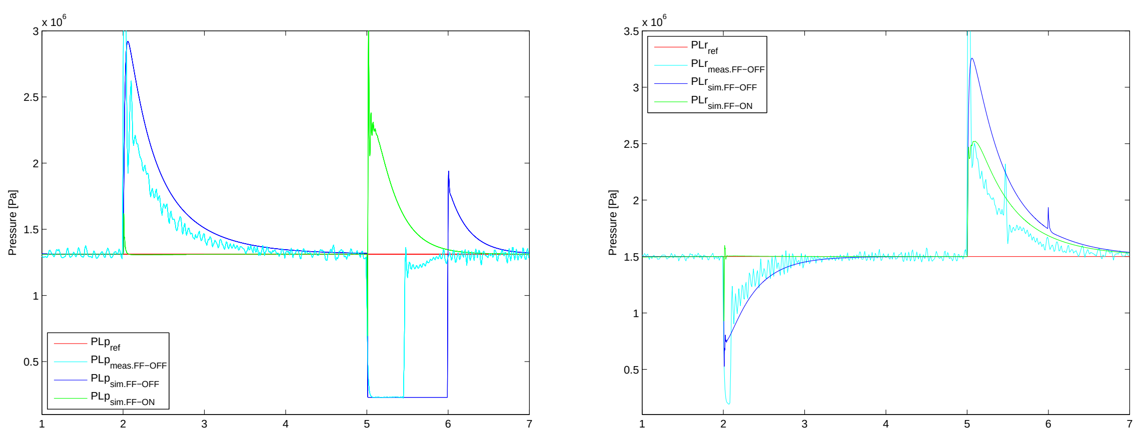

Figure 4.19: Control pressures at step in $\dot{x}_{ref}$ and constant pressure references.

The implementation of the feedforward compensation did not yield satisfactory results when applied in the physical setup, why feedforward compensation is switched off during friction tests. The reason is expected to be due to the implied errors when linearizing expressions to specific work points and also inconsistent behavior of some system parameters, *e.g. the supply pressure*, but this is not investigated further as sudden velocity step inputs are not used in the friction tests, rendering the velocity feedforward compensation redundant.

4.5.3 Evaluation of Velocity Ramping

Figure 4.20 depicts velocity data as $\dot{x}_{ref}$ is ramped up and down between ± 50 $[mm/s]$ using a slope of $\ddot{x}_{ref} = \pm 100$ $[mm/s^2]$.

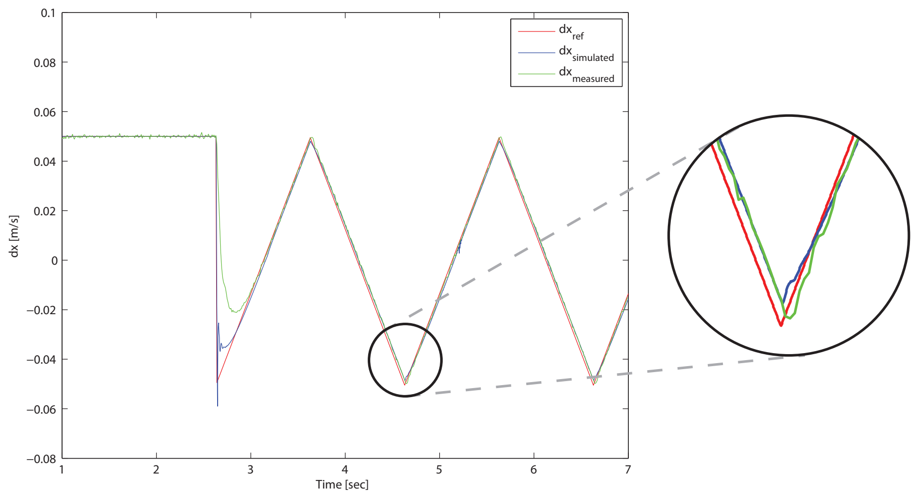

Figure 4.20: Simulated and measured data for the ramped velocity, $\ddot{x}_{ref} = \pm 100$ $[mm/s^2]$.

An expected steady state error occurs as the open loop controlled system is a type 1 system, and the applied velocity reference is ramped. In theory the steady state error for the velocity system at ramp inputs can be calculated by using equation 4.37 [Phillips and Harbor, 2000].

$$e_{ss\ddot{x}_{ref}} = \frac{\ddot{x}_{ref}}{K_v} \tag{4.37}$$

$$K_v = \lim_{s \to 0} G_{CTol} s \tag{4.38}$$

Using the estimated system parameters, the transfer functions and setting $\ddot{x}_{ref} = 100$ $[mm/s^2]$ the theoretical steady state error at the given ramp input is calculated to $e_{ssramp} = 1.67$ $[mm/s]$. The steady state error obtained from the Simulink model was in the interval of $e_{ssramp} = [1.5;\ 1.7]$ $[mm/s]$ and the steady state error obtained from the test bench was approximately the same.

From this section it can be concluded that a fairly good control is attained. Due to poor pump performance, data collected for relative high velocities and load scenarios must be examined to verify the dynamics of the pump has minimal influence or accounted for.

4.6 DSP Program

When test runs are conducted on the test bench a *Texas Instruments TMS320f28335* is used for controlling as well as data recording purposes. The program loaded onto the DSP is written in and compiled from *Code Composer Studio v4*. The desired controlling frequency is 10 $[kHz]$, and due to the limited memory of the DSP a lower sampling frequency 100 $[Hz]$ has been chosen for model verification and friction modeling. In figure 4.21 a flow chart is illustrating the program executed on the DSP. The complete program is found on the enclosed DVD.

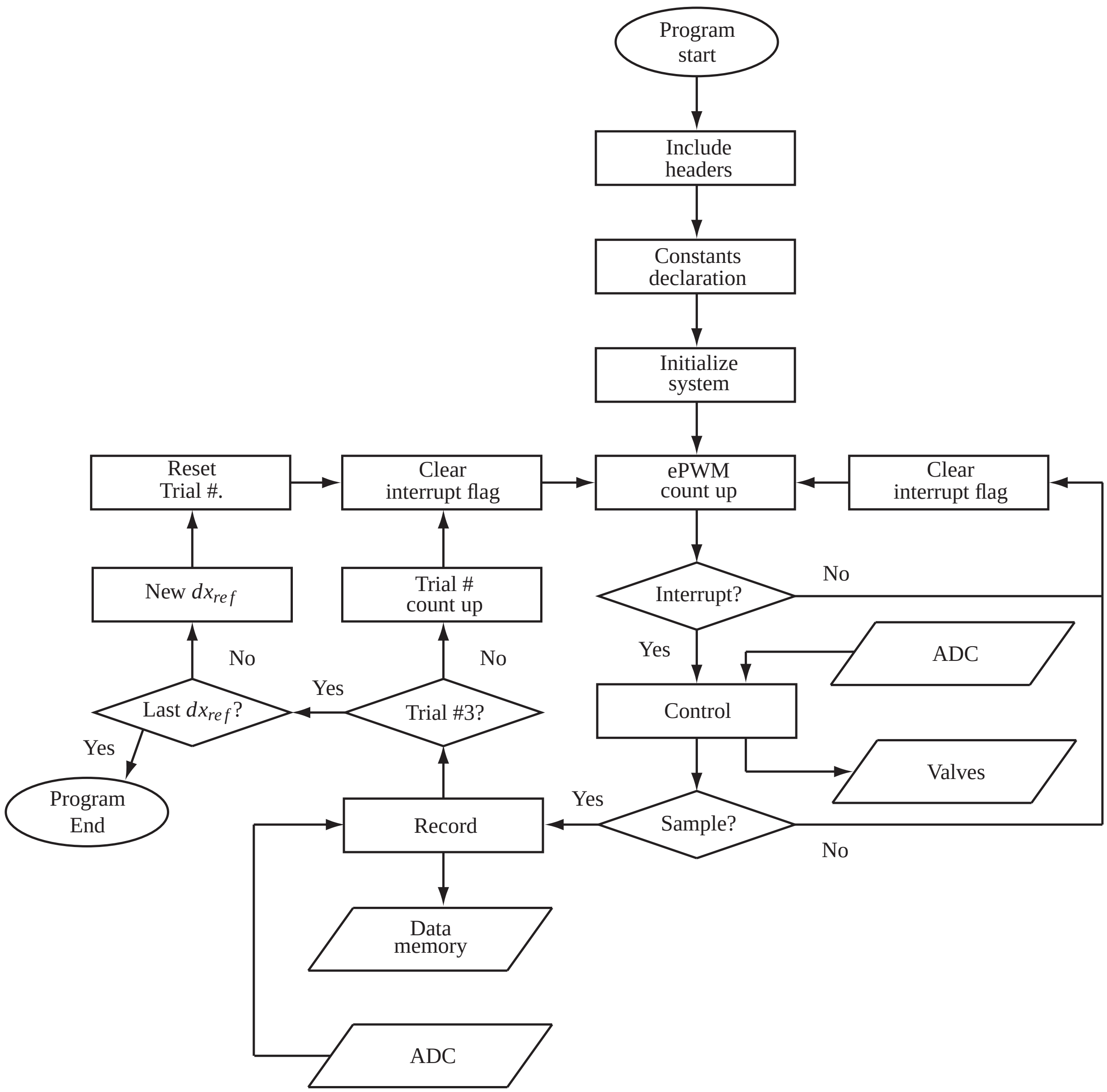

Figure 4.21: Flowchart illustrating the structure of the DSP program.

The *Initialize system* box from figure 4.21 is shown more detailed in figure 4.22.

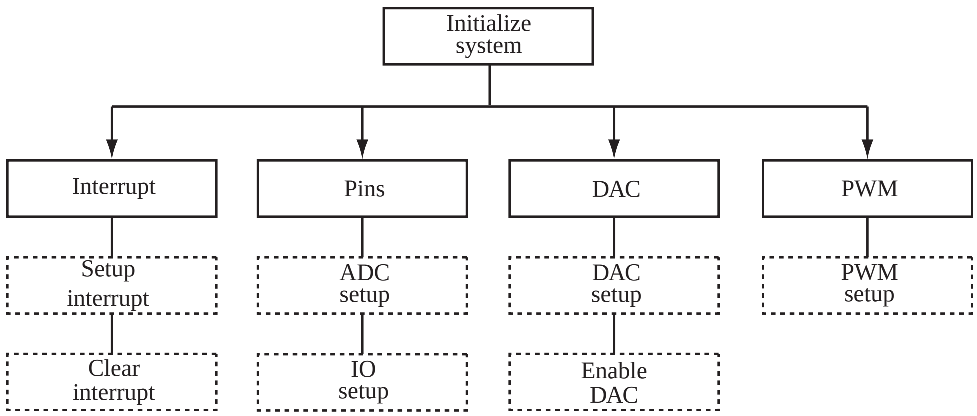

Figure 4.22: Chart showing the most important parts of the *system initialization*.

The ePWM is determining when to trigger the control algorithm and the data sampling. As the sampling frequency is set to a lower value than the control frequency a sampling frequency divider is introduced in the program. If the sampling frequency divider is set to 10, a data sampling will only occur every tenth control cycle. This could also have been triggered by a second ePWM.

The control section is consisting of the difference equations of *appendix D Filters and Difference Equations* and the results are outputted through the multichannel buffered serial port (McBSP) of the DSP to an external digital to analog converter(DAC) connected to the valves.

The data samples will be collected by the internal analog to digital converter (ADC) and stored onto the ram memory.

The test bench setup is expected to be an easy way to test a specific cylinders performance, and therefore the test bench should perform as many tasks automatically as possible. The program executed on the DSP is constructed so it only needs to be activated, and thereafter it is to record the necessary data automatically and shut down the system afterwards. Deriving data for the Stribeck and the efficiency curves demands for data sets with constant load and velocity. The program runs three trials with the same load and velocity before a new dx_{ref} is set. This is done so that a mean value of the three trials can be obtained. To develop Stribeck curves, different runs at several different $\dot{x}_{ef}$ are carried out. The recorded data are afterwards analyzed by using a *MATLAB* file that automatically generates Stribeck and efficiency curves. The parameters describing the Stribeck curves are automatically derived.

5 Experimental Approach

To achieve a better understanding of the friction phenomena in hydraulic asymmetrical cylinders, it is of most importance to obtain test data from which friction characteristics can be derived. To ensure the validity of the data a strict consistent experimental approach is necessary. To investigate the presence of friction hysteresis a hysteresis loop is to be derived from a triangular velocity reference as seen in section 5.2 *Triangular Velocity Experiment*. An other phenomenon to be investigated are the Stribeck curve, why the experiments mentioned in section 5.3 *Stribeck curve* are to be conducted.

In all tests conducted in the positive velocity regime, the pressure reference for the load cylinder's rod-side is $P_{Lrref} = 15$ $[bar]$, and $P_{Lrref} = 110$ $[bar]$ when conducting experiments in the negative velocity regime. The pressure reference for the load cylinder's piston-side is set to depend upon P_{Lrref} and F_{Lref}, as explained in section 4.3.1 *Force Control of the Load System*. The supply pressure is set to $P_s = 150$ $[bar]$.

5.1 Assumptions and Simplifications

The friction force is assumed to be affected by several parameters, and not all of these parameters can be controlled in the test bench. Therefore some simplifications are made and the actual conditions are noted:

- **Constant viscosity -** The temperature has a significant influence on the viscosity [Çengel and Turner, 2005].
- **Constant temperature -** Heat is induced to the oil due to throttling in the valves, why precautions are taken in accordance with section 5.2 *Triangular Velocity Experiment*.
- **Surface roughness -** The surface roughness can vary depending on the piston rod position. The tests are therefore to be undertaken in a defined interval of the test cylinder rod position for steady state runs. When ramping the velocity, homogeneous surface roughness is assumed.
- **Directional influence on the friction -** Due to the piston ratio the pressure in a given cylinder chamber is different when operating with a positive velocity reference compared to a negative velocity reference.

5.2 Triangular Velocity Experiment

The test bench has not been operational since assembling, why air is expected to be trapped in the hydraulic components of the test bench. To be able to obtain fair operational values, the air must be filtered from the oil. This is attempted by applying a triangular velocity reference as depicted in figure 5.1. The triangularly velocity reference is adjusted in such a way, that the cylinders are shifting between the maximum and minimum position.

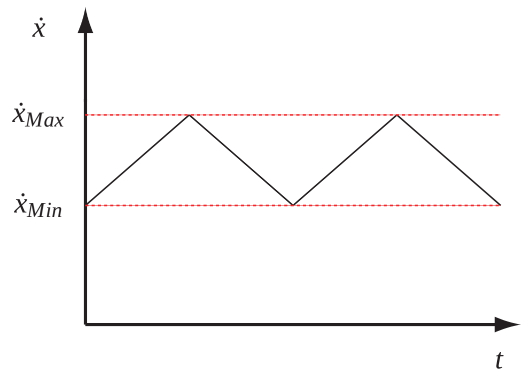

Figure 5.1: Velocity profile when air is eliminated from the system.

The triangular velocity signal is also used to heat up the oil to normal operational conditions and to produce a hysteresis loop. When conducting the hysteresis loop test the load cylinder valves are connected to the reservoir, leading to a minimum value of F_L. This is done so the influence of the load system can be disregarded.

5.3 Stribeck curve

Stribeck curves are desired for different constant load situations to examine the impact of a given load. Two types of test runs are conducted to create the Stribeck curves; steady state velocity test runs and ramping velocity test runs as acceleration is expected to influence the friction in accordance with section 3.1.2 *Friction Lag*. For the steady state velocity experiment, a series of tests with **constant** velocity varying from zero to approximately 0.2 $[m/s]$ are to be performed. The load cylinder is controlled to maintain the same produced force at all velocities. Operating with a constant velocity should, according to the theory in chapter 3 *Friction Modelling*, lead to a steady state friction force. That is of course only in the absence of stick-slip motions. Three force measurements are recorded for every velocity reference. The red crosses in figure 5.2 are representing the average value of the friction force measured in the three runs. It is assumed that 15 averaged values are enough to illustrate the Stribeck curve. In figure 5.2 the velocity interval between the measurements expands from low velocity to high velocity, to obtain a better resolution of the segment thought to be nonlinear.

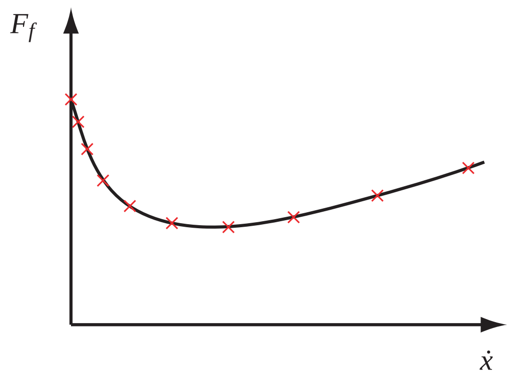

Figure 5.2: Expected average friction values at steady state experiments.

Due to the time-consuming procedure of generating the Stribeck curves from steady state tests, it is chosen to try deriving the curves from a ramping velocity input. The results of the two test types are to be compared.

To evaluate the accelerations influence on friction the velocity is ramped with three different references of acceleration. The friction force of the test cylinder, F_{fT}, is calculated from the equation of motion, equation 2.9, reformulated to equation 5.1 for steady state. Equation 2.12 is used to calculate F_{fT} for ramped velocities.

$$F_{fT} = P_{Tp}A_{Tp} - P_{Tr}A_{Tr} - F_{Applied} \tag{5.1}$$

$F_{Applied}$ is the force derived from measurements of the strain gage and therefore includes the resulting force from the two load chambers and the friction force generated by the load cylinder, F_{fL}. The ramp input is also conducted to obtain information regarding the initial friction behavior.

The data recorded from the Stribeck tests can also be used to determine the friction at different operational situations.

5.4 Control Verification

To verify the control strategy and the Simulink model, velocity steps are conducted. In chapter 4.5 *Evaluation of the Implemented Controllers* the performance was evaluated. When the velocity is stepped, the pressure controllers have to maintain the given references.

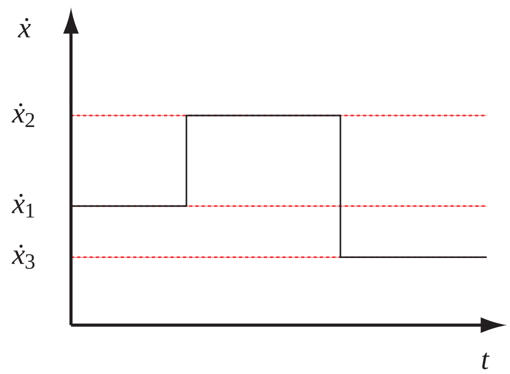

Figure 5.3: Velocity profile for control verification.

This experiment challenging for the controllers and is hence used to examine the influence of the feed-forward compensation described in section 4.5.2 *Evaluation of Feedforward Compensation*.

5.5 Friction Model Verification

It is of essence to verify the performance of one or more of the friction models presented in section 3.2 *Friction Models*, and to do this, a test is conducted that provokes the friction behavior at steady state and unsteady velocity. Implementing the friction function parameters, determined from chapter 6 *Data Analysis*, in a chosen friction model, makes it possible to examine the estimated friction properties of the cylinder.

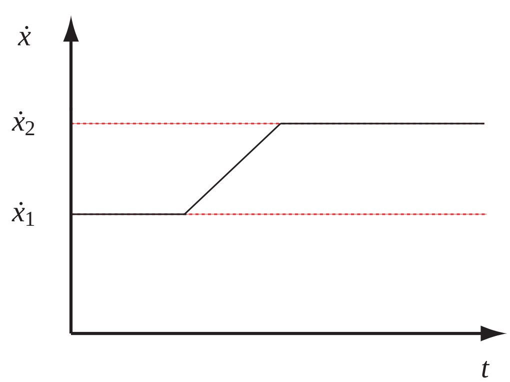

Figure 5.4: Velocity profile for friction model verification.

5.6 Friction Measuring Procedure

This section serves as a guide on how to conduct the friction experiments presented earlier in this chapter. The development of suitable controllers to a given setup is a precondition to this procedure, which is left to the user. Furthermore, it is required to have MATLAB 2010 and Code Composer Studio v4 *(or a newer version)* installed on the computer to be able to use the developed programs. Obviously, the procedure must be performed on the presented test bench with the adhering developed electrical circuits or on a sufficiently similar setup. Suggestions to adjustments for optimization of the control program is stated in section 5.6.1 *Control Program Adjustments.*

The folder: *DataAnalysis*, located on the enclosed DVD, contains the files and folders needed to analyze collected data. Copy this folder to the computer and use the folder as a work directory for future tests.

Automatic execution of the experiments has been aspired during the project period, but only a semi-automatic execution was achieved. The users part in the procedure is limited to specifying the reference pressure in the rod-side chamber and pressure force from the load cylinder, before executing the steady state test program in the *Main Complete.m*-file through the debug mode in code composer. This is to be done at every new load scenario. The *Main_Complete.m* -file is located in the *DSP* - folder.

At the end of a successful steady state test, the program prints out: "*Done with data measurement routine*" in the code composer debug command window, and halts. The user then needs to retrieve the data- (.dat) files from the debug folder and insert them into the *Data Analysis*-folder.

The parameters for the given setup, *e.g. the piston areas of the test cylinder*, must be typed in the *parameter.m*-file located in the *Data Analysis*-folder. Execute *parameter.m*-file and then execute *StribeckCurve.m*-file, which is located in the same folder.

If successfully executed the program opens a series of graphs, including a Stribeck friction-graph with a fitted Tustin function. The derived parameters for the Tustin function are printed in the MATLAB-command window.

In some cases the boundaries used in the *LSQNONLIN-function* might be needed to be reevaluated to obtain better parameter estimates. The boundaries and the friction model to be fitted can be set in *StribeckDataFitt.m*-file. Note the function estimating the friction is the Tustin model, unless otherwise specified. Likewise, the default lower and upper boundary conditions as stated in table 6.1 on page 56.

5.6.1 Control Program Adjustments

As presented in section 4.6 *DSP Program* the program control algorithm executes a series of trials to different velocity references. The program executes three trials at every velocity reference and updates the velocity references with a predetermined function. This function is a 2nd order polynomial as it makes sense to use small step sizes in at low velocity regime, where the friction is assumed to be nonlinear. Greater step sizes are used when the friction is assumed to evolve linear. If the program is to be used in a general manner, it is recommended to change this function. Suggestions on adjustments are stated and commented upon in the following bullets:

- A linear function with small step sizes is simple to implement and is able to cover a broad range of cylinders, but the steady state experiment would be very time consuming.
- If a good estimate on where the friction function transits from nonlinear to linear exists for the

given cylinder, the slope on the updating function can be adjusted to forthcome the expected friction development.

- A correction of the next steady state reference can be developed from the derivative of an on-line calculated friction level. At high absolute values of the friction derivatives, the increase in steady state velocity reference should be set to a minimum step-value and for zero or low absolute values, of the friction derivative, the increase should be set to a maximum. To avoid the risk of using small steps at the fully developed viscous friction regime, this function needs to examine the double derivative of the friction. This implementation is relatively more comprehensive, but enables an overall good coverage.

6 Data Analysis

In this chapter the data obtained through the experiments presented in chapter 5 *Experimental Approach* are analyzed and the friction characteristics are derived and evaluated. The data collected from the experiments, presented in section 5.3 *Stribeck curve*, are fitted to the Tustin function through the method presented in section 6.1 *Nonlinear Least Squares Method*. In section 6.2 *Stribeck Curve* and section 6.3 *Efficiency* the data from the steady state and the ramped velocity experiments are analyzed and compared.

6.1 Nonlinear Least Squares Method

The nonlinear least square method is used to derive the constants used to approximate the friction curve generated by the test data. Using the *LSQNONLIN-function* in *MATLAB* nonlinear least squares problems can be solved. The function desired to fit the data needs to be specified. The Tustin function is assumed to be a valid fit as the LuGre- and the Leuven model takes this form at steady state velocity, for the geometric dependent constant $\delta = 1$.

Due to the broad range of functions the nonlinear least squares method is to be fitted to, it is suitable for this application.

For simplicity a walkthrough of the least square method is conducted for a guess on a linear function which is to fit measured values.[MathWorks, 2011]

A linear function is given by equation 6.1, and the parameters a and b are to be optimized so the combined deviation of the data points from the function is minimized.

$$y = a + bx \tag{6.1}$$

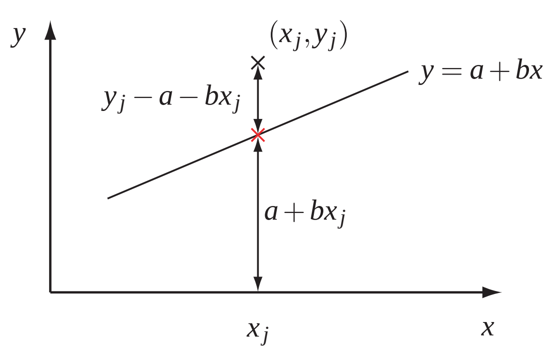

Figure 6.1: Line approximating measured data. The black cross is representing the measured data, and the red cross is the corresponding point of the linear function when inserting x_j.

To evaluate the total deviation, a sum of the squared data point deviations is depicted in equation 6.2.

$$q = \sum_{j=1}^{n} (y_j - a - bx_j)^2 \tag{6.2}$$

The minimization of the squares is performed through a *Levenberg-Marquardt algorithm* which is an iterative optimization routine which interpolates between two curve-fitting algorithms: *Gauss-Newton* and *gradient descent*. The Gauss-Newton algorithm is based on linear approximations of the user-estimated function *y* for small steps. The gradient descent, *or steepest descent*, algorithm converges fast towards the function *y* and minimizes the squared error when evolving in the direction of the negative gradient while updating the steps. The *Levenberg-Marquardt* algorithm excels by using the gradient descent method at very poor parameter estimates and evolves towards the Gauss-Newton algorithm as the step sizes, and the error in parameter estimations, decreases. A shortcoming of the Levenberg-Marquardt algorithm is that it is slightly slower to converge than the Gauss-Newton algorithm at small steps. Another flaw, of this algorithm, is that it can not distinguish between local and global minimum. The latter can be avoided by reasonable initial guesses of the parameters [Madsen et al., 2004], [Garvin, 2011].

The *LSQNONLIN-function* enables boundary conditions which are used to ensure reasonable estimated values. A such boundary condition is obtained through a penalty function, where an error caused by the boundary condition violation, is multiplied by a large constant. The boundary conditions used in the parameter search are listed in table 6.1.

	Lower boundary	Upper boundary
F_C $[N]$	0	$1.0 \cdot 10^5$
$F_{stiction}$ $[N]$	0	$1.0 \cdot 10^5$
$\dot{x}_{Stribeck}$ $[m/s]$	0.05	0.2
B $[Ns/m]$	0	10^5

Table 6.1: Boundary values for the respective parameters.

Note these conditions have been set after reviewing the data from the Stribeck curves and might not be suitable to apply on tests conducted on another setup. Furthermore, the user of *LSQNONLIN-function* should reconsider whether the determined boundary conditions are misguiding if a final estimated parameter has the same value as a boundary value. Using the fitted friction function outside the velocity interval studied is not recommended, as an extrapolation can derive large deviation if the full fluid lubrication regime is not established in the data used for fitting.

6.2 Stribeck Curve

In this section the data measurements are analyzed to investigate the friction characteristics at different operational conditions. Four different load situations have been conducted for both the steady state tests and the velocity ramp tests. The Stribeck curves derived from these tests are compared and evaluated.

The same load is applied in both test situations. The data reviewed in this section are not necessarily of the same data length, as data has been discarded from the segments where the measurements are assumed to be misleading, e.g. if the cylinder has reached an end-stop.

6.2.1 The Influence of Acceleration on Friction

If data from steady state tests are to be compared with those from a ramped velocity test and an evaluation of the accelerations impact on the friction must be done. It is of interest to examine the friction behavior when applying different accelerations to the cylinder, and inspect the dynamic behavior of the friction. In figures 6.2 to 6.5 the influence of the acceleration on the friction is illustrated under different load conditions. The acceleration references used in the experiment are $ddx = 0.067\ [m/s^2]$, $^{ddx}/_{2}$ and $^{3 \cdot ddx}/_{2}$. The signals have been filtered so the individual signals can be distinguished.

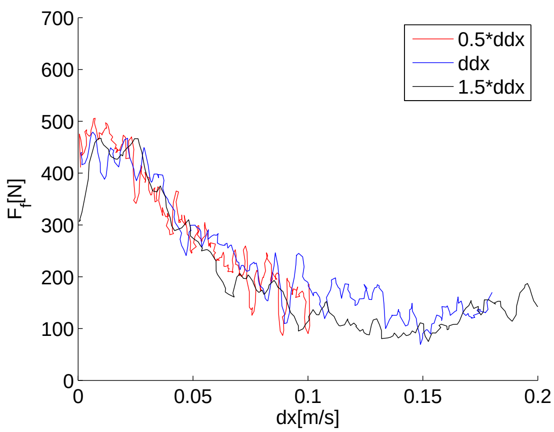

Figure 6.2: Friction curve derived from velocity ramp data for $F_L = 500\ [N]$.

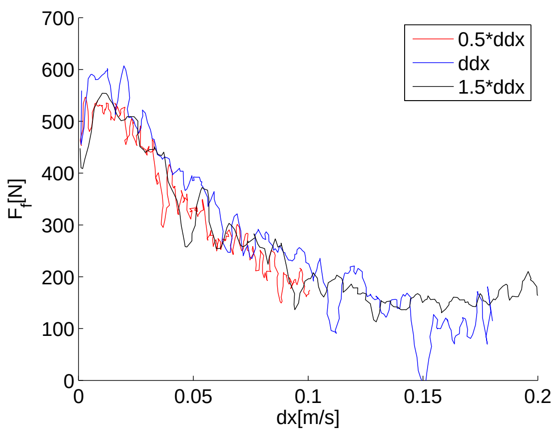

Figure 6.3: Friction curve derived from velocity ramp data for $F_L = 1000\ [N]$.

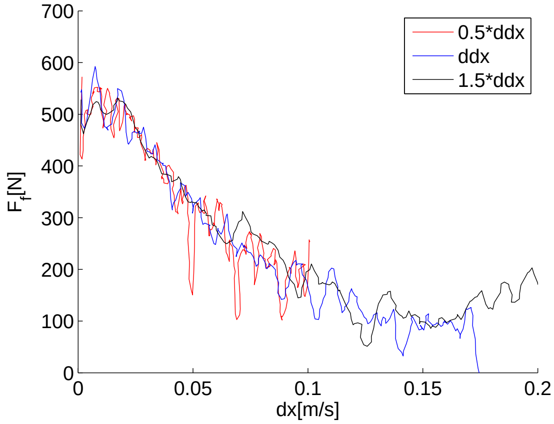

Figure 6.4: Friction curve derived from velocity ramp data for $F_L = 2000$ $[N]$.

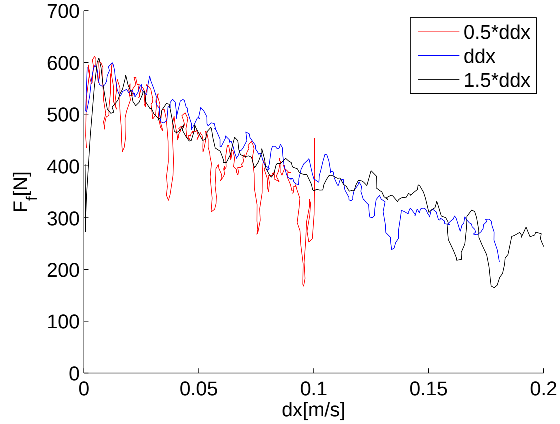

Figure 6.5: Friction curve derived from velocity ramp data for $F_L = 5000$ $[N]$.

No significant influence of the friction can be observed with the chosen accelerations. Ideally the variation of the acceleration could have been further enlarged, though this is not possible on the given test setup. In the following text the steady state data will only be compared with a ramping velocity of $ddx = 0.1$ $[m/s^2]$. The pump can not sustain the supply pressure if the acceleration is raised, and if the acceleration is decreased the cylinder will reach the end-stop and the viscous friction domain is not reached.

6.2.1.1 Load Situation One, 500 [N]

The first case to be studied is a test run with a positive velocity reference and a load of $F_L = 500$ $[N]$. The friction derived from the steady state test, observed in figure 6.6, has an offset compared to the friction derived from the ramped velocity test, seen in figure 6.7. The lower friction level in the ramped test is expected to be due to the presence of frictional lag. Otherwise, the friction has similar characteristic for the two test types, and a saddle point can be distinguished in both plots but with an offset. The friction decreases more rapidly from zero velocity to the saddle point for the velocity ramp than for the steady state data. The viscous friction tendencies are barely starting to show at $\dot{x} > 1.5$, and are therefore insufficient in regard to the viscous friction parameter derivation.

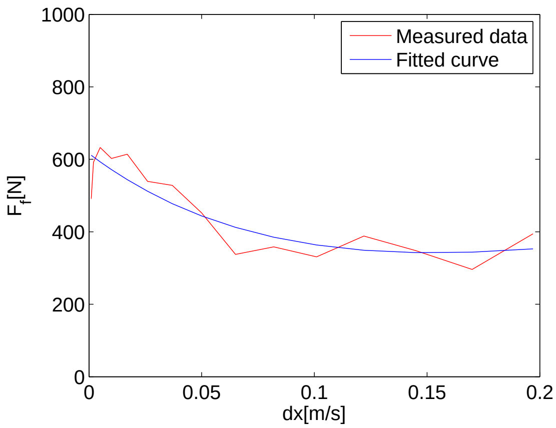

Figure 6.6: Friction curve derived by steady state velocity tests for $F_L = 500$ $[N]$.

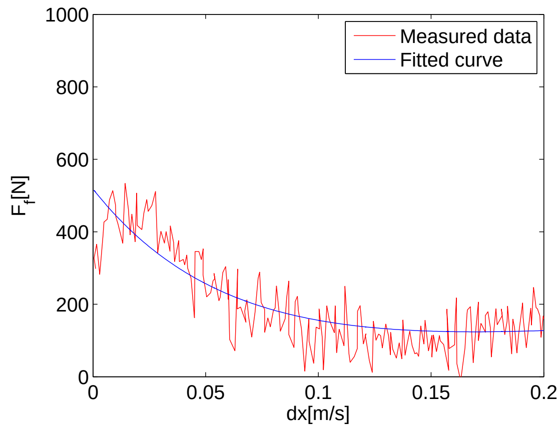

Figure 6.7: Friction when ramping the velocity and applying $F_L = 500$ $[N]$.

In figure 6.6 and 6.7 fitted curves are displayed and the estimated parameters of the two Tustin functions are presented in table 6.3.

	Steady state curve	Velocity ramp
F_C $[N]$	≈ 0	≈ 0
$F_{stiction}$ $[N]$	616	518
$\dot{x}_{stribeck}$ $[m/s]$	0.10	0.06
B $[Ns/m]$	1341	537

Table 6.2: Estimated friction parameters.

As anticipated from the different friction levels the parameters are not coincident. When applying boundary conditions, for the nonlinear least squares method, F_C is set almost equal to zero to produce a reasonable fit. If no boundary conditions is set, the nonlinear least squares method estimates negative values for F_C and compensates by a great estimated value of B. In none of the two plots the expected viscous tendency is present, why the estimated viscous friction coefficient is considered corrupted.

6.2.1.2 Load Situation Two, 1000 [N]

When applying $F_L = 1000$ $[N]$ the friction force close to zero velocity is greater than for the previous load situation. A viscous friction tendency is suspected to occur at $\dot{x} =]0.12; 0.2]$ in figure 6.8. The data does still not reveal sufficient information about the viscous friction.

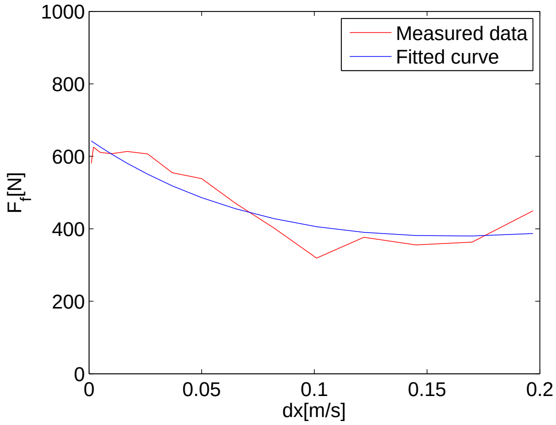

Figure 6.8: Friction curve derived by steady state velocity tests for $F_L = 1000$ $[N]$.

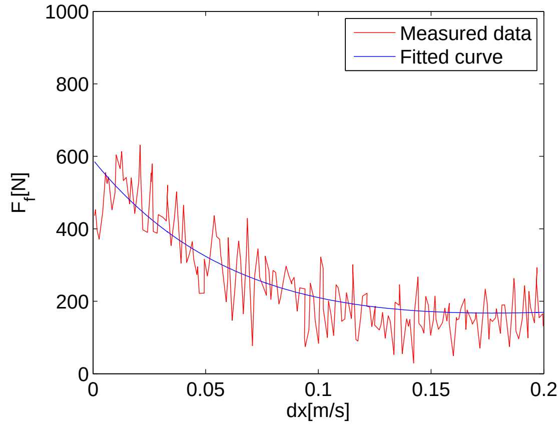

Figure 6.9: Friction when ramping the velocity and applying $F_L = 1000$ $[N]$.

A clear deviation of the friction parameters of the two test types appear in table 6.3. The segment $\dot{x} =]0.1; 0.2]$ can be considered almost uniform when observing figure 6.9, where the viscous tendency is more apparent in figure 6.8. The general development of the friction is similar to $F_L = 500$ $[N]$.

	Steady state curve	Velocity ramp
$F_C[N]$	≈ 0	≈ 0
$F_{stiction}[N]$	647	590
$\dot{x}_{stribeck}[m/s]$	0.11	0.07
$B[Ns/m]$	1381	676

Table 6.3: Friction parameters.

6.2.1.3 Load Situation Three, 2000 [N]

The development of the friction curves from the test runs with $F_L = 1000$ $[N]$ and $F_L = 2000$ $[N]$ are quite alike. But even if the plot are visually alike the corresponding parameters are not.

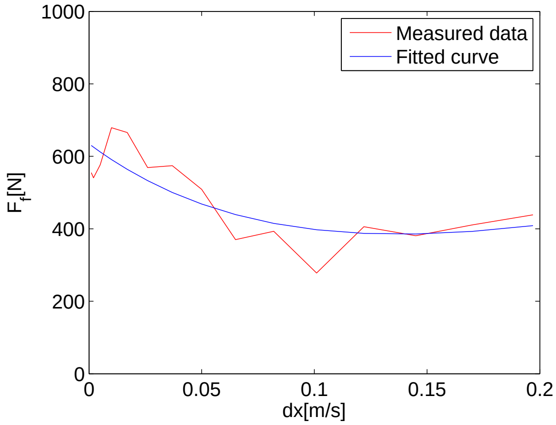

Figure 6.10: Friction curve derived by steady state velocity tests for $F_L = 2000\ [N]$.

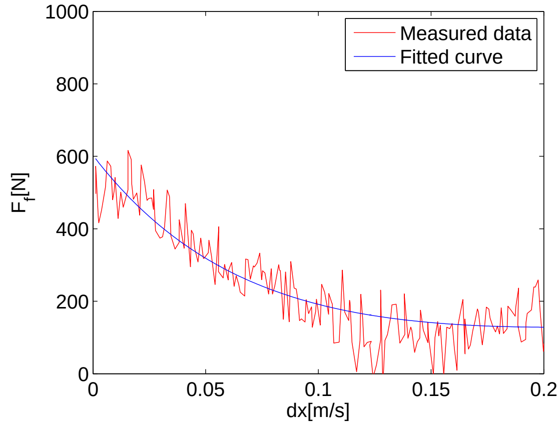

Figure 6.11: Friction when ramping the velocity and applying $F_L = 2000\ [N]$.

	Steady state curve	Velocity ramp
$F_C\ [N]$	≈ 0	≈ 0
$F_{stiction}\ [N]$	634	603
$\dot{x}_{stribeck}\ [m/s]$	0.10	0.07
$B\ [Ns/m]$	1611	469

Table 6.4: Friction parameters.

6.2.1.4 Load Situation Four, 5000 [N]

The friction curves from this last load situation are more distinctive than the previous cases. Both figure 6.12 and 6.13 have a high overall friction level. It is observed for the data collected from the velocity ramping experiment under this load condition, that no obvious Stribeck effect nor viscous friction is present.

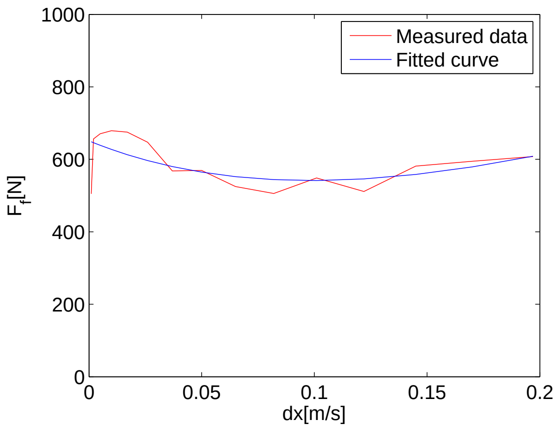

Figure 6.12: Friction curve derived by steady state velocity tests for $F_L = 5000$ $[N]$.

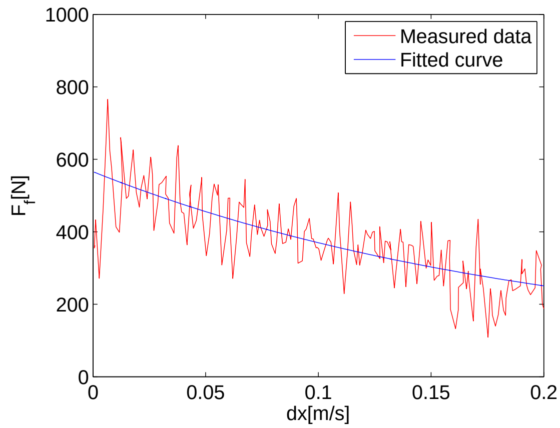

Figure 6.13: Friction when ramping the velocity and applying $F_L = 5000$ $[N]$.

No obvious viscous dominated regime is present for the velocity ramp, and therefore a major deviation from the steady state parameters occurs.

	Steady state curve	Velocity ramp
F_C $[N]$	≈ 0	67
$F_{stiction}$ $[N]$	651	566
$\dot{x}_{stribeck}$ $[m/s]$	0.13	0.2
B $[Ns/m]$	2331	≈ 0

Table 6.5: Friction parameters.

6.2.2 Directional Influence on Friction

To investigate the influence of the seals, friction curves for the positive and negative velocity regimes are plotted together. In figure 6.14 and 6.15 for $F_L = 500$ $[N]$ and $F_L = 5000$ $[N]$, respectively, a difference in the friction levels for positive and negative velocities are shown. Thus, it can be concluded that it is necessary to determine the parameters for both regimes to be able to simulate the friction.

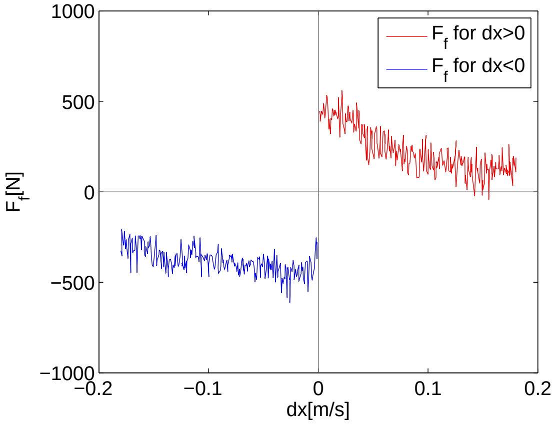

Figure 6.14: Friction curve covering both positive and negative velocity regime for velocity ramp test with $F_L = 500$ $[N]$.

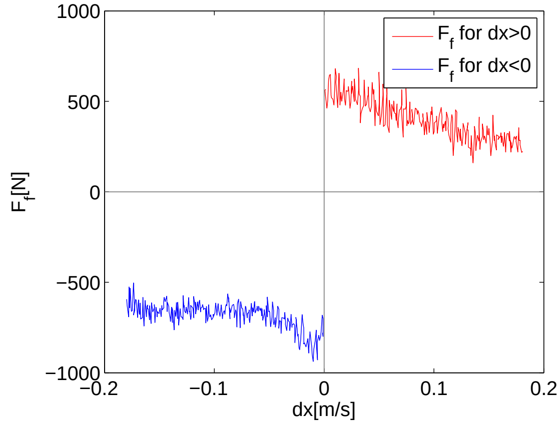

Figure 6.15: Friction curve covering both positive and negative velocity regime for velocity ramp test with $F_L = 5000[N]$.

6.2.3 Hysteresis Loop

In section 3.1.3 *Friction Hysteresis* frictional hysteresis loops where first mentioned. Hysteresis loops originate from systems exhibiting rate or path dependence, and the hydraulic cylinder is analyzed for this by setting a triangularly velocity reference. A triangularly input signal is seen in figure 6.16, and the resulting hysteresis loops in figure 6.17 and 6.17.

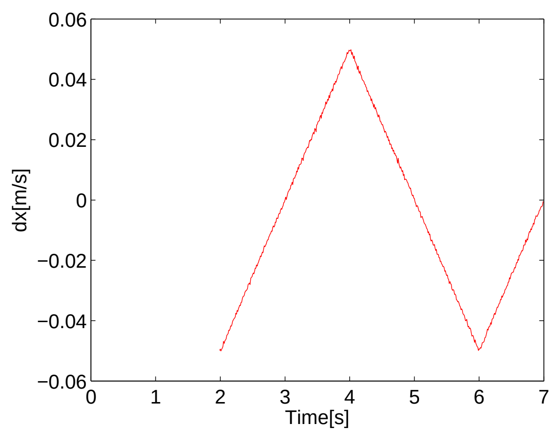

Figure 6.16: Velocity profile for hysteresis loop.

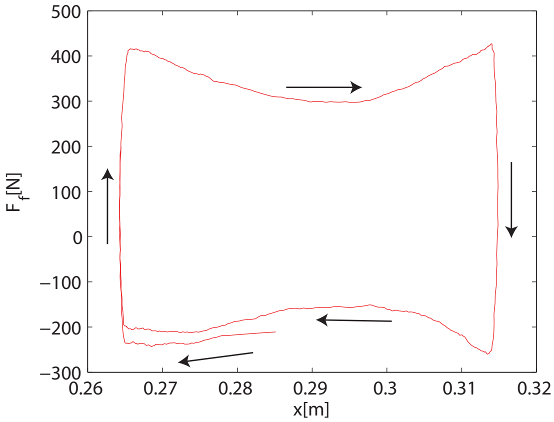

Figure 6.17: Path dependent hysteresis loop for the velocity profile illustrated in figure 6.16. The force signal has been filtered.

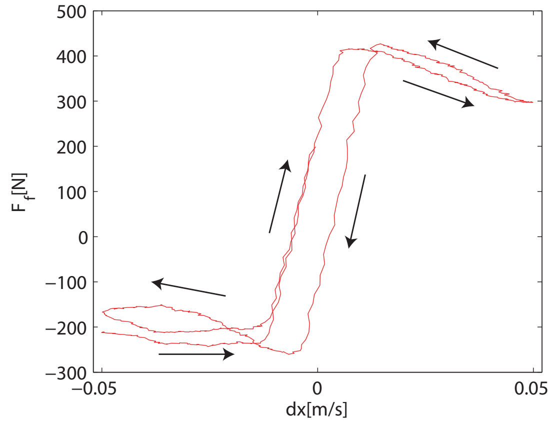

Figure 6.18: Rate dependent hysteresis loop for the velocity profile illustrated in figure 6.16. The force signal has been filtered.

From figure 6.18 it can be realized that friction under acceleration differs from friction under deceleration, and hence a friction model should take this phenomenon into account. The generated hysteresis loop is in accordance with [Al-Bender et al., 2005]. The reader needs to be aware of the force measurements presented in this test being inaccurate, due to faulty strain gage calibration. The strain gage calibration is not considered to influence the overall shape of the loop.

6.2.4 General Review of Friction results

Reviewing the measured data reveals information about the friction at steady state and unsteady velocities. It is clear that the parameters found, when fitting the Tustin function to the data of the ramping velocity test, are not suitable for implementation in the friction models which are based on steady state parameters. This is due to the significant difference in the derived parameters from the two tests. To cover different operating scenarios it can be concluded that an ideal friction model must be valid for steady state as for unsteady velocities, and be able to include the load force.

The parameters for the Tustin function, derived in the tables 6.2 to 6.5, could lead to the assumption that the general friction force is rising when the load force increases, except for measurement of $F_L = 2000$ $[N]$. In the steady state generated Stribeck curves a saddle point indicates the transition to the viscous friction dominated friction regime. Ramping the velocity appears to displace the saddle point. Thus the friction force reaches a lower friction level than for steady state. The supporting film layer takes time to build up, and this is thought to be the reason why the ramping velocity derives a lower friction than steady state, meaning that the friction is lagging the velocity.

Implementing a precise friction model in a simulation model would also demand the friction parameters for negative velocities, and incorporate the hysteresis behavior due to rate-dependence.

A hypothesis was made that the chamber pressures have a significant influence on the friction. If comparisons between the steady state- and the ramping experiments are to be valid the pressures in the test cylinder must be adequately similar during both tests, due to the assumption of the influence of the seals, section 5.1 *Assumptions and Simplifications.* Figure F.7 to F.16 in *appendix F Experimental Results* are used to verify that comparing the two types of tests are acceptable. From these figures it can be observed that the load cylinder fails to remain a constant pressure when ramping the velocity. Though the load is not sustained the chamber pressures are still matching in a acceptable manner.

6.2.5 Confidence Intervals for Steady State Tests

When averaging the friction force used to generate the Stribeck curve from the steady state data, a confidence interval can be derived for the averaged value:

$$\left[\hat{F}_f - \frac{tS}{\sqrt{n}}, \hat{F}_f + \frac{tS}{\sqrt{n}}\right] \tag{6.3}$$

Where:

$\hat{F}_f$:	Mean value of the friction	$[N]$
S :	The variance of the measured data	$[-]$
t :	Student$'$s t-distribution	$[-]$
n :	Number of measurements, set to 3	$[-]$

The Student$'$s t-distribution can be found from [Walpole et al., 2007] for a two sided distribution to be equal to 3.182 for a 95% confidence interval. The variance can be calculated as in equation 6.4.

$$S^2 = \frac{1}{n-1}\sum_{i=1}^{n}\left(\hat{F}_{f,i} - \hat{F}_f\right)^2 \tag{6.4}$$

The confidence interval for the Stribeck curve generated by steady state velocities can be derived when combining equation 6.3 and 6.4. In figure 6.19 the confidence interval for $F_L = 5000\ [N]$ is found.

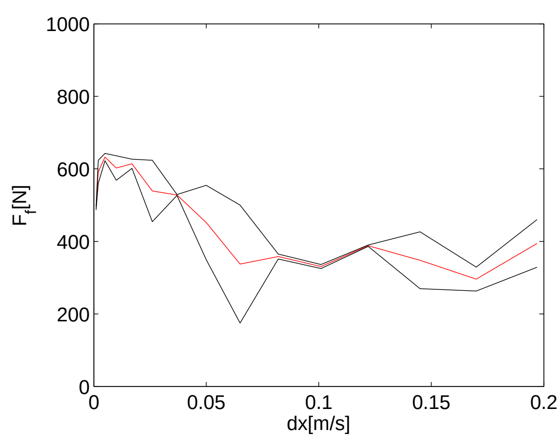

Figure 6.19: Confidence interval for steady state Stribeck curve with $F_L = 500\ [N]$.

Confidence intervals for the last three Stribeck curves can be found in section F.3.1 *Confidence Interval*, figure F.17 to F.19. From the plots it can be concluded that the number of trials used to average over should be set up, and that figure F.17 is the most representative Stribeck curve, as the least variance is found in this data.

As it was concluded that a Stribeck curve derived from a ramped velocity deviates from a steady state curve, it is recommend to use values found from the steady state test. The *LuGre* and *Modified Leuven* model are both estimating the dynamic frictional behavior on the basis of steady state parameters. It would therefore be wrong to use values from a ramped velocity test as parameters for the *LuGre* and *Modified Leuven* model. Depending on whether the cylinder is used with at steady state velocity or shifting velocity, parameters from either the steady state or ramping velocity could be implemented in the *Márton and Lantos* model.

6.3 Efficiency

From the data collected in the Stribeck curve experiments, it is also possible to determine the efficiency of the cylinder. The efficiency of a cylinder is often stated as a single value covering every working situation by the manufactures. If the friction is proven to be dependent on the velocity or even the load force it would be of interest to investigate the efficiency at different velocities and loads. The overall efficiency η_{cyl} of the cylinder is given by equation 6.5.

$$\eta_{cyl} = \frac{\tilde{P}_{mech}}{\tilde{P}_{hyd}} \tag{6.5}$$

Where the mechanical power $\tilde{P}_{mech}$ and hydraulic power $\tilde{P}_{hyd}$ are given in equation 6.6 and 6.7.

$$\tilde{P}_{hyd} = Q_{Tp}P_{Tp} - Q_{Tr}P_{Tr} \tag{6.6}$$

$$\tilde{P}_{mech} = (P_{Tp}A_{Tp} - P_{Tr}A_{Tr} - F_{fT})\dot{x} \tag{6.7}$$

There is not mounted any flow transducers on the cylinder hoses, why the flow into the test cylinder chambers, Q_{Tp} and Q_{Tr}, are derived from equation 6.8 and equation 6.9, which is acceptable in steady state situations where no remarkable pressure build up is present.

$$Q_{Tp} = A_{Tp}\dot{x} \tag{6.8}$$

$$Q_{Tr} = A_{Tr}\dot{x} \tag{6.9}$$

This leads to the efficiency giving in equation 6.10.

$$\eta_{cyl} = \frac{\tilde{P}_{mech}}{\tilde{P}_{hyd}} = \frac{F_{Applied}}{P_{Tp}A_{Tp} - P_{Tr}A_{Tr}} \tag{6.10}$$

The friction of the cylinder is not constant when varying the velocity, and therefore the efficiency is examined for any variation. In this section the efficiency for $F_L = 500$ $[N]$ and $F_L = 5000$ $[N]$ are analyzed.

6.3.1 Load Situation One, 500 [N]

The efficiency when applying $F_L = 500$ $[N]$ is found to be velocity dependent. The efficiency achieved by steady state data, presented in figure 6.20, is less than the efficiency from the velocity ramp data in figure 6.21. It can be concluded that the efficiency near zero velocity is low, due to the relatively high friction values. The data is not covering the viscous dominated segment of the friction curve and it can not be ruled out that the efficiency would decrease at higher velocities.

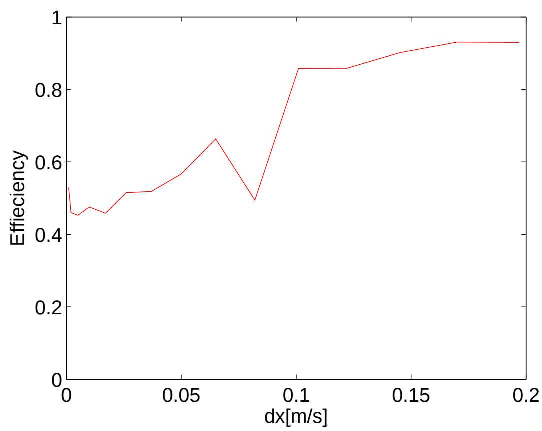

Figure 6.20: Efficiency curve derived from steady state velocity curve data for $F_L = 500$ $[N]$.

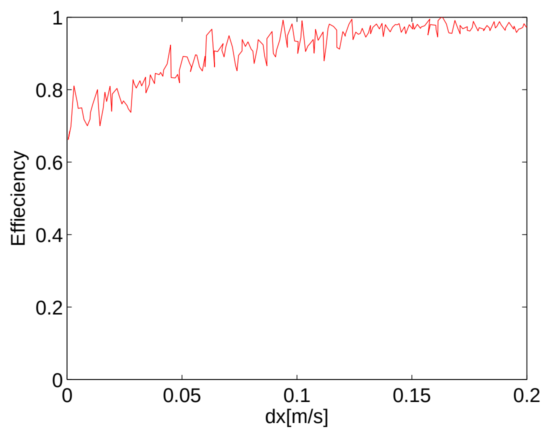

Figure 6.21: Efficiency curve derived from velocity ramp data for $F_L = 500$ $[N]$.

6.3.2 Load Situation Four, 5000 [N]

Comparing the efficiency for the test run with $F_L = 500$ $[N]$ and $F_L = 5000$ $[N]$ it can be concluded that the efficiency is better for high loads in the given velocity interval. In contrast to low loads a more uniform efficiency is attained in the velocity interval.

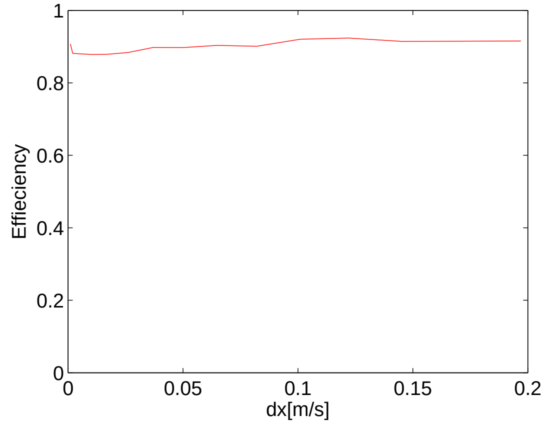

Figure 6.22: Efficiency curve derived from steady state velocity curve data for $F_L = 5000\ [N]$.

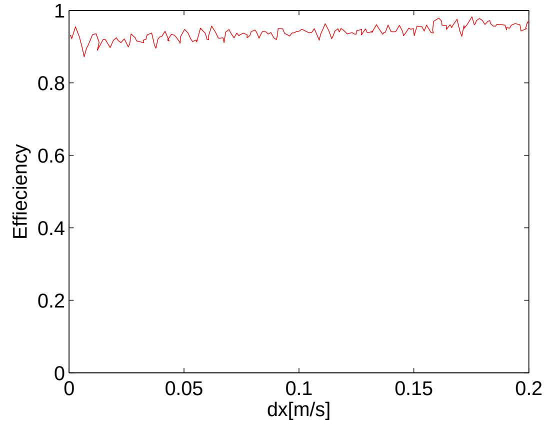

Figure 6.23: Efficiency curve derived from velocity ramp data for $F_L = 5000\ [N]$.

When working at low velocity and low load forces it is important to have a low friction cylinder to be energy efficient, where as the friction does not have the same relative importance at high loads. Efficiency curves for $F_L = 1000\ [N]$ and $F_L = 2000\ [N]$ are given in *appendix F Experimental Results.*

6.3.3 Efficiency Uncertainty

To derive the bias uncertainty of the efficiency plots, a first order Taylor series is used, as seen in equation 6.11 for a general function f including the parameters x_i.

$$f = f_0 + \frac{\partial f}{\partial x_1}\delta_{x_1} + \frac{\partial f}{\partial x_2}\delta_{x_2} + \ldots \tag{6.11}$$

$$\delta_f = \frac{\partial f}{\partial x_1}\delta_{x_1} + \frac{\partial f}{\partial x_2}\delta_{x_2} + \ldots \tag{6.12}$$

$$\delta_f^2 = \left(\frac{\partial f}{\partial x_1}\delta_{x_1} + \frac{\partial f}{\partial x_2}\delta_{x_2} + \ldots\right)^2 \tag{6.13}$$

$$\delta_f^2 = \left(\frac{\partial f}{\partial x_1}\right)^2 \delta_{x_1}^2 + \left(\frac{\partial f}{\partial x_2}\right)^2 \delta_{x_2}^2 + \cancelto{0}{2\frac{\partial f}{\partial x_1}\frac{\partial f}{\partial x_2}\delta_{x_1}\delta_{x_2}} + \ldots \tag{6.14}$$

In equation 6.14 the covariance is neglected, as it is zero when the parameters are independent of each other. The uncertainty is then given by equation 6.15 [Barry N. Taylor and Chris E. Kuyatt, 1994].

$$\pm\delta_f = \sqrt{\sum_{i=1}^{N}\left(\frac{\partial f}{\partial x_i}\right)^2 \delta_{x_i}^2} \tag{6.15}$$

This is applied on equation 6.10 from chapter 5 *Experimental Approach* and the uncertainty is now defined by .

$$\pm\sigma = \sqrt{\left(\frac{\partial \eta_{cyl}}{\partial F_{Applied}}\right)^2 \delta^2_{F_{Applied}} + \left(\frac{\partial \eta_{cyl}}{\partial P_{Tp}}\right)^2 \delta^2_{P_{Tp}} + \left(\frac{\partial \eta_{cyl}}{\partial P_{Tr}}\right)^2 \delta^2_{P_{Tr}}} \tag{6.16}$$

Where:

$$\frac{\partial \eta_{cyl}}{\partial F_{Applied}} = \frac{1}{P_{Tp}A_{Tp} - P_{Tr}A_{Tr}} \tag{6.17}$$

$$\frac{\partial \eta_{cyl}}{\partial P_{Tp}} = \frac{-F_{Applied}A_{Tp}}{(P_{Tp}A_{Tp} - P_{Tr}A_{Tr})^2} \tag{6.18}$$

$$\frac{\partial \eta_{cyl}}{\partial P_{Tr}} = \frac{F_{Applied}A_{Tr}}{(P_{Tp}A_{Tp} - P_{Tr}A_{Tr})^2} \tag{6.19}$$

The uncertainty of the measured force is partly introduced by the possibility that the strain gages could have been mounted faulty. If the strain gages are not placed correctly in accordance to the longitudinal line of the load cell, the angle produces a deviation. This deviation is considered to be small, due to the geometrical relation. In [Mouritsen, 2010] an example with a strain gage is presented and the tolerance of the strain/voltage behavior is set to 0,1%. The signal output from the strain gage amplifier experiences significant noise, and recalibration was needed during the project period, and therefore the tolerance is set to 1.0%. The tolerance of the pressure tranducers are maximum 0.8%,[Danfoss, 2010].

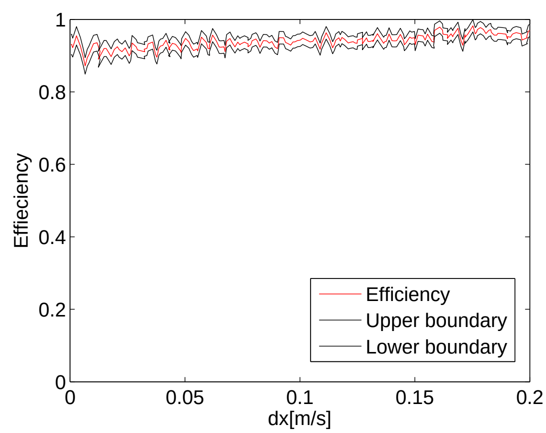

Figure 6.24: Uncertainty interval for efficiency curve derived by a ramped velocity and $F_L = 5000$ $[N]$.

In figure 6.24 a very small uncertainty interval can be observed, and therefore it can be concluded that the tolerances of the test bench are satisfying. The response of figure 6.24 is characterized by being noisy and if the noise is a pure white noise, a more aggressive filter could be applied. A too aggressive filter would corrupt measurements of fast dynamics.

7 Conclusion & Discussion

During the project period several aspects where covered. The control of the system was developed with the purpose to use the test bench in the defined experiments where the frictional behavior was investigated. The friction was assumed to depend on the relative velocity of the moving body and the load applied on the test cylinder. Therefore a control was derived that could control the velocity of the test cylinder and the resulting force produced by the load cylinder. Control of the velocity with no steady state error at step inputs could be obtained by a simple PI-controller. The measured velocity lagged the reference due to the system controlled being a type zero system, but still in an acceptable range. The load cylinder consisting of two type zero systems also performed as anticipated, and no experiments with the demand for a variable load force during a test was conducted, hence no steady state errors where observed. Some tuning of the controllers where done to improve the performance of the test bench but the theoretical derived controllers provided good initial values. The force applied on the test cylinder differs from the referenced resulting force of the load cylinder specified, due to the friction in the load cylinder. To compensate for this a compensation of the friction could be done in the control strategy, or by using the strain gage signal as an input for a force control. If a force control was to be used then the noise present in the strain gage signal should be strived to be significantly reduced by shorter and shielded cables.

Before investigating the specific friction behavior of the given test cylinder it was chosen to form an overview of the existing friction phenomena. With the known friction phenomena at hand, an experimental approach was stated. From the experiments carried out an overview of the friction behavior occurring in the test cylinder was achieved as expected. Friction characteristics discussed where shown to apply for the cylinder. From the friction data, Stribeck curves could be generated and fitted with a Tustin friction model. The data revealed the need for a model capable of simulating the friction both at steady state velocity and unsteady velocities, as the friction parameters for the two situations where dissimilar.

The friction parameters found through the Stribeck tests where to be implemented in the Simulink model so a verification of the models could be accomplished, but as an unstable response in the Simulink model was observed, the friction models could not be verified. The friction models implemented in the simulation model where the *Márton and Lantos*- and the *LuGre*- model. The first model mentioned has an easy implementation and the LuGre model can simulate different dynamic friction phenomena. The LuGre model was chosen instead of the *Leuven* model due to relatively simple implementation. For both the Leuven and LuGre model advanced parameter estimation methods are to be used.

When considering which friction model to use when implementing a friction model in an online estimator, used to compensate for friction, it is of essence to evaluate the importance of the detailed knowledge, which the friction models can estimate. When considering applications where e.g. a precise position control is required a detailed friction model can help compensation for friction at low velocities, and thereby prevent stick slip behavior. In other applications the friction can be neglected or compensated for by simple controllers derived from models with simple friction representation.

A partly automatic standard procedure for determining the friction parameters was stated, and used during the project period for deriving friction parameters. If the test bench was to be turned into a full automatic friction determining tool a graphical user interface should be produced so the code composer debug mode could be omitted. During the project period an accelerometer board was constructed but due to a drifting output, the accelerometer was rejected. If more time was given an acceptable implementation of the accelerometer would be possible, and the velocity could be derived from this instead of the position sensor. The potentiometer placed in the load cylinder, was chosen not to be displayed when introducing the system. This potentiometer can however be used if a given test cylinder does not have an integrated potentiometer. This would be simple to account for in the control program. It was assumed that the pressures would have an impact on the friction but the control of the pressures in the test cylinder where limited. If a more detailed study of the seals friction contribution where to be determined the load cylinder could be used as test cylinder. Thereby the pressures in the new test cylinder could be controlled very precise and the velocity would still be maintained by the other cylinder.

During the experiments, a variation of the supply pressure was observed. An improvement to the existing hydraulic setup is proposed to stabilize the supply pressure. Unlike a typical PVG with a bypass circuit, the mounted servo valves do not have a bypass circuit and therefore a shift in supply pressure occurs when a sudden demand for flow is necessary. This problem can be solved by adding a bypass circuit or an accumulator to the hydraulic setup.

In the articles found covering the friction phenomena in hydraulic cylinders it is often chosen to use a simple setup, where a weight is loaded onto the cylinder. By decoupling the load cylinder, the performance of the load cylinder is not influencing the friction data. By adding weight as needed the desired load situation can be achieved, but no variable load during a test run would be possible.

Bibliography

Al-Bender, F. [2005], 'FUNDAMENTALS OF FRICTION MODELING'. Katholieke Universiteit Leuven.

Al-Bender, F., Lampaert, V. and Swevers, J. [2005], 'The Generalized Maxwell-Slip Model: A Novel Model for Friction Simulation and Compensation', *IEEE TRANSACTIONS ON AUTOMATIC CONTROL* **50**(11).

Armstrong-Hélouvry, B., Dupont, P. and de Wit, C. C. [1994], 'A survey of models, analysis tools and compensation methods for the control of machines with friction', *Automatica, Vol. 30, No. 7* . CD/Bibliography/Armstrong1994.pdf.

Barry N. Taylor and Chris E. Kuyatt [1994], 'Guidelines for evaluating and expressing the uncertainty of NIST measurement results', [Online]. Cited 29. Maj 2011
`http://www.nist.gov/pml/pubs/tn1297/index.cfm`.

Bonchis, A., Corke, P. I. and Rye, D. C. [1999], 'A Pressure-Based, Velocity Independent, Friction Model for Asymmetric Hydraulic Cylinders', *International Conference on Robotics & Automation* .

Çengel, Y. A. and Turner, R. H. [2005], *Fundamentals of Thermal- Fluid Sciences*, 2. edn, McGraw Hill, Singapore. ISBN: 007-245426-1.

Danfoss [2010], 'Tryktransmitter til industriel anvendelse Type MBS 32 og MBS 33', [Online]. Cited 27. Maj 2011
`http://www.ra.danfoss.com/TechnicalInfo/Literature/Manuals/04/ICPDP20X201.pdf`.

de Wit, C. C., Olsson, H., Åström, K., Gäfvert, M. and Lischinsky, P. [1995], 'A New Model for Control of Systems with Friction', *IEEE TRANSACTIONS ON AUTOMATIC CONTROL* **40**(3).

Dennis S. Bernstein [2011*], 'Backlash, Bifurcation, and Buckling and the Mysterious Origin of Hysteresis', [Online]. Cited 29. May 2011
`http://aerospace.engin.umich.edu/people/faculty/bernstein/papers/HystTalkJan022008VWebSite.pdf`.

Garvin, H. [2011], 'The Levenberg-Marquardt method for nonlinear least squares curve-fitting problems'.

Henriksen, D. [2010], *Design and Construction of a Facility for Testing Friction in Hydraulic Cylinders*.

Hoffmann, K. [1989], *An Introduction to Measurements using Strain Gages*, 1. edn, Hottinger Baldwin Messtechnik GmbH, Darmstadt, Darmstadt, Germany.

Kato, S., Marui, E. and Hashimoto, M. [1998], 'Fundamental Study on Normal Load Dependency of Friction Characteristics in Boundary Lubrication', *Tribology Transactions* **41**(3), 341–349.

Lambert, V., Swevers, J. and Al-Bender, F. [2002], 'Experimental Comparison Of Differend Friction Models For Accurate Low-Velocity Tracking', *Proceedings of the 10th Mediterranean conference on control and Automation* .

Madsen, K., Nielsen, H. and Tingleff, O. [2004], 'METHODS FOR NON-LINEAR LEAST SQUARES PROBLEMS'.

MathWorks [2011], 'lsqnonlin', [Online]. [Cited 6. May 2011] `http://www.mathworks.com/help/toolbox/optim/ug/lsqnonlin.html`.

Meikandan, N., Raman, R. and Singaperumal, M. [1994], 'Experimental study of friction in hydraulic actuators with sealless pistons', *Wear* (176), 131–135.

Mouritsen, O. . [2010], 'Grundlæggende usikkerhedsvurdering ved måling med strain gages.'.

Márton, L. and Lantos, B. [2006], 'Identification and Model-based Compensation of Striebeck Friction', *Acta Polytechnica Hungarica* **3**(3).

Phillips, C. L. and Harbor, R. D. [2000], *Feedback Control Systems*, 4. edn, Prentice Hall, Upper Saddle River, New Jersey. ISBN: 0-13-949090-6.

Studienævnet for Industri og Global Forretningsudvikling [2010], '*Elektro-Mekanisk System Design, 3. semester*', [Online]. [Cited 15. Dec 2010] `http://www.misg.aau.dk/sv/emsd/emsd9.pdf`.

Swevers, J., Al-Bender, F., Ganseman, C. G. and Prajogo, T. [2000], 'An Integrated Friction Model Structure with Improved Presliding Behavior for Accurate Friction Compensation', *IEEE TRANSACTIONS ON AUTOMATIC CONTROL VOL. 45, NO. 4* .

Walpole, R. E., Myers, R. H., Myers, S. L. and Ye, K. [2007], *Probability & Statistics for Engineers & Scientists*, 8. edn, Pearson Education International.

Part I

Appendix

A Parameter Values

Parameter	Description	Value	Unit
a_d	*Koefficient used in Márton and Lantos model*	–	$[-]$
A	*The contact area of the moving object in contact with the fluid*	–	$[m^2]$
A_{Lp}	*Piston area on the load cylinders piston side*	–	$[m^2]$
A_{Lr}	*Piston area on the load cylinders rod side*	–	$[m^2]$
A_{Tp}	*Piston area on the test cylinders piston side*	–	$[m^2]$
A_{Tr}	*Piston area on the test cylinders rod side*	–	$[m^2]$
b_d	*Koefficient used in Márton and Lantos model*	–	$[-]$
B	*Viscous friction coefficient*	–	$[^{Ns}/_{m}]$
C_{ffLp}	*Feedforward gain*	–	$[-]$
C_{ffLr}	*Feedforward gain*	–	$[-]$
C_{Lp}	*Load cylinder piston pressure controller*	–	$[-]$
C_{Lr}	*Load cylinder rod pressure controller*	–	$[-]$
C_{PI}	*PI controller*	–	$[-]$
C_T	*Controller for test cylinder*	–	$[-]$
E	*Recursive model error*	–	$[-]$
ff	*Feed forward*	–	$[-]$
$F_{Applied}$	*Force measured by strain gage*	–	$[N]$
F_C	*Coulomb friction*	–	$[N]$
F_d	*Linear approximated force*	–	$[N]$
$F_{Exerted}$	*Force exerted on plate in contact with another plate*	–	$[N]$
$F_{f,bristles}$	*Friction force generated when bending the bristles*	–	$[N]$
F_{fL}	*Friction contribution in the load cylinder*	–	$[N]$
F_{fT}	*Friction contribution in the test cylinder*	–	$[N]$
F_{fTotal}	*Total friction force in the system*	–	$[N]$
F_f	*Friction force*	–	$[N]$
$\hat{F}_f$	*Friction force*	–	$[N]$
F_h	*Total friction force in the system*	–	$[N]$
F_L	*Resulting pressure force of the load cylinder*	–	$[N]$
$F_{stiction}$	*Static friction*	–	$[N]$
F_T	*Resulting pressure force of the test cylinder*	–	$[N]$
F_{Tustin}	*Tustin function*	–	$[-]$
g	*Function used in LuGre*	–	$[-]$
G_{CTcl}	*Controlled closed loop transfer function for test cylinder*	–	$[-]$
G_{CL_pcl}	*Controlled closed loop transfer function for load cylinder piston pressure*	–	$[-]$
G_{CL_rcl}	*Controlled closed loop transfer function for load cylinder rod pressure*	–	$[-]$
G_{CTol}	*Controlled open loop transfer function for test cylinder*	–	$[-]$
G_{CL_pol}	*Controlled open loop transfer function for load cylinder piston pressure*	–	$[-]$
G_{CL_rol}	*Controlled open loop transfer function for load cylinder rod pressure*	–	$[-]$

Parameter	Description	Value	Unit
G_{EM}	*Equation of motion transfer function*	$-$	$[-]$
G_{L_pol}	*Open loop transfer function for load cylinder piston pressure*	$-$	$[-]$
G_{L_rol}	*Open loop transfer function for load cylinder rod pressure*	$-$	$[-]$
G_{Tol}	*Transfer function for the test cylinder*	$-$	$[-]$
G_{valve}	*Transfer function for the valves*	$-$	$[-]$
k_{1-5}	*Constants used in*	$-$	$[-]$
K_C	*PI controller gain*	$-$	$[-]$
K_I	*Integrator gain for PI controller*	$-$	$[-]$
K_P	*Proportional gain for PI controller*	$-$	$[-]$
$K_{P_{Lp}}$	*Constant for linear equation*	$-$	$[-]$
$K_{P_{Lr}}$	*Constant for linear equation*	$-$	$[-]$
$K_{P_{Tp}}$	*Constant for linear equation*	$-$	$[-]$
$K_{P_{Tr}}$	*Constant for linear equation*	$-$	$[-]$
K_T	*Valve gain the pressure-based model*	$-$	$[-]$
$K_{u_{Tp}}$	*Constant for linear equation*	$-$	$[-]$
$K_{u_{Tr}}$	*Constant for linear equation*	$-$	$[-]$
$K_{u_{Lp}}$	*Constant for linear equation*	$-$	$[-]$
$K_{u_{Lr}}$	*Constant for linear equation*	$-$	$[-]$
m_{eq}	*Total mass of moving bodies*	$-$	$[kg]$
M	*Number of samplings*	$-$	$[-]$
n	*Arbitrary parameter*	$-$	$[-]$
n	*Number of measurements*	$-$	$[-]$
N	*Number of elastoslide elements*	$-$	$[-]$
L	*Gain vector*	$-$	$[-]$
P	*Covariance matrix*	$-$	$[-]$
$\widetilde{P}_{hyd}$	*Hydraulic power*	$-$	$[W]$
$\widetilde{P}_{mech}$	*Mechanical power*	$-$	$[W]$
P_{Lp}	*Pressure in the load cylinders piston side chamber*	$-$	$[Pa]$
P_{Lr}	*Pressure in the load cylinders rod side chamber*	$-$	$[Pa]$
P_s	*Supply pressure*	150	$[Pa]$
P_t	*Reservoir pressure*	2	$[Pa]$
P_{Tp}	*Pressure in the test cylinders piston side chamber*	$-$	$[Pa]$
P_{Tr}	*Pressure in the test cylinders rod side chamber*	$-$	$[Pa]$
q	*Total deviation*	$-$	$[Pa]$
Q_{Ll}	*Leakage flow over the load cylinder piston*	$-$	$[m^3/s]$
Q_{Lp}	*Flow into the load cylinder on the piston side*	$-$	$[m^3/s]$
Q_{Lr}	*Flow into the load cylinder on the rod side*	$-$	$[m^3/s]$
Q_N	*Rated flow*	$-$	$[m^3/s]$
Q_{Tl}	*Leakage flow over the test cylinder piston*	$-$	$[m^3/s]$
Q_{Tp}	*Flow into the test cylinder on the piston side*	$-$	$[m^3/s]$
Q_{Tr}	*Flow out of the test cylinder on the rod side*	$-$	$[m^3/s]$
S	*Function used in modified Leuven model*	$-$	$[-]$
S	*Variance of measured data*	$-$	$[-]$
t	*Time*	$-$	$[s]$
t	*Student's t-distribution*	$-$	$[-]$

Parameter	Description	Value	Unit
t_d	*Dwell time*	–	$[s]$
t_s	*Slip time*	–	$[s]$
T_s	*Sampling time*	–	$[s]$
u	*The measured piston displacement in modified Leuven*	–	$[m]$
u_{L_1}	*Load cylinder rod side valve voltage*	–	$[V]$
u_{L_2}	*Load cylinder piston side valve voltage*	–	$[V]$
u_T	*Test cylinder valve voltage*	–	$[V]$
V_{Lp}	*Volume on the load cylinders piston side*	–	$[m^3]$
V_{Lr}	*Volume on the load cylinders rod side*	–	$[m^3]$
V_{Lp0}	*Initial volume on the load cylinders piston side*	–	$[m^3]$
V_{Lr0}	*Initial volume on the load cylinders rod side*	–	$[m^3]$
V_{Tp}	*Volume on the test cylinders piston side*	–	$[m^3]$
V_{Tr}	*Volume on the test cylinders rod side*	–	$[m^3]$
V_{Tp0}	*Initial volume on the test cylinders piston side*	–	$[m^3]$
V_{Tr0}	*Initial volume on the test cylinders rod side*	–	$[m^3]$
x	*Position of the test cylinder piston*	–	$[m]$
x_0	*Offset of the load cylinder position*	–	$[m]$
$x_{Lstroke}$	*Stroke length of the load cylinder*	–	$[m]$
$x_{Tstroke}$	*Stroke length of the test cylinder*	–	$[m]$
y	*ratio between the spring deformation and the maximum spring deformation*	–	$[m]$
z	*Bristle deflection*	–	$[m]$
z_{SS}	*Steady state bristle deflection*	–	$[m]$
$\dot{z}$	*Rate of bristle deflection*	–	$[m/s]$
$\dot{x}_{max}$	*Maximum velocity present in friction data*	–	$[m/s]$
$\dot{x}$	*Velocity of the cylinder piston*	–	$[m/s]$
$\dot{x}_{Stribeck}$	*Stribeck velocity*	–	$[m/s]$
$\dot{x}_{SW}$	*Switching velocity*	–	$[m/s]$
$\ddot{x}$	*Acceleration of the cylinder pistons*	–	$[m/s^2]$
β	*Bulk modulus of the fluid*	–	$[bar]$
δ	*The deformation of each springin modified Leuven*	–	$[m]$
Δ	*Maximum spring deformation in modified Leuven*	–	$[m]$
Δp_N	*Rated pressure drop*	–	$[Pa]$
ε	*Strain of the load cell obtained by a strain gage*	–	$[-]$
η_{cyl}	*Cylinder efficiency*	–	$[W]$
Φ	*Ratio vector*	–	$[-]$
κ	*Spring constant*	–	$[N/m]$
λ	*Forgetting factor*	–	$[-]$
μ	*Dynamic viscosity*	–	$[sPa]$
θ	*Coulomb force for each element modified Leuven*	–	$[F]$
ρ	*Density of the system fluid*	–	$[kg/m^3]$
σ_0	*Average stiffness of the bristles*	–	$[N/m]$
σ_1	*Micro-viscous coefficient*	–	$[sN/m]$
Θ	*Coulomb forces vector*	–	$[-]$
$\tau_{2\%}$	*Settling time*	–	$[-]$
τ_c	*PI controller time constant*	–	$[-]$

Parameter	Description	Value	Unit
τ	*Shear stress of the fluid*	$-$	$[Pa]$
ω	*Frequency*	$-$	$[-]$
ω_{valve}	*The eigenfrequency of the valves*	90	$[Hz]$
ξ_{valve}	*The damping of the valves response*	1	$[-]$
ζ_{valve}	*Position of each element used in the modified Leuven*	$-$	$[m]$

B Electrical Circuit Boards

The I/O pins on the DSP are configured to handle voltages between zero and 3.0 [V]. Why circuit boards have been constructed to scale the voltage outputted by the sensors to an acceptable range.

A key circuit component configuration is the *Difference Amplifier* which is illustrated in figure B.1 and the resulting voltage output expressed as seen in equation B.1 and B.2.

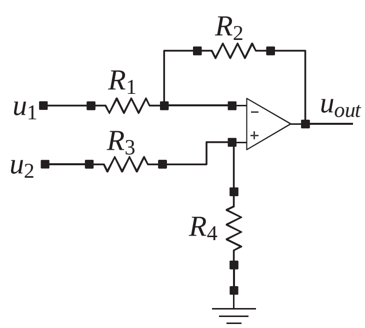

Figure B.1: General Difference Amplifier

$$u_{out} = \left(\frac{R_1 + R_2}{R_3 + R_4}\right)\frac{R_4}{R_1}u_2 - \frac{R_2}{R_1}u_1 \quad \text{(B.1)}$$

For $R_1 = R_3$ and $R_2 = R_4$

$$u_{out} = (u_2 - u_1)\frac{R_2}{R_1} \quad \text{(B.2)}$$

In the following sections the different circuits are presented and the scaling they introduce are documented.

B.1 Pressure Transducer Op-Amp Circuits

The circuits which scales the 0-10 [V] output from the pressure transducer, into a measurable voltage for the DSP is illustrated in figure B.2.

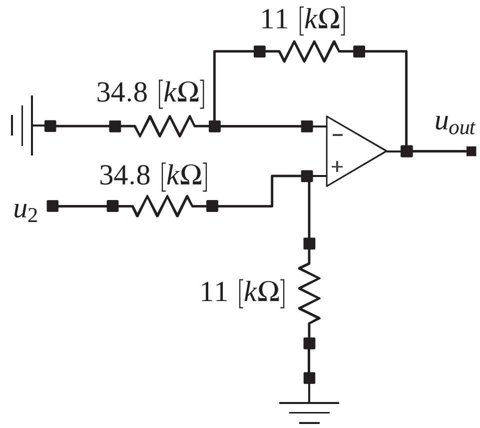

Figure B.2: Pressure transducer board.

To verify the choice of circuit components, the circuit is tested in MapleSim with an alternating input voltage u_2 between zero and 10 [V] and the output voltage is displayed in a graph. Figure B.3 and B.4 illustrate the input and output of the pressure transducer Op-Amp circuits.

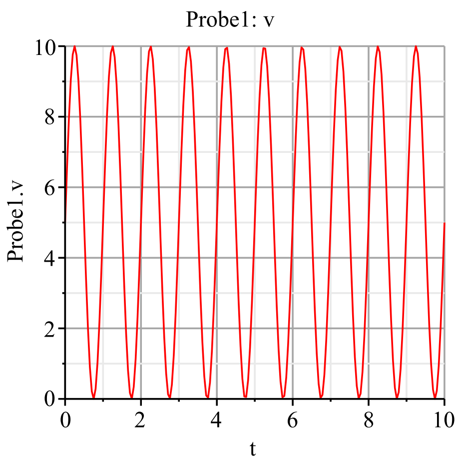

Figure B.3: Simulated input to electrical circuit board for pressure transducers.

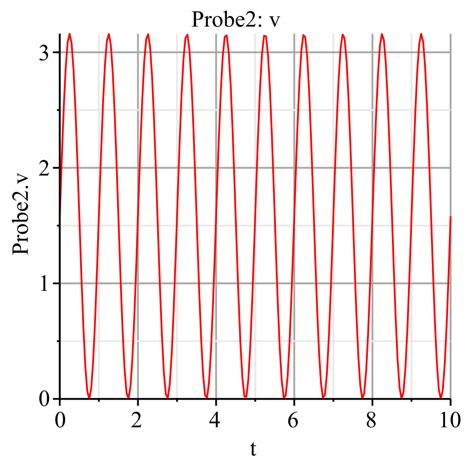

Figure B.4: Simulated output from electrical circuit board for pressure transducers.

Note: The input voltage will not be sinusoidal, but this serves well when considering the input/output-relation. By using equation B.2 on page 81 the scaling equation becomes $u_{out} = 0.316u_2$ and the maximum output voltage is found to $u_{out} = 3.16$ [V] at $u_2 = 10$.

B.2 Accelerometer Op-Amp Circuit

The circuit which scales the 0-5 [V] output from the accelerometer, into a measurable voltage for the DSP is illustrated in figure B.5.

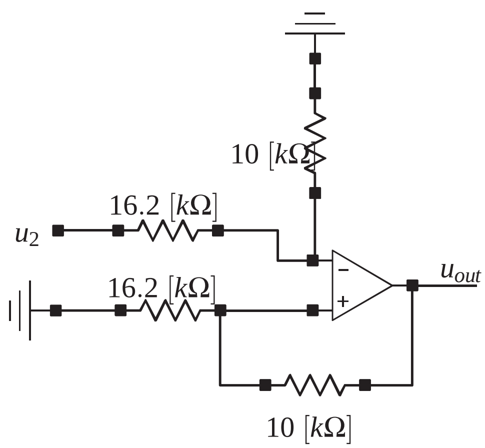

Figure B.5: Accelerometer

To verify the choice of circuit components, the circuit is tested in MapleSim with an alternating input voltage u_1 between zero and 5 [V] and the output voltage is displayed in a graph. Figure B.6 and figure B.7 illustrates the input and output of the accelerometer Op-Amp circuit.

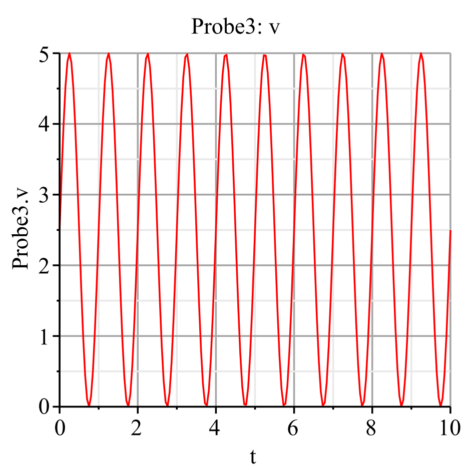

Figure B.6: Simulated input to electrical circuit board for the accelerometer.

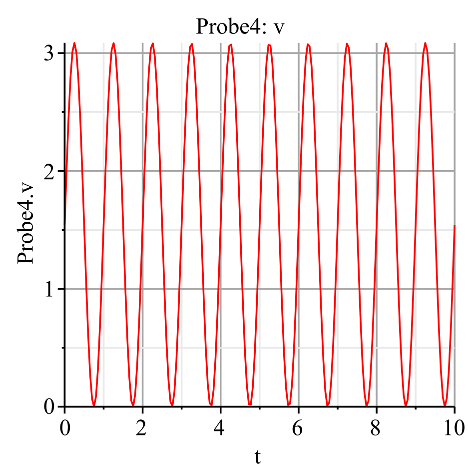

Figure B.7: Simulated output from electrical circuit for the accelerometer.

By using equation B.2 on page 81 the scaling equation becomes $u_{out} = 0.617u_2$ and the maximum output voltage is found to $u_{out} = 3.08$ [V] at $u_1 = 5$.

B.3 Accelerometer And Strain Gage Supply Op-Amp Circuits

To supply the accelerometer and the strain gage with approximative ± 5[V] a simple op-amp circuit is produced. To scale the ± 15[V] down to ± 5[V] two of the circuits in figure B.8 are used.

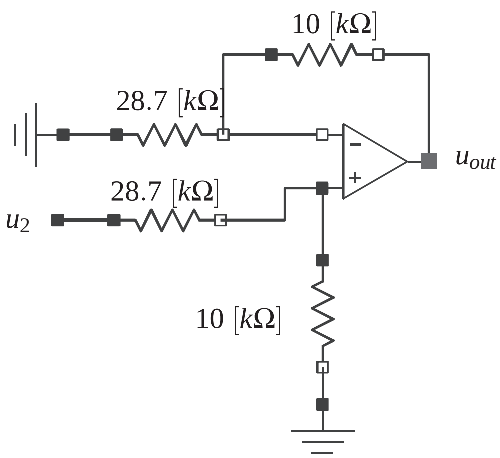

Figure B.8: Board supplying strain gage and accelerometer.

When applying $u_2 = \pm 15$[V], u_{out} will reach a value of ± 5.23 [V].

C Strain Gage Measurements

To measure the applied force on the test cylinder, a strain gage is attached to the load cell which is functioning as a compression bar in the test setup. The applied force on the test cylinder is given as in equation C.1.

$$F_{applied} = \varepsilon_L A_{LoadCell} E \tag{C.1}$$

ε_L is the strain in the longitudinal direction of the compression bar. To compensate for bending strains, thermal strains and to suppress interference effects through internal bridge connections a full bridge setup is used, consisting of four strain gages. The relation between the strains, the supply voltage and the measured output voltage is seen in equation C.2. In equation C.3 the four strains are combined into ε_i, where ε_i is the value that can be measured. k is the "k-factor" describing the proportionality between the strain and the change in resistance.[Hoffmann, 1989]

$$\frac{u_{out}}{u_s} = \frac{k}{4}(\varepsilon_1 - \varepsilon_2 + \varepsilon_3 - \varepsilon_4) \tag{C.2}$$

$$\Rightarrow \frac{u_{out}}{u_s} = \frac{k}{4}\varepsilon_i \tag{C.3}$$

ε_L can be found from equation C.4.

$$\varepsilon_i = 2(1+\upsilon)\varepsilon_L \tag{C.4}$$

υ is the Poisson's ratio. A strain gage amplifier is used when measuring the output voltage of the full bridge. The amplifier has a gain that can be specified by the user, and the relation between the strain gage output voltage and the amplified voltage is therefore as in equation C.5.

$$u_{out,amp} = u_{out} K_{strain} \tag{C.5}$$

This leads to the applied force equation C.6.

$$F_{applied} = \frac{4u_{out,amp} A_{LoadCell} E}{2u_s k (1+\upsilon) K_{strain}} \tag{C.6}$$

D Filters and Difference Equations

In this section the difference equations implemented on the DSP are derived through use of Backward Euler. Using this method the s in Laplace transfer functions are replaced by $\frac{z-1}{T_s \cdot z}$ and transformed to difference equations suited for implementation in the DSP program.

All measurements from the sensors are noisy due to the unscreened cables fails to preserve the uncorrupted analogue signals. To cancel some of the noise, two types of filters are deployed: *first order low pass*-filters and *finite impulse response (FIR)*-filters.

The nature of operation for the FIR-filter is to mean over n-number of measured values. Thereby canceling some of the noise. This results in a phase delay which magnitude depends on the ratio between T_s and n. The transfer function for a FIR-filter is presented in equation D.1.

$$FIR(z) = \frac{1}{n}\sum_{k=0}^{n-1} z^{-k} \tag{D.1}$$

This is transformed to programmable friendly difference equation presented in equation D.4 with the filtered output y, sample counter k and measured value buffer $\widehat{x}$ which is n long.

$$y_{k-1} = 0; \tag{D.2}$$

$$for(k = 0\ ;\ k\ <\ n\ ;\ k{+}{+}) \tag{D.3}$$

$$\{y_k = y_{k-1} + \frac{1}{n}\widehat{x}_k\} \tag{D.4}$$

When using the position to derive the velocity used for control equation D.11 is used. The cable used is not shielded and a first order low pass filter is therefore added.

$$\dot{x} = G_{1.Filter} \cdot s \cdot x = \frac{s}{s\tau_c + 1} \cdot x \tag{D.5}$$

$$\Leftrightarrow \dot{x} = \frac{\left(\frac{z-1}{T_s \cdot z}\right)}{\left(\frac{z-1}{T_s \cdot z}\right)\tau_c + 1} \cdot x \tag{D.6}$$

$$\Rightarrow \dot{x}\left((z-1)\,\tau_c + T_s \cdot z\right) = (z-1) \cdot x \tag{D.7}$$

$$\Leftrightarrow \dot{x}_{k+1}\tau_c - \dot{x}_k\tau_c + \dot{x}_{k+1}T_s = x_{k+1} - x_k \tag{D.8}$$

$$\Leftrightarrow \dot{x}_k\tau_c - \dot{x}_{k-1}\tau_c + \dot{x}_k T_s = x_k - x_{k-1} \tag{D.9}$$

$$\Rightarrow \dot{x}_k\,(\tau_c + T_s) = x_k - x_{k-1} + \dot{x}_{k-1}\tau_c \tag{D.10}$$

$$\Rightarrow \dot{x}_k = \frac{x_k - x_{k-1} + \dot{x}_{k-1}\tau_c}{(\tau_c + T_s)} \tag{D.11}$$

In equation D.18 a general difference equation for the PI controllers is shown.

$$
\begin{aligned}
u = G_{PI}e &= K_c \frac{s\tau_c + 1}{s} e && \text{(D.12)}\\
\Leftrightarrow u &= K_c \frac{\left(\frac{z-1}{T_s \cdot z}\right)\tau_c + 1}{\left(\frac{z-1}{T_s \cdot z}\right)} e && \text{(D.13)}\\
\Leftrightarrow u\left(\frac{z-1}{T_s \cdot z}\right) &= K_c \left(\frac{z-1}{T_s \cdot z}\right)\tau_c e + K_c e && \text{(D.14)}\\
\Leftrightarrow u &= K_c \tau_c e + K_c e \left(\frac{T_s \cdot z}{z-1}\right) && \text{(D.15)}\\
\Leftrightarrow u(z-1) &= K_c \tau_c e (z-1) + K_c e (T_s \cdot z) && \text{(D.16)}\\
\Leftrightarrow u_{k+1} - u_k &= K_c \tau_c e_{k+1} - K_c \tau_c e_k + K_c T_s e_{k+1} && \text{(D.17)}\\
\Leftrightarrow u_k &= K_c \tau_c e_k - K_c \tau_c e_{k-1} + K_c T_s e_k + u_{k-1} && \text{(D.18)}
\end{aligned}
$$

To calculate the velocity from the acceleration equation D.23 is used.

$$
\dot{x} = \ddot{x}\frac{1}{s} \tag{D.19}
$$

$$
\begin{aligned}
\Leftrightarrow \dot{x} &= \ddot{x}\left(\frac{T_s \cdot z}{z-1}\right) && \text{(D.20)}\\
\Leftrightarrow \dot{x}(z-1) &= \ddot{x}(T_s \cdot z) && \text{(D.21)}\\
\Leftrightarrow \dot{x}_{k+1} - \dot{x}_k &= \ddot{x}_{k+1} T_s && \text{(D.22)}\\
\Leftrightarrow \dot{x}_k &= \ddot{x}_k T_s + \dot{x}_{k-1} && \text{(D.23)}
\end{aligned}
$$

The filters implemented in the DSP program for filtering the signal from the pressure transducers are given in equation D.29.

$$
\begin{aligned}
P_{filtered} &= K \frac{1}{s\tau + 1} P_M && \text{(D.24)}\\
\Rightarrow P_{filtered} &= K \frac{1}{\left(\frac{z-1}{T_s \cdot z}\right)\tau + 1} P_M && \text{(D.25)}\\
\Rightarrow P_{filtered}\left((z-1)\tau + T_s \cdot z\right) &= K P_M T_s \cdot z && \text{(D.26)}\\
\Rightarrow P_{filtered,k+1}\tau - P_{filtered,k}\tau + P_{filtered,k+1} T_s &= K P_{M,k+1} T_s && \text{(D.27)}\\
\Rightarrow P_{filtered,k}\tau - P_{filtered,k-1}\tau + P_{filtered,k} T_s &= K P_{M,k} T_s && \text{(D.28)}\\
\Rightarrow P_{filtered,k} &= \frac{K P_{M,k} T_s + P_{filtered,k-1}\tau}{\tau + T_s} && \text{(D.29)}
\end{aligned}
$$

E Control System Plots

E.1 Control Plots for Test System

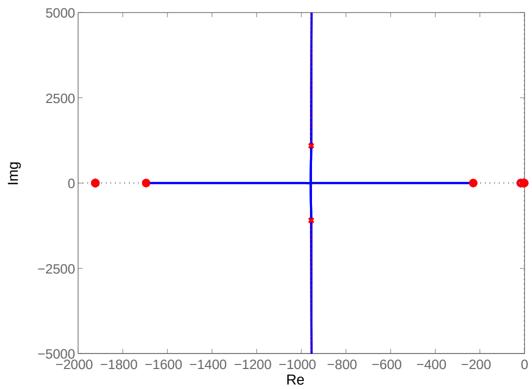

Figure E.1: Root locus of G_{CTol} (blue) and G_{CTcl} (red).

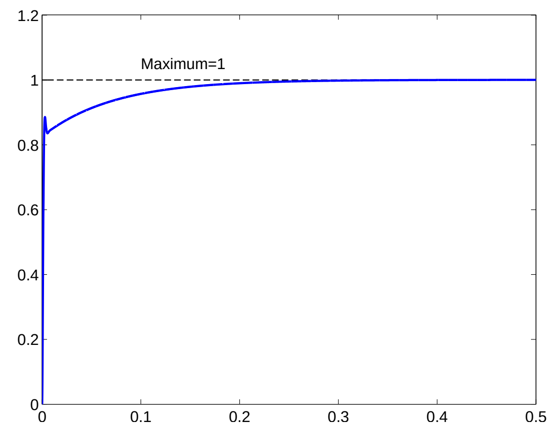

Figure E.2: Unity step response of G_{CTcl}.

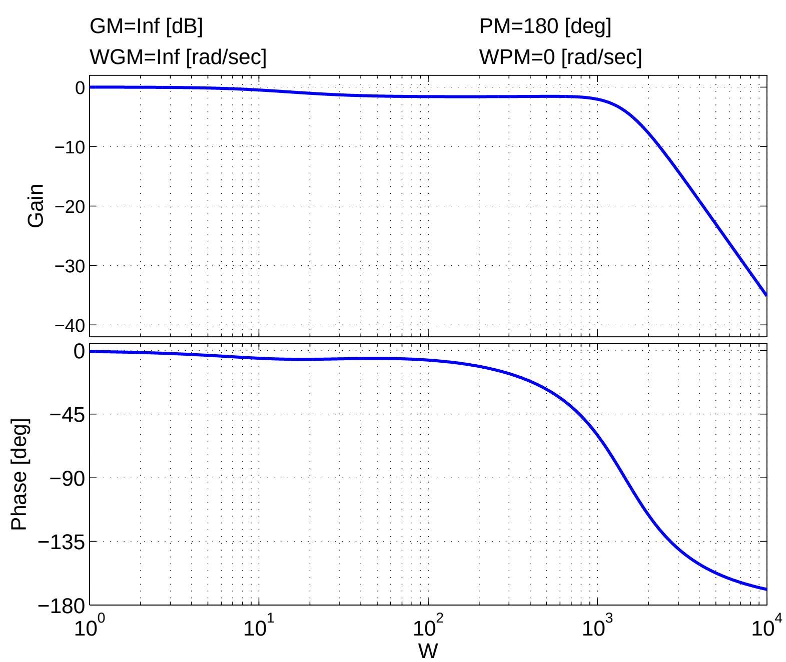

Figure E.3: Bode Plot, GM is the gain margin, WGM is the frequency at GM, PM is the phase margin, WPM is the frequency at PM.

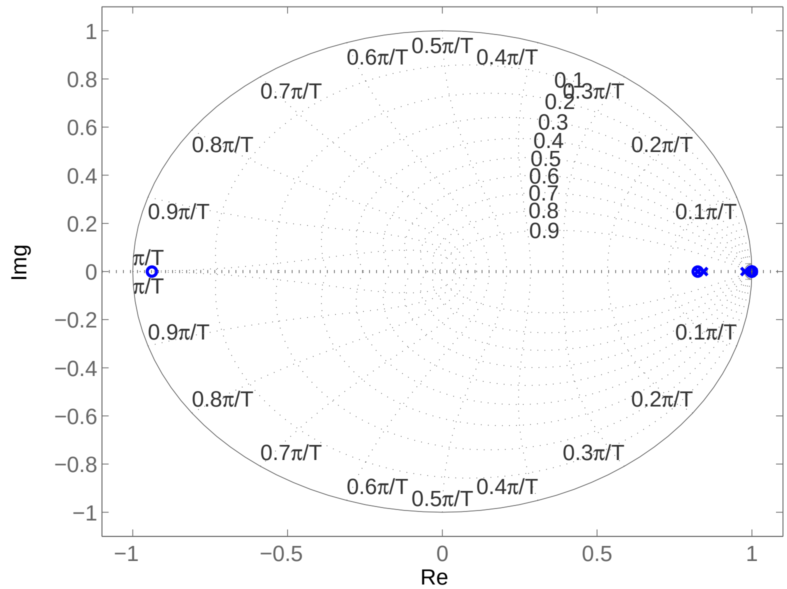

Figure E.4: Pole zero map.

E.2 Control Plots for Load-rod System

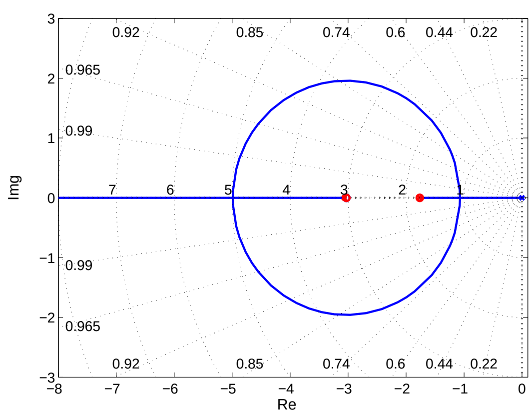

Figure E.5: Root locus of $G_{CL_{r}ol}$ (blue) and $G_{CL_{r}cl}$ (red).

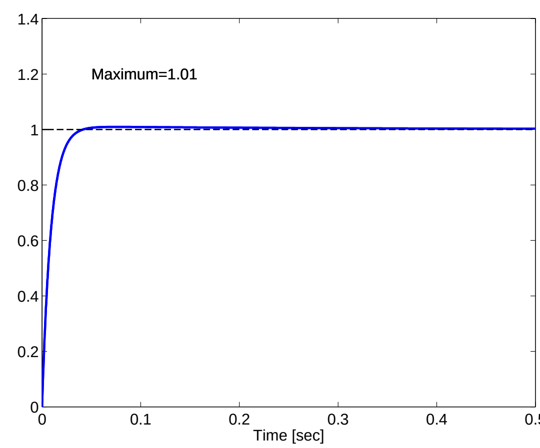

Figure E.6: Unity step response of $G_{CL_{r}cl}$.

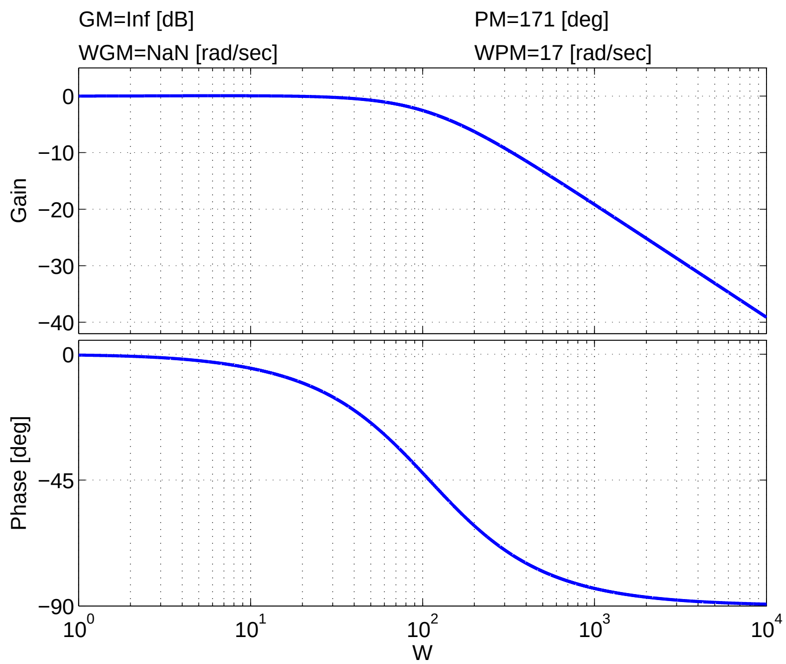

Figure E.7: Bode Plot, GM is the gain margin, WGM is the frequency at GM, PM is the phase margin, WPM is the frequency at PM.

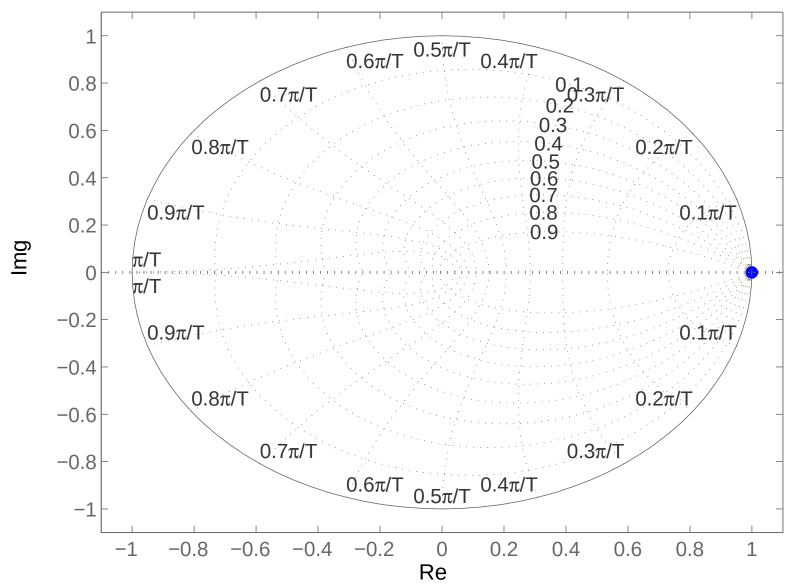

Figure E.8: Pole zero map.

E.3 Control Plots for Load-piston System

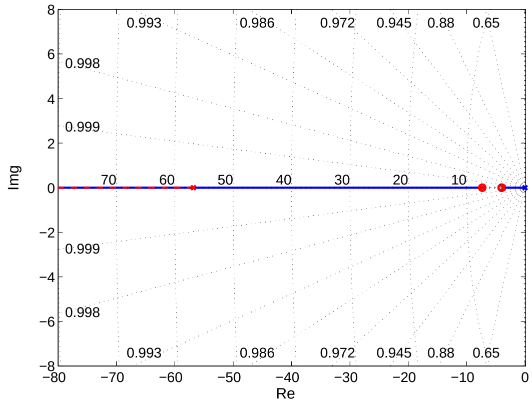

Figure E.9: Root locus of $G_{CL_{pol}}$ (blue) and $G_{CL_{pcl}}$ (red).

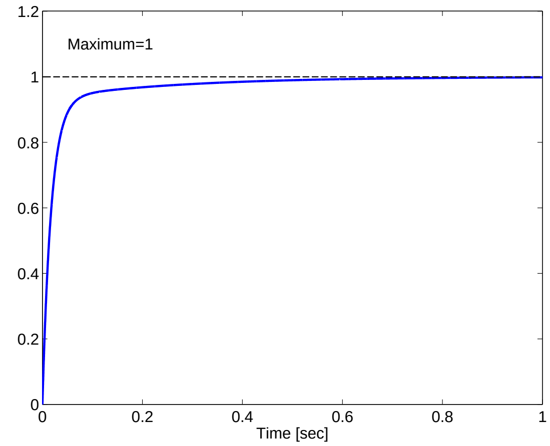

Figure E.10: Unity step response of $G_{CL_{pcl}}$.

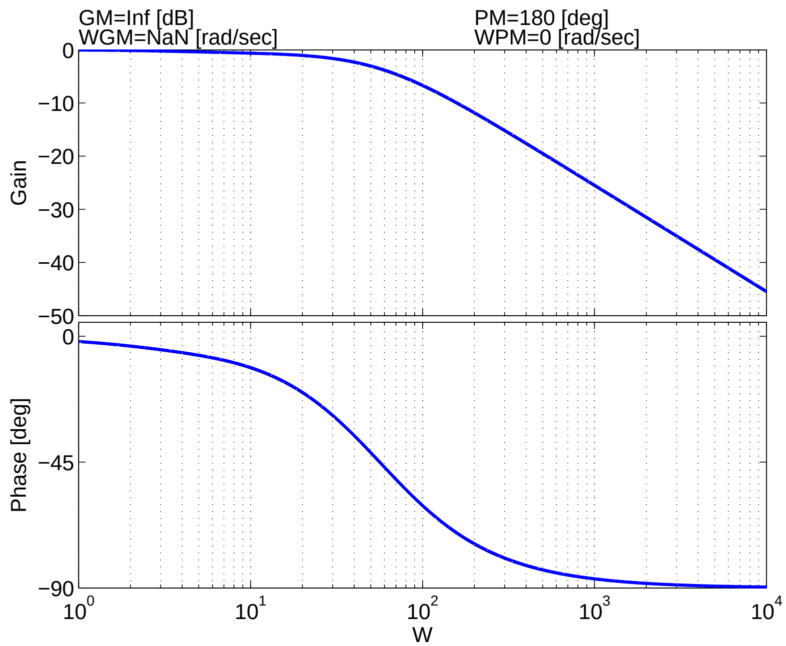

Figure E.11: Bode Plot, GM is the gain margin, WGM is the frequency at GM, PM is the phase margin, WPM is the frequency at PM.

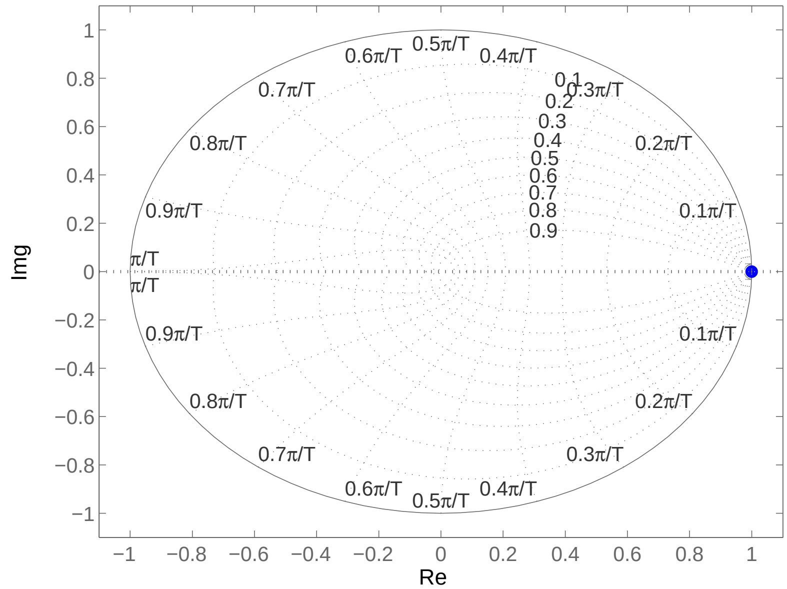

Figure E.12: Pole zero map.

F Experimental Results

F.1 The Influence of Acceleration on Friction

dr

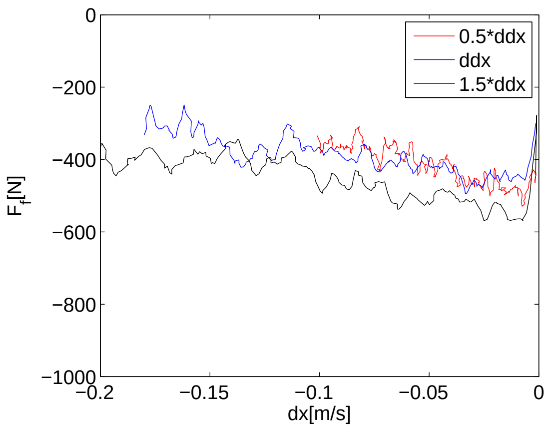

Figure F.1: Friction curve derived from velocity ramp data for $F_L = 500[N]$.

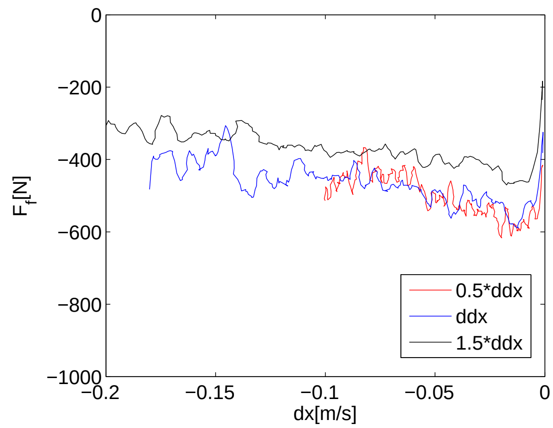

Figure F.2: Friction curve derived from velocity ramp data for $F_L = 1000[N]$.

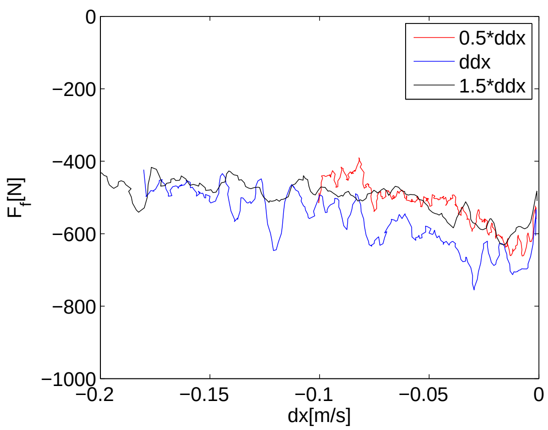

Figure F.3: Friction curve derived from velocity ramp data for $F_L = 2000[N]$.

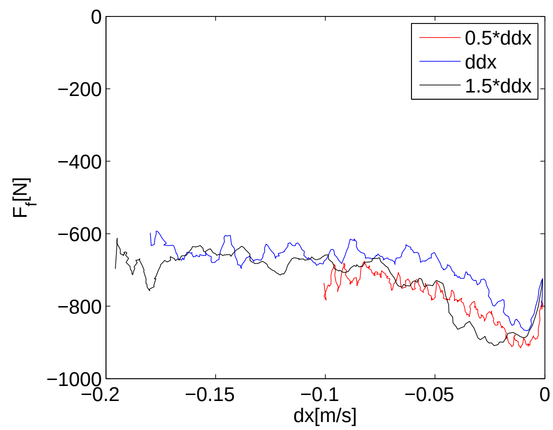

Figure F.4: Friction curve derived from velocity ramp data for $F_L = 5000[N]$.

F.2 Directional Influence on Friction

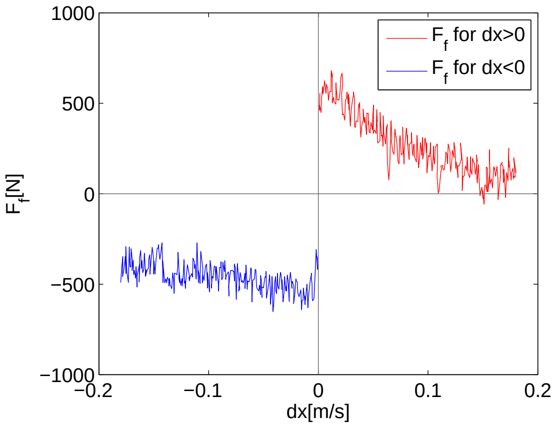

Figure F.5: Friction curve covering both positive and negative velocity regime for velocity ramp test with $F_L = 1000[N]$.

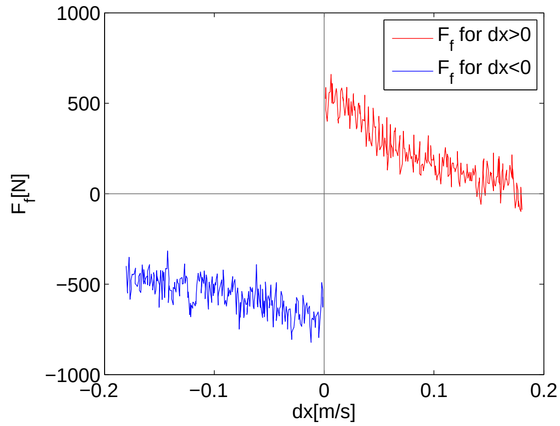

Figure F.6: Friction curve covering both positive and negative velocity regime for velocity ramp test with $F_L = 2000[N]$.

F.3 General Review of Friction results

Measured values for steady state velocity and a ramped velocity input at $F_L = 5000[N]$.

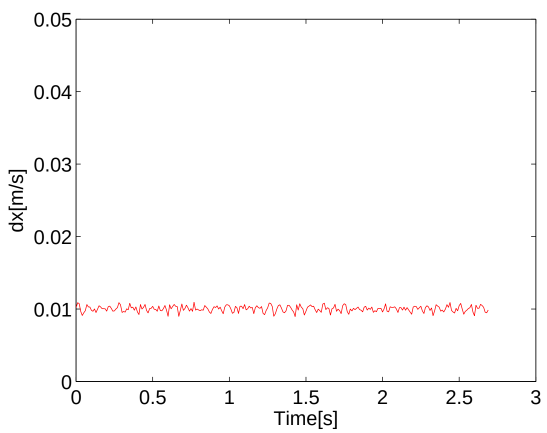

Figure F.7: Velocity profile for steady state velocity. The velocity reference is set to $0.01[m/s]$ and $F_L = 5000[N]$.

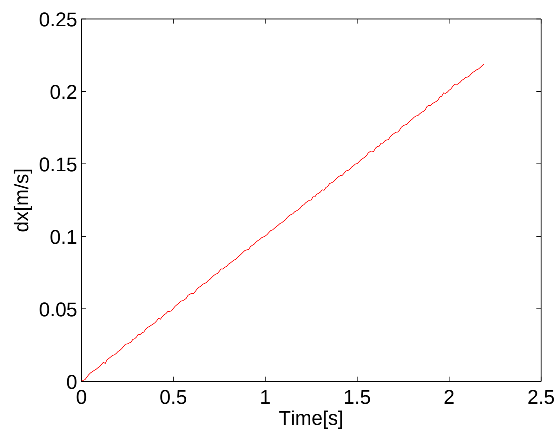

Figure F.8: Velocity ramp profile for an acceleration of $0.1[m/s^2]$ and $F_L = 5000[N]$. A arrow is identifying the point at which values are to be compared for the steady state and ramping velocity.

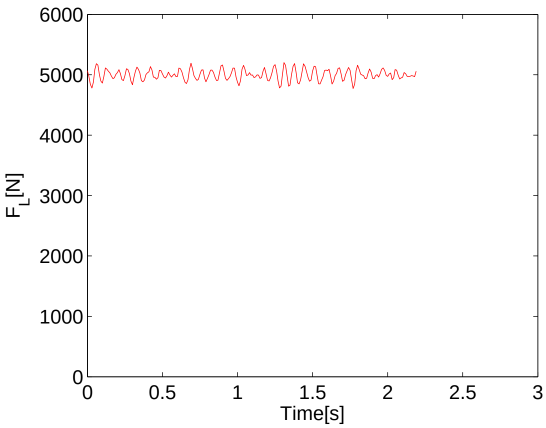

Figure F.9: The resulting force from the load cylinder at steady state.

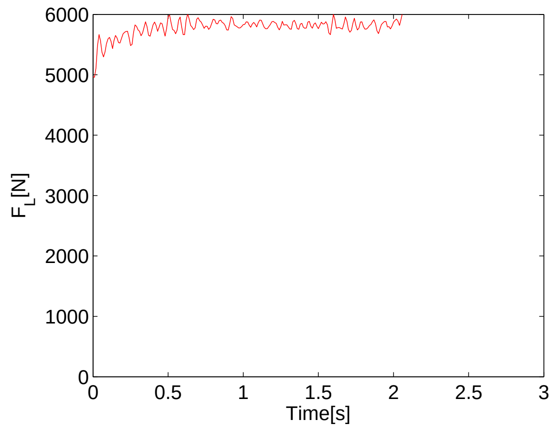

Figure F.10: The resulting force from the load cylinder when ramping the velocity.

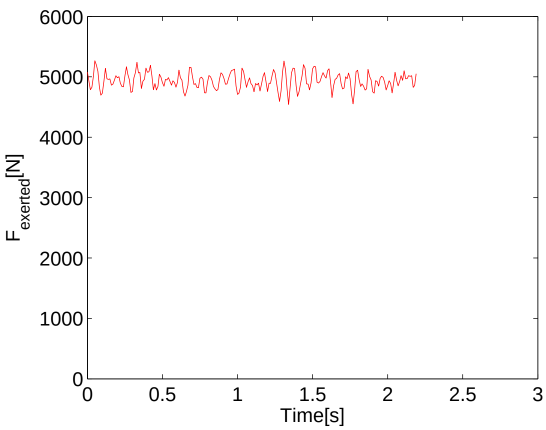

Figure F.11: The force measured by the strain gage at steady state.

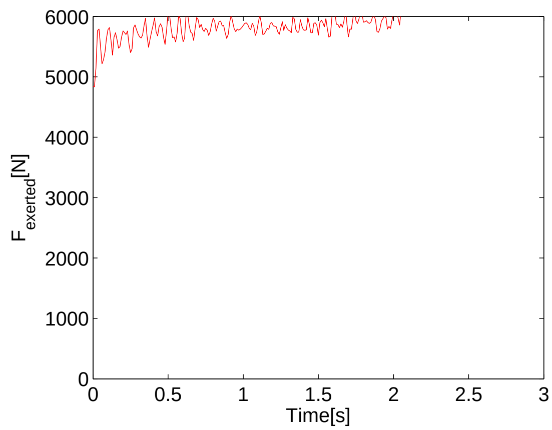

Figure F.12: The force measured by the strain gage when ramping the velocity.

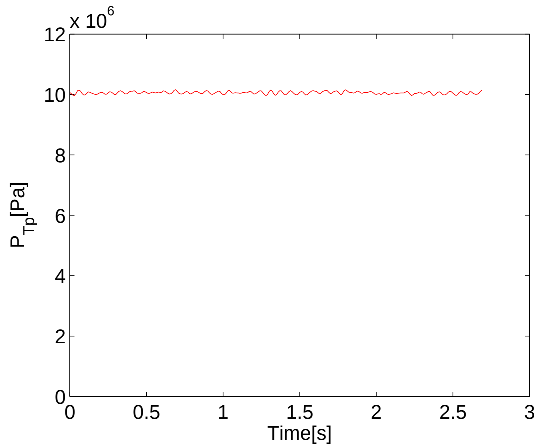

Figure F.13: The piston chamber pressure measured at steady state.

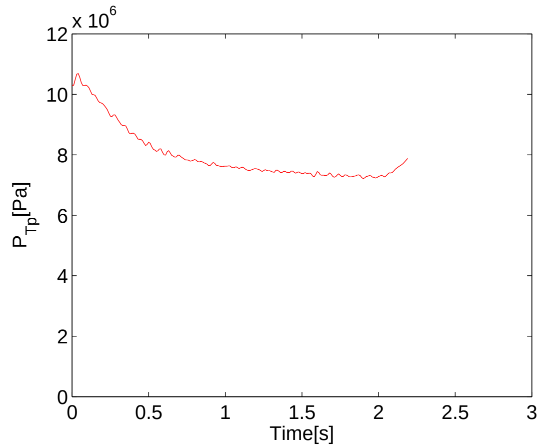

Figure F.14: The piston chamber pressure measured when ramping the velocity.

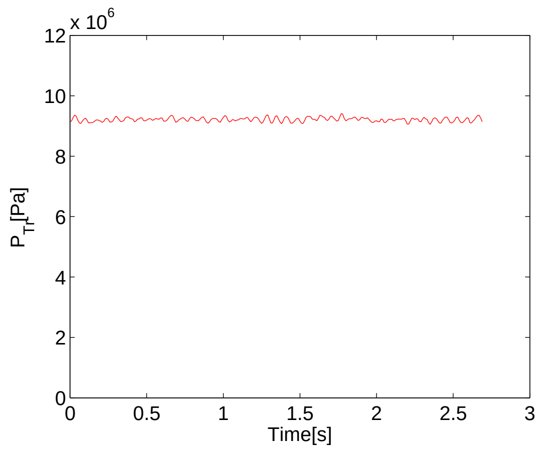

Figure F.15: The rod chamber pressure measured at steady state.

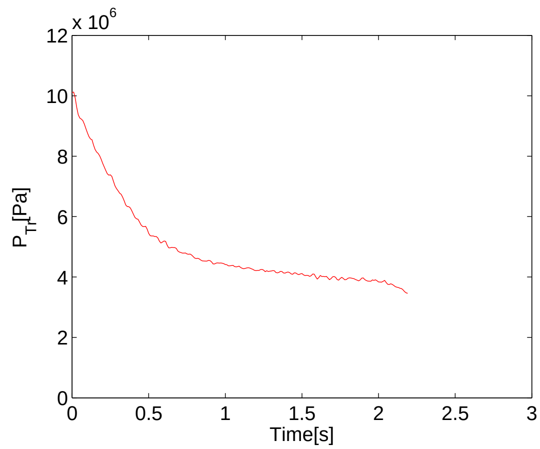

Figure F.16: The rod chamber pressure measured when ramping the velocity.

F.3.1 Confidence Interval

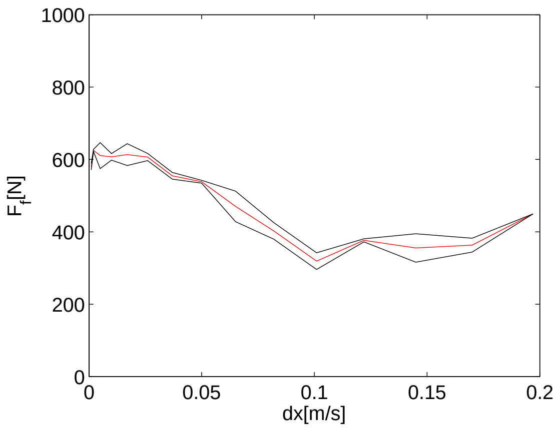

Figure F.17: Confidence interval for steady state Stribeck curve with $F_L = 1000[N]$.

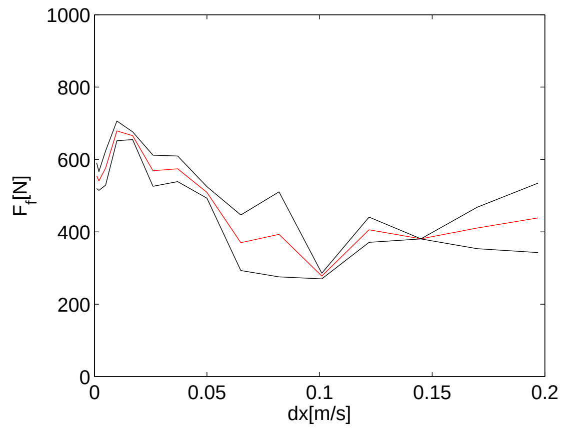

Figure F.18: Confidence interval for steady state Stribeck curve with $F_L = 2000[N]$.

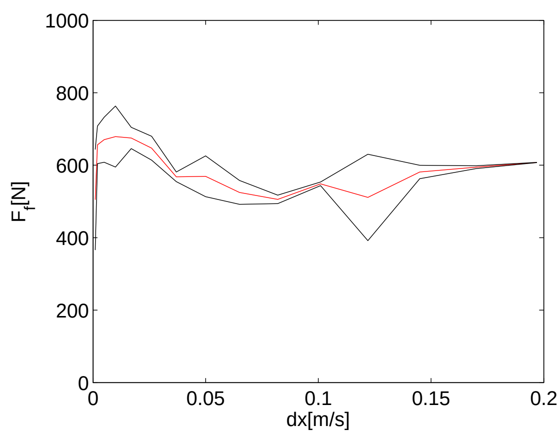

Figure F.19: Confidence interval for steady state Stribeck curve with $F_L = 5000[N]$.

F.4 Efficiency

F.4.1 $F_L = 1000[N]$

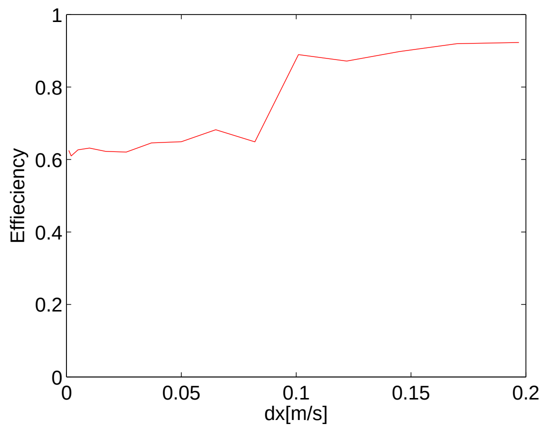

Figure F.20: Efficiency curve derived from steady state velocity curve data for $F_L = 1000[N]$.

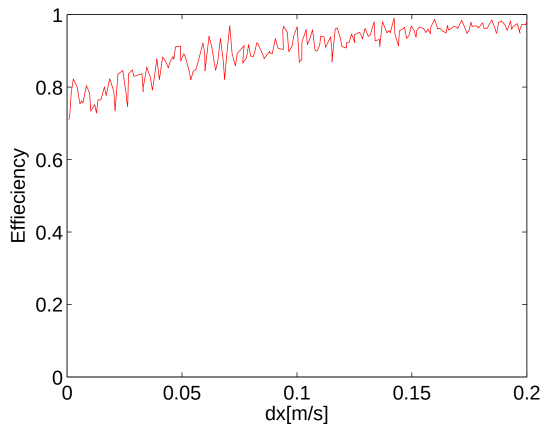

Figure F.21: Efficiency curve derived from velocity ramp data for $F_L = 1000[N]$.

F.4.2 $F_L = 2000[N]$

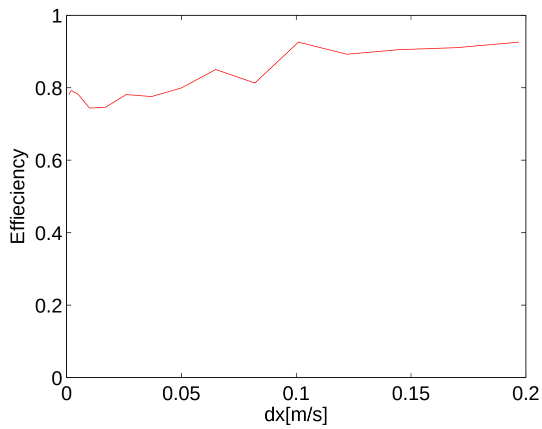

Figure F.22: Efficiency curve derived from steady state velocity curve data for $F_L = 2000[N]$.

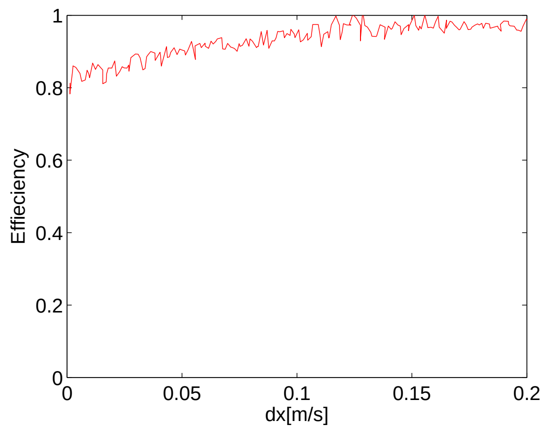

Figure F.23: Efficiency curve derived from velocity ramp data for $F_L = 2000[N]$.